

**Investigation of Methane Hydrate Formation Kinetics Using Machine  
Learning and Computational Fluid Dynamics Tools**

By  
©Marziyeh Zare

A thesis submitted to the school of Graduate Studies in partial fulfilment of the  
requirements for the degree of

Doctor of Philosophy

Faculty of Engineering and Applied Science  
Memorial University

October 2022

St. John's, Newfoundland and Labrador  
Canada

## **ABSTRACT**

Hydrate blockage in oil and gas facilities can cause a significant economic impact in terms of deferred production and remediation costs, particularly in harsh conditions (e.g., deep water). Financial considerations and safety concerns have motivated most operating companies to apply the hydrate management approach rather than the hydrate avoidance strategy. The hydrate management strategy requires a detailed understanding of how hydrates form, accumulate, deposit, and jam in pipeline systems. Despite all efforts that have been accomplished to find out the best method to manage and control hydrate formation in oil facilities, hydrate formation remains a challenge for the industry, and more research is needed to find reliable/effective methods for hydrate management. This research thesis starts with an extensive literature review, and the first series of simulation runs are performed to study methane hydrate formation in a jumper using a computational fluid dynamics (CFD) software, named Star CCM+. The numerical model for the simulation phase is developed through considering transport phenomena equations, including conservation of mass, momentum, and energy in which mass transfer, hydrate reaction kinetics model, and heat of hydrate formation are incorporated in the multiphase flow equations in the form of source terms in the CFD software. An extensive sensitivity analysis is performed to study the influences of changes in the inlet fluid velocity, gas volume fraction, inlet temperature, and subcooling on the hydrate formation in the jumper. The results indicate that the developed CFD model can simulate methane hydrate formation in the jumper with high precision. The amount of hydrate decreases when the value of the liquid inlet velocity and gas inlet temperature parameters increases. In contrast, an increase in subcooling and gas volume fraction leads to more hydrate formation in the jumper. More hydrate can be observed close to the wall, where the temperature is low and subcooling has high values. In the next phase, the induction time for the methane hydrate

formation in the presence of Luvicap 55W (a kinetic hydrate inhibitor - KHI) solutions is determined using artificial intelligence models, including least squares support vector machine (LSSVM), adaptive network-based fuzzy inference system (ANFIS), and gene expression programming (GEP). For these models, 440 experimental data taken from the literature are employed, where 85% of data is utilized for the training step and 15% for the testing step. Induction time is considered as a target and the molecular weight of solution, mass fraction of KHI, temperature, pressure, and subcooling are the input parameters for these deterministic models. The performance of the smart models for the training and testing steps is evaluated using average relative error percent (ARE %), average absolute relative error (AARE %), and coefficient of determination ( $R^2$ ). Moreover, the Pearson correlation coefficient is calculated for the input parameters based on the ANFIS model to identify the influence of the input parameters on the induction time. The outcome shows that among LSSVM, ANFIS, and GEP models, the GEP technique has an excellent performance in predicting induction time. For instance, the values of the coefficient of determination ( $R^2$ ) for the developed GEP model are 0.9582 and 0.9726 in the training and testing steps, respectively. Also, the results reveal that the most influential parameters are the system pressure and temperature. Other input parameters, including the molecular weight of the solution, mass fraction of the Luvicap 55 W, and subcooling, have an indirect relationship with the induction time. In the next phase of this thesis, methane hydrate formation is simulated in an agitated reactor using Star CCM+ with a stirring rate of 300 RPM, a volume fraction of 0.04, and a pressure of 5,500 kPa. Then, the results are validated using the experimental data adapted from literature where an overall absolute average deviation (AAD%) of 15.6% is obtained. The effect of various parameters, including stirring rate, methane volume fraction, pressure, and subcooling is investigated on the hydrate formation in the stirred reactor. It is found that hydrate is formed more close to the wall and the impeller blades when the wall temperature is 274.15 K. Moreover, an

increase in the parameters of stirring rate, methane volume fraction, pressure, and subcooling increases the amount of methane hydrate formation in the reactor. This CFD model can simulate hydrate formation in the stirred reactor with an acceptable accuracy. This model can be extended to other geometries of oil and gas facilities; it can be useful for corresponding industries to predict hydrate formation in transportation and processing facilities.

## ACKNOWLEDGMENTS

I would like to express my deepest gratitude to those who gave me invaluable advice, suggestions, and unlimited support. This endeavor would not have been possible without the generous support of many people.

I am extremely grateful to my supervisor Dr. Sohrab Zendehboudi and co-supervisor Dr. Abedinzadegan Abdi for their noble guidance, patience, and support. I have benefited greatly from their enormous knowledge and precise editing. Their friendly guidance and invaluable advice have been beneficial throughout all phases of this research. I am extremely grateful to Dr. Vandad Talimi for his valuable suggestions and discussions on the CFD simulations which have been incorporated into an improvement of this section of the thesis.

I would like to extend my sincere thanks to Memorial University (NL, Canada), the Natural Sciences and Engineering Research Council of Canada (NSERC), Equinor Canada, and InnovateNL for offering financial assistance.

I would be remiss in not mentioning all of my friends, my parents, and my siblings for encouraging and helping me to keep my spirit, and supporting me whenever I needed them. I would like to thank my lovely husband, Shahram, who has been a constant source of support and encouragement during this endeavor. I could not have undertaken this journey without his support.

*“This dissertation is dedicated to my parents and my husband.”*

## Table of Contents

ABSTRACT.....	ii
ACKNOWLEDGMENTS .....	v
LIST OF TABLES.....	1
LIST OF FIGURES .....	2
1. CHAPTER ONE.....	5
1.1 INTRODUCTION AND BACKGROUND.....	5
1.2 LITERATURE REVIEW .....	7
1.3 RESEARCH CONTRIBUTION.....	16
1.4 THESIS ORGANIZATION.....	17
2. CHAPTER TWO .....	33
Computational Fluid Dynamic Modeling of Methane Hydrate Formation in Subsea Jumper .	33
Preface.....	33
ABSTRACT.....	34
2.1 INTRODUCTION .....	35
2.3.1 Model Geometry and Mesh Creation.....	40
2.3.2 Boundary and Initial Conditions.....	42
2.3.3 Numerical Model .....	42
2.3.4 Model Solution.....	47
2.4.1 Effect of Inlet Liquid Velocity on Hydrate Formation .....	52
2.4.2 Effect of Fluid Inlet Temperature and Subcooling on Hydrate Formation.....	55
2.4.3 Effect of Gas Volume Fraction on Hydrate Formation .....	57
2.5 CONCLUSIONS.....	58
3. CHAPTER THREE .....	69
Deterministic Tools to Estimate Induction Time for Methane Hydrate Formation in the Presence of Luvicap 55 W Solutions .....	69
Preface.....	69
ABSTRACT.....	70
3.1 INTRODUCTION .....	71
3.2 LITERATURE REVIEW .....	76

3.3	THEORY OF DETERMINISTIC MODELS .....	80
3.3.1	LSSVM Model.....	80
3.3.2	ANFIS Model.....	84
3.3.3	GEP Model.....	86
3.4	METHODOLOGY: KEY STEPS.....	89
3.4.1	Data Analysis .....	90
3.4.2	Modeling Tool Selection.....	92
3.4.3	Model Evaluation Criteria.....	93
3.5	RESULTS AND DISCUSSION.....	94
3.5.1	LSSVM Model Performance Evaluation .....	94
3.5.2	ANFIS Model Performance Evaluation.....	96
3.5.3	GEP Model Performance Evaluation.....	100
3.5.4	Comparison of the Results of LSSVM, ANFIS, and GEP Models .....	105
3.5.5	Sensitivity Analysis of ANFIS Model .....	107
3.6	CONCLUSIONS.....	110
4.	CHAPTER FOUR.....	130
	Computational Fluid Dynamics Approach to Study Methane Hydrate Formation in Stirred Reactor .....	130
	Preface.....	130
	ABSTRACT.....	131
4.1	INTRODUCTION .....	132
4.2	CFD MODELING AND METHODOLOGY.....	139
4.2.1	Model Geometry .....	140
4.2.2	Mesh Creation and Mesh Independence Test.....	142
4.2.3	Boundary and Initial Conditions.....	144
4.3	Computational Fluid Dynamic Model .....	144
4.3.1	Numerical Solution.....	149
4.3.2	Model Validation .....	150
4.4	RESULTS AND DISCUSSION.....	152
4.4.1	Effect of Stirring Rate.....	154
4.4.2	Effect of Gas Volume Fraction .....	156
4.4.3	Effect of Pressure and Subcooling.....	160
4.5	CONCLUSIONS.....	165
	ACKNOWLEDGMENTS .....	168
	APPENDIX A.....	168

NOMENCLATURES .....	170
REFERENCES .....	172
5. CHAPTER FIVE .....	180
Summary and Recommendations for Future Work .....	180
5.1 Computational Fluid Dynamic Modeling of Methane Hydrate Formation in Subsea Jumper (Chapter 2) .....	181
5.2 Deterministic Tools to Estimate Induction Time for Methane Hydrate Formation in the Presence of Luvicap 55 W Solutions (Chapter 3).....	182
5.3 Computational Fluid Dynamics Approach to Study Methane Hydrate Formation in Stirred Reactor (Chapter 4).....	184
5.4 Recommendations for Future Work.....	186

## LIST OF TABLES

Table 2-1. Boundary conditions considered for the model.....	42
Table 2-2. Values of main parameters used in the model.....	48
Table 2-3. Model specifications for hydrate formation in the jumper.....	49
Table 3-1. Summary of experimental data.....	92
Table 3-2. ANFIS model specifications to predict the induction time for methane + Luvicape 55W+ water systems. ....	97
Table 3-3. Specifications of GEP model to determine the induction time for methane + Luvicap 55W+ water systems. ....	101
Table 3-4. The parameters of GEP correlation. ....	103
Table 3-5. Error analysis results for the introduced models. ....	105
Table 4-1. Boundary conditions and range of parameters for the CFD model.....	144
Table 4-2. Thermophysical properties for water, methane, and hydrate used in the CFD modeling. ....	150
Table 4-3. CFD Model specifications for hydrate formation simulation in the stirred reactor ..	150
Table 4-4. Validation of the CFD model with experimental data.....	151
Table 4-5. Mass fraction of hydrate as a function of stirring rate[ $\text{gas volume fraction} = 0.04, .$	156

## LIST OF FIGURES

Figure 1-1. Unit crystals, hydrate structures (sI, sII, and sH), and constituent cavities [5].	6
Figure 1-2. Schematic diagram of the HyJump flowloop [75].	11
Figure 2-1. Three-dimensional CAD model of the jumper.	41
Figure 2-2. Polyhedral meshing scheme.	42
Figure 2-3. Contour plots of mass fraction of hydrate in the jumper [Fluid velocity =5 m/s; gas volume fraction (VF) = 0.2; and fluid inlet temperature = 7°C].	49
Figure 2-4. Hydrate mass fraction contours for points of B, C, E, and H [fluid velocity =5 m/s; gas volume fraction (VF) = 0.2; and fluid inlet temperature = 7 °C].	51
Figure 2-5. Contour plots of liquid velocity in the jumper [inlet velocity =5 m/s; gas volume fraction (VF) = 0.2; and fluid inlet temperature =7°C].	52
Figure 2-6. Contour plots of hydrate mass fraction at various liquid velocities in the jumper [gas volume fraction (VF) =0.2; and fluid inlet temperature =16°C].	53
Figure 2-7. Effect of liquid velocity on the mass fraction of hydrate in different time steps	54
Figure 2-8. Cross-sectional contour plots of the liquid velocity in the jumper outlet for various inlet fluid velocities [gas volume fraction (VF) =0.2; fluid inlet temperature = 7 °C].	55
Figure 2-9. Cross-sectional contour plots of subcooling at jumper stations [gas volume fraction (VF) = 0.2; fluid inlet temperature =10 °C; and liquid velocity = 5 m/s].	56
Figure 2-10. Effect of liquid velocity and fluid inlet temperature on the hydrate mass fraction in the jumper.	57
Figure 2-11. Effect of gas volume fraction and fluid inlet temperature on the hydrate mass fraction in the jumper.	58
Figure 3-1. General sketch for induction time calculation using deterministic models.	80
Figure 3-2. Structure of the LSSVM method (modified after Shaberi and Suhartono [97]).	83

Figure 3-3. ANFIS model structure for a system with two inputs $x_1, x_2$ , and one output (modified after [99]).	85
Figure 3-4. An example of an expression tree of $(xab + cd)$ for GEP model (adapted from Mohammed & Sharifi [103]).	88
Figure 3-5. Flowchart of the GEP model (modified after [104]).	89
Figure 3-6. The histograms of experimental data: (a) Molecular weight of solution, (b) Lvicap 55 W concentration, (c) Temperature, (d) Subcooling, (e) Pressure, and (f) Induction time.	91
Figure 3-7. Performance of LSSVM model: (a) Training and (b) Testing.	95
Figure 3-8. Histogram of relative errors for LSSVM model.	96
Figure 3-9. Membership functions for input parameters of developed ANFIS model.	98
Figure 3-10. Performance of ANFIS model: (a) Training and (b) Testing.	99
Figure 3-11. Histogram of relative errors for ANFIS model.	100
Figure 3-12. Performance of GEP model: (a) Training and (b) Testing.	102
Figure 3-13. Histogram of relative errors for GEP model.	103
Figure 3-14. Expression trees of the developed GEP model.	104
Figure 3-15. $R^2$ value for the developed models of ANFIS, LSSVM, and GEP.	106
Figure 3-16. Comparing experimental and predicted induction times obtained from LSSVM, ANFIS, and GEP models for two phases: (a) Training, and (b) Testing.	107
Figure 3-17. Pearson correlation coefficient between the induction time and input parameters, including the molecular weight of solution ( $M_{wsol}$ ), the mass fraction of KHI ( $mi$ ), temperature ( $T_{exp}$ ), system pressure ( $P$ ), and subcooling ( $\Delta T$ ).	109
Figure 3-18. Correlation coefficient values for induction time with respect to input parameters.	110
Figure 4-1. Flowchart for CFD simulation.	140
Figure 4-2. Three-dimensional CAD model of stirred reactor (A = 7 mm, B = 75 mm, C = .55 mm, D = 20 mm, E = 6 mm, F = 18.75 mm, and G = 5 mm)	141
Figure 4-3. Mesh layout of the stirred reactor (a) and plate section (b).	143

Figure 4-4. Hydrate mass fraction (a) and gas volume fraction in the stirred reactor (b) [stirring rate = 300 rpm, pressure = 5,500 kPa, gas volume fraction = 0.04, and system temperature = 274.3 K]. .....	153
Figure 4-5. Hydrate mass fraction contour for cross-section area of stirred reactor [stirring rate= 300 rpm, gas volume fraction = 0.04, pressure = 5,500 kPa, and system temperature = 274.3 K]. .....	154
Figure 4-6. The effect of stirring rates on the hydrate mass fraction in the stirred reactor [gas volume fraction = 0.04, system pressure = 5,500 kPa, and system temperature = 274.3 K]. .....	155
Figure 4-7. Effect of gas volume fraction and stirring rate on the methane hydrate formation in the stirred reactor, [pressure = 5,500 kPa, system temperature = 274.3 K]. .....	158
Figure 4-8. Effect of gas volume fraction on the methane hydrate formation in the stirred reactor [stirring rate = 500 RPM, pressure = 5,500 kPa, system temperature = 274.3 K]. .....	159
Figure 4-9. Effect of pressure and stirring rate on the methane hydrate mass formation in the stirred reactor [gas volume fraction=0.2, system temperature = 274.3 K]. .....	162
Figure 4-10. The contours of hydrate mass fraction for different pressure in the stirred reactor .....	163
Figure 4-11. Effect of subcooling on the methane hydrate mass formation in the stirred reactor [gas volume fraction=0.2, system temperature = 274.3 K]. .....	164
Figure 4-12. Contour plots of mass fraction of hydrate in the stirred reactor with different degrees of subcooling [stirring rate = 900 RPM, gas volume fraction=0.2, and system temperature = 274.3 K]. ....	165

# 1. CHAPTER ONE

## 1.1 INTRODUCTION AND BACKGROUND

Gas clathrates, which are known as gas hydrates, are crystalline compounds that occur when the water molecules form a cage-like structure around guest molecules [1, 2]. Gas hydrates can be formed at temperatures below as well as above the normal freezing point of water. There is no chemical bonding that exists between the water molecules and the enclosed guest molecule [3]. The literature shows that gas hydrates can be formed in oil/gas systems at high pressure and low temperature conditions. Gas hydrates can be classified based on their structures (Type I, Type II, and Type H), where the number of cages and their sizes are different [4]. The 512 is a basic cage as a building block which forms three structures. The structure I (sI) is a body center cubic structure that is formed with small natural gas components such as methane and ethane. Structure II (sII) with a diamond lattice within a cubic framework forms when natural gases or oil comprise molecules larger than ethane but smaller than pentane. This structure commonly forms in oil/gas production systems in the processing facilities. The hexagonal framework is named structure H (sH) in which the size of cavities is large enough to contain large molecules such as naphtha and gasoline [1].

Different gas molecules, such as methane, ethane, propane, isobutane, normal butane, nitrogen, carbon dioxide, and hydrogen sulfide can make gas hydrates with water molecules in crystalline structures [3]. Four conditions are required for hydrate formation, including presence of water, small hydrocarbons ( $< 9 \text{ \AA}$  diameter), low temperature (e.g.,  $< 80 \text{ }^\circ\text{F}$ ), and high pressure ( $>200 \text{ psig}$ ). It is noted that in the absence of any of these conditions, hydrates will not occur [5]. The predictions of hydrate thermophysical and thermochemical properties do not have any consistency

and patterns (or trends) due to the complexity of the hydrate structures. Ross et al. (1981) found that the thermal conductivity of THF hydrate is pressure independent, and this property is a function of temperature [6]. It was reported that the thermal conductivities of THF (Tetrahydrofuran) hydrates are similar to methane hydrates with a value of  $0.50 \text{ Wm}^{-1} \text{ K}^{-1}$  [7]. The density measurement of gas hydrate only is possible using NMR (Nuclear Magnetic Resonance) and EPR (Electron Paramagnetic Resonance) technologies. The geometrical structures of gas molecules and water in hydrate structures reveal that the physical properties of gas hydrates are between pure ice and pure water [7]. Figure 1-1. indicates the specification of three hydrate structures (SI, SII, and SH) [5].

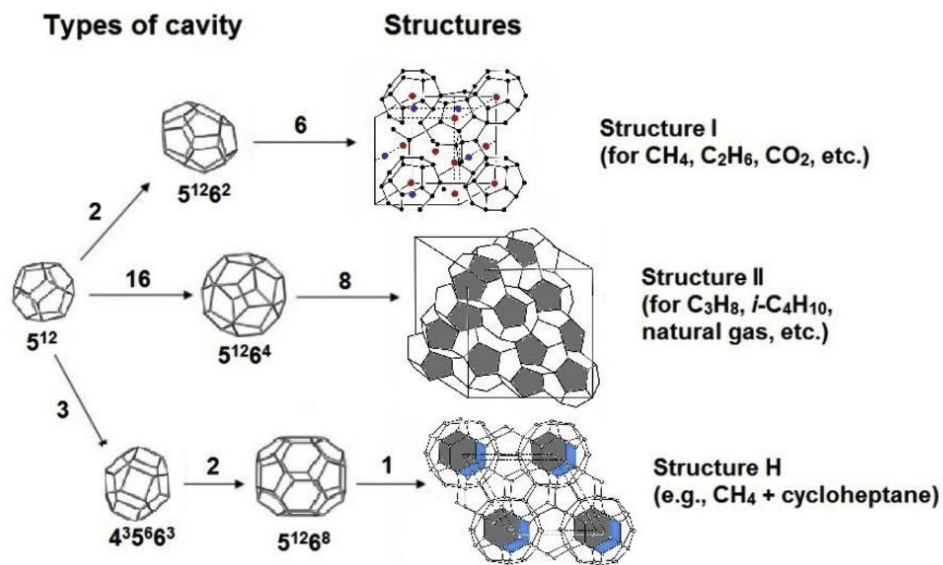


**Figure 1-1.** Unit crystals, hydrate structures (sI, sII, and sH), and constituent cavities [5].

Offshore oil/gas facilities are very expensive (typically more than US\$ 1 billion). Therefore, sustainability and preservation of production rates are crucial for the oil/gas companies. The survey from many companies showed that flow assurance is a major technical problem in oil and gas

facilities [2, 5]. Flow assurance is the process in which fuel production is guaranteed through minimizing the restrictions on the hydrocarbon flow from the reservoir to the sale spot. The formation of gas hydrates can cause flow assurance issues as it can disrupt the pipelines by agglomeration and blockage. The offshore pipeline disruption caused by gas hydrate formation can create a serious flow assurance issue and cause huge economic losses and human risks when it is not remediated [8]. During flow stops, the temperature of deep-water pipelines decreases at a much faster rate than pressure. Therefore, hydrate formation probably occurs in pipelines during shutdowns, restarts, and flow stops [4]. The pipeline is separated into two distinct zones of higher and lower pressures when the hydrates form in this flowline. The higher-pressure zone is between the source (hydrocarbon production) and plug, while the lower-pressure zone is formed between the plug and outlet. In the high-pressure zone, the pipe burst can occur due to pressure rise. The plug can be a projectile that destroys the pipe when the pressure difference between two distinct zones increases. These events can put personnel at risk and damage production equipment [7, 9-11]. Hydrates, waxes, scale, corrosion, and asphaltenes are the critical issues in flow assurance [12]. In recent years, researchers have focused on hydrate agglomeration and plugging mechanisms in different patterns in oil and gas transportation flowlines experimentally and theoretically (oil-dominated, gas-dominated, and water-dominated systems) [13-19].

## **1.2 LITERATURE REVIEW**

Ginns (1928) investigated nucleation kinetics [2]. Kashchiev and Firoozabdi reviewed different hydrate nucleation theories [2, 20, 21]. Nucleation can occur based on the theory of homogeneous and heterogeneous crystallization. Homogeneous nucleation (HON) does not need any impurities to take place with two-phase system, while heterogeneous nucleation (HEN) needs impurities, such as a foreign body or surface [2, 22]. The driving force is a key component for hydrate

nucleation processes and it is used in developed correlations. Researchers studied nucleation theories by using different driving forces [2, 21, 23-26]. Anklan and Firoozabadi (2004) [27] estimated the driving force for the hydrate nucleation of multicomponent mixtures based on their chemical potentials. They also developed equations for the calculation of the compositions of critical hydrate nuclei in multicomponent systems [27]. High-pressure differential scanning calorimetry has been used for the hydrate nucleation of the gas phase hydrate formers [28]. The results showed that a subcooling of around 30 K should be maintained for hydrate nucleation to occur. Although the system pressure had a considerable effect on the hydrate nucleation temperature, cooling rates (a range of 0.5-3 /min) did not affect it appreciably. The methane hydrate nucleation and growth were estimated using a quiescent high-pressure view cell. In each step of the hydrate formation, pictures were taken to better understand the hydrate formation mechanisms. At an initial pressure of 10 MPa, a thick layer of hydrate formed at the interface of the methane-water phases that caused no diffusion of methane gas into the water phase, resulting in a decrease in hydrate formation. However, at an initial pressure of around 19.5 MPa, a hydrate formation occurred in the liquid bulk close to the interface of the two phases [29].

Several researchers experimentally studied the conditions of hydrate growth for various gases. Their results showed that gas hydrate initiates and grows at the water-hydrocarbon interface [30-33]. In the hydrate growth theory, three factors are considered: the kinetics of crystal growth at the hydrate surface, mass transfer of components to the growing crystal surface, and heat transfer of the exothermic heat of hydrate formation outside of the crystal surface [2]. Three controlling mechanisms or their combinations, including intrinsic kinetics, mass transfer, and heat transfer, can be involved in hydrate growth modeling [2, 34, 35]. Englezos' model is popular and utilized for hydrate formation growth theory by researchers. This model takes into account the role of

hydrate intrinsic kinetic in hydrate growth; however, their results showed that heat and mass transfer play a greater role in hydrate growth in real systems [36]. In terms of mass transfer as a controlling mechanism for the hydrate growth model, a simple film model was proposed by Skovborg and Rasmussen (1994) where the gas transportation from the vapor phase through the liquid film at the vapor-liquid interface is the rate-limiting step for the overall process [37]. Uchida et al. (1999) developed a hydrate growth model in which heat transfer was a controlling mechanism. It was found that hydrate formation rate depends on the temperature rather than other system parameters [38]. Different kinetics models of hydrate growth with different controlling systems have been developed by some researchers [39-44].

Hydrate formation process is a complicated phenomenon that involves two inter-related processes, a stochastic nucleation process, and a hydrate growth process. Understanding the concepts of heat and mass transfer, fluids flow, and intrinsic kinetics associated with phase changes can be useful to analyze this phenomenon [34]. From the microscopic point of view, hydrate growth is a combination of three steps. Firstly, the mass transfer of hydrate former and water on the hydrate crystal surface occurs. Secondly, the intrinsic kinetics of hydrate growth on the hydrate surface takes place. Finally, heat is released away through the exothermic reaction of hydrate formation on the hydrate crystal surface [2, 34]. Researchers have developed different hydrate growth models. The hydrate growth process can be modeled based on various controlling mechanisms: (i) Intrinsic kinetics, (ii) Mass transfer, and (iii) Heat transfer [2, 34, 35]. Hydrate growth models should be applied with high caution because hydrate nucleation is a stochastic process, especially in the initiation growth step. The hydrate growth models might be apparatus dependent. Although the hydrate structure has a remarkable effect on the hydrate growth model, most of the hydrate growth data have been measured only for the gases which form sI hydrate, while natural gas

typically forms the sII [2, 34]. Vysniauskas and Bishnoi (1983) developed a kinetic model for hydrocarbon hydrate formation [23]. It was later modified by other members of Prof. Bishnoi's group at the University of Calgary, Canada [36, 45, 46]. This model is still used in most of the published papers on hydrate formation growth [47]. Englezos et al. (1987) modeled the hydrate formation growth of methane, ethane, and their mixtures based on the crystallization theory coupled with the two-film theory for the gas adsorption into the liquid. [36]. Skovborg and Rasmussen (1994) developed a simple film model for gas consumption rate which was based on mass transfer instead of growth kinetics. In this model, the transportation of the gas from the vapor phase through the liquid film at the gas-liquid interface was the rate-limiting step for the overall process [37]. Uchida et al. (1999) submerged the water droplet in liquid carbon dioxide and measured the hydrate film-propagation rates. They found that the hydrate formation rate depends on the temperature rather than pressure or other system parameters [38].

Hydrate precipitation in pipelines reduces the cross-sectional area of the flowlines and increases the risk of disruptions. Different testing tools can be utilized to simulate real pipeline conditions. These experimental setups can be categorized into stirred cells [48-56], rocking cells [57-59], and flow loops [60-64]. The apparatuses have some advantages and drawbacks [59]. One of the advantages of the flow loops is that the flow conditions in the flow loop are similar to the flowline in the field. However, these apparatuses are not widely common systems due to the high costs of assembly and operation. Moreover, the stirred cells and the rocking cell are the lab scale apparatuses that provide valuable experimental information, while the flow conditions in the flowline are not considered. Thus, the extension of the results to field conditions is difficult [59]. Sa et al. (2019) proposed a new rock-flow cell and investigated effects of different parameters, including liquid loading, water cut, and rocking angle/speed on hydrate formation in different flow

regimes [59]. Rao et al. (2018) studied hydrate formation mechanisms and slurry flow in the spiral flow loop. Their results revealed that the hydrate formation in this flow loop is the same as in a conventional flow loop [65]. Hydrate formation and deposit mechanisms have been studied in different test systems where the effects of water cut, flow regime, inhibitors, and temperature (subcooling) have been investigated [63, 66-73]. Ding et al. (2017) proposed different plugging mechanisms in various flow regimes, such as slug flow, stratified flow, bubble flow, and annular flow in the high-pressure flow loop [69]. A flow loop with a jumper shape (HyJump flow loop) was designed and installed to estimate the hydrate formation performance in shutdown and restart situations. The preliminary restart gas tests in this flow loop provided apparent proof of hydrate deposition when the gas velocity was less than 0.26 ft/s [74]. Kumar et al. (2020) conducted restart tests for HyJump flow loop and injected the monoethylene glycol (MEG) in the concentration range of 0 – 30 wt% in this flowloop. The results indicated that hydrate deposition could be prevented considerably using 20 wt % MEG injection. This MEG content was approximately 50 percent less than the amount of thermodynamic inhibitors which is used in the oil and gas facilities [75]. The Schematic diagram of the HyJump flow loop is indicated in Figure 1-2 [75].

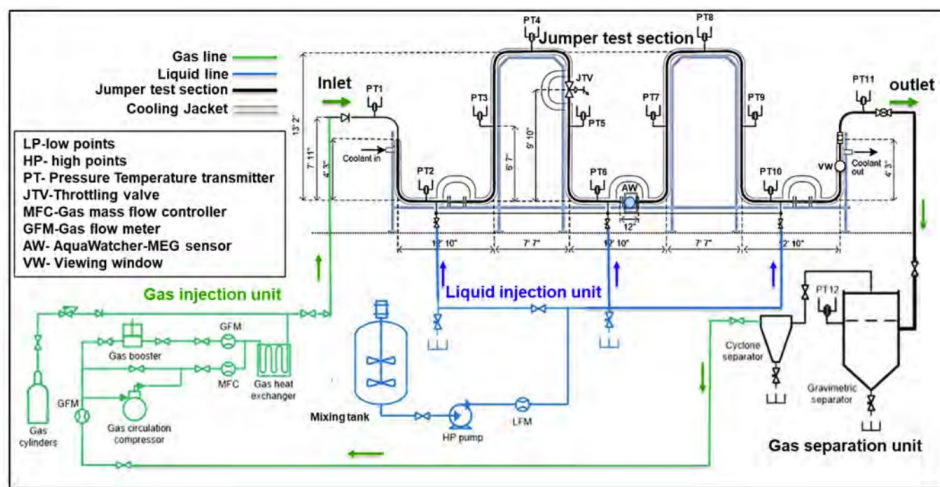


**Figure 1-2.** Schematic diagram of the HyJump flow loop [75].

Induction time or lag time is the time taken the hydrate particles are detected macroscopically after nucleation and onset of growth have occurred [1]. Methane hydrate formation in the presence of kinetic inhibitors (A, B, and C) is investigated in a high-pressure reactor. The effect of additives on the induction time and the quantity of formed hydrate is studied. It was found that the inhibitors are able to help increase the induction time and decrease the amount of hydrate crystals [76]. Hussain et al. (2006) investigated the ethane hydrate formation and decomposition in a batch agitated reactor at a temperature range of 270–280 K, a pressure range of 8.83–16.67 bar, and at various stirring rates of 110–190 rpm. According to the results, higher hydrate formation was observed at a faster stirring rate. Moreover, it was found that hydrate formation kinetics is related to pressure, temperature, degree of subcooling, and stirring rate [77]. The influences of temperature, initial water content, stirring rate, and reactor size on the methane hydrate formation in the stirred semi-batch autoclave reactor at a pressure of 90 bar were studied by Meindinyo and Svartaas (2016) [78]. It was revealed that subcooling has a significant impact on methane hydrate formation since increasing subcooling leads to an increase in the driving force for methane hydrate formation and growth. Also, the hydrate formation in batch/semi-batch reactor is considerably controlled by mass and heat transfer [78]. Longinos & Parlaktuna (2021) conducted some tests to study the effects of the type and numbers of impellers on the methane hydrate formation in a stirred tank reactor with a volume of 5.71 L. It was found that methane hydrate formation rate in the experiments with Rushton turbine (RT) impeller for all baffles is higher than that of pitched blade turbines upward pumping (PBTU) experiments, while RT blades consume more energy. The results of experiments with dual impellers were the same as single impellers tests [79].

Different simulation software packages could be utilized to estimate hydrate formation and agglomerations in subsea pipelines, such as CFD (Computational Fluid Dynamic), Gromax,

OLGA-CSMHyK, and HyFAST2 [13, 80-83]. In OLGA-CSMHyK, the kinetics hydrate formation models are coupled with commercial software, OLGA, to estimate the risk of hydrate plugs in pipelines. A new flow assurance simulation tool (HyFAST2) was proposed by Norris et al. (2016) to assess the hydrate slurry viscosification for oil-dominated systems [82]. Gromax is also a powerful software that is utilized for the simulation of the behavior of different natural matters (such as wax and asphaltene) on the hydrate formation in the oil flow in flowlines [83-85].

In a research study, the hydrate formation behaviors in a subsea pipeline were investigated using the ANSYS/CFX-workbench 14 software. This CFD model helped to explore the impacts of fluid velocity, geometry (diameter), fluid viscosity, and water fraction on hydrate formation. The results showed that these parameters have significant influences on hydrate formation in flowlines [86].

The gas hydrate flow behaviours in a jumper were studied using CFD software (ANSYS 2019) integrated with a commercial subsea pipeline visualization tool. The maximum stress and deformation under different flow rates in different regions of the jumper were studied after the validation of the developed CFD model [87]. Yao et al. (2019) simulated hydrate slurry flow in pipes with different inclination angles using the Eulerian–Eulerian two-fluid multiphase flow model, which was combined with the PBM (Population Balance Model) [88]. Lo (2011) studied a pipeline with three phases, including oil (as a continuous phase), gas bubbles, and water/hydrate droplets as the dispersed phases using Star CCM+. The developed CFD model was based on the transport equations in which the equations of dissolved gas in the oil phase, mass transfer of gas from oil phase to water, and the reaction kinetics of hydrate formation were imbedded in the software to simulate the hydrate formation in the pipeline [89]. The Eulerian–Eulerian CFD model was employed to investigate the accumulation of Freon R11 hydrate particles in a turbulent flow of water. The model was validated using the flow loop data [90, 91]. Machine learning methods,

especially artificial intelligence, could be useful tools to assist in predicting/modeling hydrate formation behaviours and transportability in pipelines [92-97]. Qin et al. (2019) analyzed the data sets obtained at pilot-scale flow loop facilities (4500 data points) as well as operation field data using several machine learning techniques such as support vector machine (SVM) algorithm and neural networks (NN). In these models, the parameters such as water cut, gas-oil ratio, hydrate particle cohesive force, fluid (and oil) velocity, specific gravity, interfacial tension, and time are as the inlet parameters, while the hydrate fraction and probability of hydrate plugging variables are considered as output of these modeling. Additionally, the level of hydrate resistance to flow during restart or dead oil displacement was calculated. Their results showed that the machine learning model, as a proper predictive tool, can be applied to estimate the hydrate risks in the field [98]. The hydrate formation/dissociation temperature of natural gas/salt/alcohol systems was calculated using extremely randomized trees (Extra Trees or ET) and least square support vector machine (LSSVM). These models are able to determine the target parameter with  $R^2$  (coefficient of determination) greater than 96%. The results revealed that two models of LSSVM and ET can predict the hydrate equilibrium temperature and pressure as the objective functions with high precision [92]. LSSVM model is employed to calculate the natural gas hydrate equilibrium pressure and temperature, and mono ethylene glycol (MEG) flow rate for different systems, including natural gas/ MEG/water. Comparing the results showed that the total average absolute relative deviation errors for the gas hydrate equilibrium pressure, desired hydrate formation temperature (DHFT), and flow rate of MEG were 0.15, 0.58, and 7.17, respectively. It implies that the results of the LSSVM model are in good agreement with the experimental data [93]. Adjusting the gas temperature is vital when natural gas passes through the throttling process. Yarveicy et al. (2018) applied adaptive network-based fuzzy inference system (ANFIS), LSSVM, and radial basis

function artificial neural network (RBF-ANN) models to predict the initial natural gas temperature in this throttling process. It was found that the models could forecast this parameter precisely (an  $R^2$  more than 0.99 and AARD% less than 0.5). However, the predictions of the RBF-ANN model were more accurate than other deterministic models [99]. Amar (2021) studied the hydrate formation temperature (HFT) for various systems (e.g., sour gas, acid gas, and sweet gas mixtures) using the gene expression programming (GEP) model. The results revealed that the GEP model can predict the hydrate formation temperature (HFT) precisely for different systems with the average absolute relative error (AARE%) of 0.1397% [97].

Hydrate avoidance methods, including process solutions, hydrodynamic methods, thermal methods, and chemical injections (e.g., methanol and mono ethylene glycol) help the systems keep out of the hydrate stability zone. However, the offshore oil/gas industry is more interested in the hydrate management methods [100-103]. In this approach, gas hydrates are allowed to form in pipelines, but are controlled by injecting a small amount of low-dosage hydrate inhibitors (LDHIs) into flowlines. LDHIs include two categories, including anti-agglomerates (AAs) and kinetic hydrate inhibitors (KHIs). AAs form a transportable hydrate slurry, while KHIs delay hydrate formation. Hydrate management is gaining more interest in the industry because small amounts of these chemicals are needed (where only 2 vol% LDHI is used compared with 40 vol% thermodynamic inhibitors) [71].

The gas hydrate formation experiments were conducted for the mixtures of methane/ethane gases in the presence of KHIs such as GHI 101 (gas hydrate inhibitor 101) and Luvicap EG at the pressure of 5100 kPa and the temperature of 273.7 K (and/or 273.9 K). Based on the results, the hydrate formation is postponed when GHI 101 (gas hydrate inhibitor 101) and Luvicap EG are added to the experiment samples. However, adding polyethylene oxide to the samples with KHIs

decreased the effect of hydrate memory on the induction time [104]. The methane hydrate formation in the presence of Luvicap 55W in the seven independent multiple high-pressure stirred automated lag time apparatuses (HPS-ALTA) was studied by Lim et al. (2021). They collected over 3000 experimental points to investigate the effect of Luvicap 55W as a KHI (0 – 3 wt% in the water) on the methane hydrate formation in terms of subcooling and initial growth rate parameters with the operating pressure of about 12 MPa. Their results showed that adding KHI to the samples leads to the measured induction times for the same samples being more repeatable, implying a decrease in the stochastic behavior of methane hydrate in these systems. However, the average initial hydrate growth rate decreased by a factor of five for these samples [105]. The effect of glycol ether was studied in the case of the natural gas hydrate formation in the presence of Luvicap 55 W with a temperature of 4 °C and pressure of 95 bar. According to the results, the glycol ether with different concentrations does not impact the induction time, while increasing the glycol ether concentration decreases the growth rate of the hydrate for these systems in the stirred reactor [106].

### **1.3 RESEARCH CONTRIBUTION**

Despite all efforts that have been accomplished to identify the best method to manage and control hydrate formation in oil facilities, hydrate formation remains a challenge for the industry, and more research investigations are needed to find reliable/effective methods for hydrate management.

Although research on gas hydrates in oil and gas facilities has been investigated over several decades, hydrate studies for the complicated geometries exposing a high risk of hydrate formation still need in-depth assessment. Thus, the knowledge gap for the hydrate formation investigation in subsea facilities such as jumpers, which are not well-understood is undeniable. Therefore, more research is vital to be accomplished to study hydrate formation in complicated geometries such as

a jumper and investigate the effects of fluid properties on hydrate formation in these geometries. In addition, although kinetic hydrate inhibitors such as Luvicap 55 W are applied to postpone gas hydrate formation in oil and gas facilities (as a hydrate management strategy), there are no sufficient expressions/models in the literature to show the relationship between process conditions and induction time for the methane hydrate systems in the presence of Luvicap 55 W. Therefore, research on hydrate formation with/without inhibitors is still needed to be performed to develop a practical model to indicate the relation between the induction time and process conditions. Stirred reactors are one of the popular experimental apparatuses to study hydrate formation/dissociation in terms of kinetics and thermodynamics prospects; however, there are rarely research simulation studies on hydrate formation/dissociation in stirred reactors using CFD software in the literature. Hence, more studies need to be performed to fill in this knowledge gap.

## **1.4 THESIS ORGANIZATION**

The current study (first chapter) further highlights the efforts made on hydrate formation and deposition in subsea pipelines experimentally and theoretically. This study is intended to further explore important aspects of hydrate formation mechanisms and modeling, experimental apparatuses, different natural gas hydrate prevention and mitigation techniques, low dose hydrate inhibitors, and simulation tools such as computational fluid dynamics and machine learning models. This thesis consists of three manuscripts (either published or under review for publication), as listed below:

The second chapter was published in the Journal of Natural Gas Science and Engineering. In this study, the methane hydrate formation in a jumper was investigated using the Eulerian multiphase flow model through employing computational fluid dynamic (CFD) software (STAR CCM+). In addition, the effects of changes in the inlet fluid velocity, gas volume fraction, inlet temperature,

and subcooling on the hydrate formation were studied. It is found that the developed CFD model is able to simulate the methane hydrate formation behaviors in the jumper with acceptable precision. The amount of hydrate in the jumper decreases with an increase in liquid inlet velocity and gas inlet temperature. In contrast, increasing subcooling and gas volume fraction helps to increase hydrate formation in the jumper.

The third chapter was published in the Journal of Molecular Liquids. In this chapter, induction time was predicted for the water + methane + Luvicap 55 W systems with a broad range of concentrations. The artificial intelligence models, including least squares, support vector machine (LSSVM), adaptive network-based fuzzy inference system (ANFIS), and gene expression programming (GEP), are employed in this study to predict induction time as a target parameter. However, the molecular weight of the solution, mass fraction of KHI, temperature, pressure, and subcooling parameters are considered as the inputs. 440 experimental data were collected, where 85% of the data was utilized for the training step and 15% for the testing step. The key statistical parameters, including average relative error percent (ARE %), average absolute relative error (AARE %), and coefficient of determination ( $R^2$ ) were calculated to evaluate the performance of the smart models. According to the results of these models in the training and testing phases, the GEP model exhibits greater performance for induction time estimation compared with the LSSVM and ANFIS models. Sensitivity analysis for the ANFIS model using the correlation coefficient method indicates that the system pressure and temperature are the most influential parameters affecting the induction time. In addition, other input parameters, such as the molecular weight of the solution, mass fraction of the Luvicap 55 W, and subcooling, exhibit an indirect relationship with the induction time.

The fourth chapter was submitted to the Journal of Natural Gas Science and Engineering. This manuscript investigates methane hydrate formation in the stirred reactor using computational fluid dynamics (Star CCM<sup>+</sup> software). The developed numerical model considers the conservation equations of momentum, mass, and energy, where the hydrate equations, including mass transfer, hydrate kinetics, and heat of hydrate formation, are incorporated into the mass and energy equations. In this work, methane hydrate formation in the stirred reactor for the stirring rate of 300 RPM, a volume fraction of 0.04, and a pressure of 55 bar was simulated. Then, the results of the model were validated with the experimental data collected from the literature. In addition, the data analysis was performed to study the influence of stirring rate, methane volume fraction, and subcooling on the hydrate formation in the stirred reactor. The simulation results reveal that methane hydrate is mainly formed near the walls and around the stirrer blades. In addition, the subcooling, gas volume fraction, and stirring rate have a positive impact on methane hydrate formation in the agitated reactor so increasing these parameters leads to more hydrate formation in the reactor.

## References

1. Sloan, E.D., *Gas hydrates: review of physical/chemical properties*. Energy & fuels, 1998. **12**(2): p. 191-196.
2. Sloan Jr, E.D. and C.A. Koh, *Clathrate hydrates of natural gases*. 2007: CRC press.
3. Gabitto, J.F. and C. Tsouris, *Physical properties of gas hydrates: A review*. Journal of Thermodynamics, 2010. **2010**.
4. Huot, K., M. White, and T. Acharya, *Natural Gas Hydrates: A Review of Formation, and Prevention/Mitigation in Subsea Pipelines*. Advanced Science, Engineering and Medicine, 2019. **11**(6): p. 453-464.
5. Sloan, E.D., *Natural gas hydrates in flow assurance*. 2010: Gulf Professional Publishing.
6. Ross, R., P. Andersson, and G. Bäckström, *Unusual PT dependence of thermal conductivity for a clathrate hydrate*. Nature, 1981. **290**(5804): p. 322-323.
7. Sharma, S., A. Saxena, and N. Saxena, *Unconventional Resources in India: The Way Ahead*. Springer.
8. Jasamai, M., M. Idress, M.Z. Arshad, and M.F. Taha, *Mitigation of methane hydrate blockage in subsea pipelines using ionic liquid as hydrate inhibitor*. Platform: A Journal of Engineering, 2019. **3**(1): p. 13-18.
9. Chatti, I., A. Delahaye, L. Fournaison, and J.-P. Petitet, *Benefits and drawbacks of clathrate hydrates: a review of their areas of interest*. Energy conversion and management, 2005. **46**(9-10): p. 1333-1343.
10. Jassim, E., M.A. Abdi, and Y. Muzychka, *A new approach to investigate hydrate deposition in gas-dominated flowlines*. Journal of natural gas science and engineering, 2010. **2**(4): p. 163-177.

11. Borden, K., *Flow Assurance: Hydrates and Paraffin Management*. Oil and Gas Facilities, 2014. **3**(01): p. 29-33.
12. Camargo, R., M. Gonçalves, J. Montesanti, C. Cardoso, and K. Minami. *A perspective view of flow assurance in deepwater fields in Brazil*. in *Offshore Technology Conference*. 2004. Offshore Technology Conference.
13. Turner, D., J. Boxall, S. Yang, D. Kleehammer, C. Koh, K. Miller, E. Sloan, Z. Xu, P. Matthews, and L. Talley. *Development of a hydrate kinetic model and its incorporation into the OLGA2000® transient multiphase flow simulator*. in *5th International Conference on Gas Hydrates, Trondheim, Norway*. 2005.
14. Zerpa, L.E., E.D. Sloan, A.K. Sum, and C.A. Koh, *Overview of CSMHyK: A transient hydrate formation model*. Journal of Petroleum Science and Engineering, 2012. **98**: p. 122-129.
15. Boxall, J.A., C.A. Koh, E.D. Sloan, A.K. Sum, and D.T. Wu, *Droplet size scaling of water-in-oil emulsions under turbulent flow*. Langmuir, 2011. **28**(1): p. 104-110.
16. Zerpa, L.E., Z.M. Aman, S. Joshi, I. Rao, E.D. Sloan, C. Koh, and A. Sum. *Predicting hydrate blockages in oil, gas and water-dominated systems*. in *Offshore Technology Conference*. 2012. Offshore Technology Conference.
17. Wang, Z., J. Zhang, L. Chen, Y. Zhao, W. Fu, J. Yu, and B. Sun, *Modeling of hydrate layer growth in horizontal gas-dominated pipelines with free water*. Journal of Natural Gas Science and Engineering, 2018. **50**: p. 364-373.
18. Song, G., Y. Li, W. Wang, K. Jiang, Z. Shi, and S. Yao, *Investigation on the mechanical properties and mechanical stabilities of pipewall hydrate deposition by modelling and numerical simulation*. Chemical Engineering Science, 2018. **192**: p. 477-487.

19. Joshi, S., E.D. Sloan, C. Koh, and A. Sum. *Micromechanical adhesion force measurements between cyclopentane hydrate particles in water*. in *7th International Conference of Gas Hydrates, ICGH, Edinburgh, Scotland*. 2011.
20. Kashchiev, D. and A. Firoozabadi, *Nucleation of gas hydrates*. Journal of crystal growth, 2002. **243**(3-4): p. 476-489.
21. Kashchiev, D. and A. Firoozabadi, *Driving force for crystallization of gas hydrates*. Journal of crystal growth, 2002. **241**(1-2): p. 220-230.
22. Ke, W., T.M. Svartaas, and D. Chen, *A review of gas hydrate nucleation theories and growth models*. Journal of Natural Gas Science and Engineering, 2018.
23. Vysniauskas, A. and P. Bishnoi, *A kinetic study of methane hydrate formation*. Chemical Engineering Science, 1983. **38**(7): p. 1061-1072.
24. Skovborg, P., H. Ng, P. Rasmussen, and U. Mohn, *Measurement of induction times for the formation of methane and ethane gas hydrates*. Chemical Engineering Science, 1993. **48**(3): p. 445-453.
25. Natarajan, V., P. Bishnoi, and N. Kalogerakis, *Induction phenomena in gas hydrate nucleation*. Chemical Engineering Science, 1994. **49**(13): p. 2075-2087.
26. Christiansen, R.L. and E.D. Sloan Jr, *Mechanisms and kinetics of hydrate formation*. Annals of the New York Academy of Sciences, 1994. **715**(1): p. 283-305.
27. Anklam, M.R. and A. Firoozabadi, *Driving force and composition for multicomponent gas hydrate nucleation from supersaturated aqueous solutions*. The Journal of chemical physics, 2004. **121**(23): p. 11867-11875.

28. Davies, S.R., K.C. Hester, J.W. Lachance, C.A. Koh, and E.D. Sloan, *Studies of hydrate nucleation with high pressure differential scanning calorimetry*. Chemical Engineering Science, 2009. **64**(2): p. 370-375.
29. Fandiño, O. and L. Ruffine, *Methane hydrate nucleation and growth from the bulk phase: Further insights into their mechanisms*. Fuel, 2014. **117**: p. 442-449.
30. Taylor, C.J., L.E. Dieker, K.T. Miller, C.A. Koh, and E.D. Sloan Jr, *Micromechanical adhesion force measurements between tetrahydrofuran hydrate particles*. Journal of Colloid and Interface Science, 2007. **306**(2): p. 255-261.
31. Mori, Y.H., *Estimating the thickness of hydrate films from their lateral growth rates: application of a simplified heat transfer model*. Journal of crystal growth, 2001. **223**(1-2): p. 206-212.
32. Kato, M., T. Iida, and Y.H. Mori, *Drop formation behaviour of a hydrate-forming liquid in a water stream*. Journal of Fluid Mechanics, 2000. **414**: p. 367-378.
33. Shindo, Y., P.C. Lund, Y. Fujioka, and H. Komiyama, *Kinetics and mechanism of the formation of CO<sub>2</sub> hydrate*. International journal of chemical kinetics, 1993. **25**(9): p. 777-782.
34. Yin, Z., M. Khurana, H.K. Tan, and P. Linga, *A review of gas hydrate growth kinetic models*. Chemical Engineering Journal, 2018. **342**: p. 9-29.
35. Yin, Z., Z.R. Chong, H.K. Tan, and P. Linga, *Review of gas hydrate dissociation kinetic models for energy recovery*. Journal of Natural Gas Science and Engineering, 2016. **35**: p. 1362-1387.

36. Englezos, P., N. Kalogerakis, P. Dholabhai, and P. Bishnoi, *Kinetics of gas hydrate formation from mixtures of methane and ethane*. Chemical engineering science, 1987. **42**(11): p. 2659-2666.
37. Skovborg, P. and P. Rasmussen, *A mass transport limited model for the growth of methane and ethane gas hydrates*. Chemical Engineering Science, 1994. **49**(8): p. 1131-1143.
38. Uchida, T., T. Ebinuma, J.i. Kawabata, and H. Narita, *Microscopic observations of formation processes of clathrate-hydrate films at an interface between water and carbon dioxide*. Journal of crystal growth, 1999. **204**(3): p. 348-356.
39. Mork, M. and J.S. Gudmundsson. *Hydrate formation rate in a continuous stirred tank reactor: Experimental results and bubble-to-crystal model*. in *4th International Conference on Gas Hydrates*. 2002. Citeseer.
40. Clarke, M.A. and P. Bishnoi, *Determination of the intrinsic kinetics of CO<sub>2</sub> gas hydrate formation using in situ particle size analysis*. Chemical engineering science, 2005. **60**(3): p. 695-709.
41. Turner, D.J., K.T. Miller, and E.D. Sloan, *Methane hydrate formation and an inward growing shell model in water-in-oil dispersions*. Chemical Engineering Science, 2009. **64**(18): p. 3996-4004.
42. Shi, B.-H., J. Gong, C.-Y. Sun, J.-K. Zhao, Y. Ding, and G.-J. Chen, *An inward and outward natural gas hydrates growth shell model considering intrinsic kinetics, mass and heat transfer*. Chemical engineering journal, 2011. **171**(3): p. 1308-1316.
43. Zerpa, L.E., I. Rao, Z.M. Aman, T.J. Danielson, C.A. Koh, E.D. Sloan, and A.K. Sum, *Multiphase flow modeling of gas hydrates with a simple hydrodynamic slug flow model*. Chemical Engineering Science, 2013. **99**: p. 298-304.

44. Wang, Z., Y. Zhao, B. Sun, L. Chen, J. Zhang, and X. Wang, *Modeling of hydrate blockage in gas-dominated systems*. Energy & Fuels, 2016. **30**(6): p. 4653-4666.
45. Vysniauskas, A. and P. Bishnoi, *Kinetics of ethane hydrate formation*. Chemical Engineering Science, 1985. **40**(2): p. 299-303.
46. Englezos, P., N. Kalogerakis, P. Dholabhai, and P. Bishnoi, *Kinetics of formation of methane and ethane gas hydrates*. Chemical Engineering Science, 1987. **42**(11): p. 2647-2658.
47. Ribeiro Jr, C.P. and P.L. Lage, *Modelling of hydrate formation kinetics: State-of-the-art and future directions*. Chemical Engineering Science, 2008. **63**(8): p. 2007-2034.
48. Windmeier, C. and L.R. Oellrich, *Visual observation of the methane hydrate formation and dissociation process*. Chemical Engineering Science, 2014. **109**: p. 75-81.
49. Meindinyo, R.-E.T., T.M. Svartaas, T.N. Nordbø, and R. Bøe, *Gas hydrate growth estimation based on heat transfer*. Energy & Fuels, 2015. **29**(2): p. 587-594.
50. Herri, J.-M., F. Gruy, J.-S. Pic, M. Cournil, B. Cingotti, and A. Sinquin, *Interest of in situ turbidimetry for the characterization of methane hydrate crystallization: Application to the study of kinetic inhibitors*. Chemical Engineering Science, 1999. **54**(12): p. 1849-1858.
51. Lederhos, J., J. Long, A. Sum, R. Christiansen, and E. Sloan Jr, *Effective kinetic inhibitors for natural gas hydrates*. Chemical Engineering Science, 1996. **51**(8): p. 1221-1229.
52. Skiba, S. and A.Y. Manakov. *Study of self-preservation of gas hydrates in suspensions in oils*. in *Journal of Physics: Conference Series*. 2019. IOP Publishing.
53. Farhadian, A., A. Kudbanov, M.A. Varfolomeev, and D. Dalmazzone, *Waterborne polyurethanes as a new and promising class of kinetic inhibitors for methane hydrate formation*. Scientific reports, 2019. **9**(1): p. 1-10.

54. Du, J., H. Li, and L. Wang, *Cooperative effect of surfactant addition and gas-inducing agitation on methane hydrate formation rate*. Fuel, 2018. **230**: p. 134-137.
55. Qureshi, M.F., M. Atilhan, T. Altamash, S. Aparicio, M. Aminnaji, and B. Tohidi, *High-pressure gas hydrate autoclave hydraulic experiments and scale-up modeling on the effect of stirring RPM effect*. Journal of Natural Gas Science and Engineering, 2017. **38**: p. 50-58.
56. Meindinyo, R.-E. and T. Svartaas, *Gas hydrate growth kinetics: a parametric study*. Energies, 2016. **9**(12): p. 1021.
57. Odutola, T., J. Ajienka, M. Onyekonwu, and S. Ikiensikimama, *Design, Fabrication and Validation of a Laboratory Flow Loop for Hydrate Studies*. American Journal of Chemical Engineering, 2017. **5**(3-12): p. 28-41.
58. Stoporev, A.S., A.P. Semenov, V.I. Medvedev, A.A. Sizikov, P.A. Gushchin, V.A. Vinokurov, and A.Y. Manakov, *Visual observation of gas hydrates nucleation and growth at a water–organic liquid interface*. Journal of Crystal Growth, 2018. **485**: p. 54-68.
59. Sa, J.-H., A. Melchuna, X. Zhang, R. Morales, A. Cameirao, J.-M. Herri, and A.K. Sum, *Rock-Flow Cell: An Innovative Benchtop Testing Tool for Flow Assurance Studies*. Industrial & Engineering Chemistry Research, 2019. **58**(19): p. 8544-8552.
60. Boxall, J., S. Davies, J. Nicholas, C. Koh, E.D. Sloan, D. Turner, and L. Talley. *Hydrate blockage potential in an oil-dominated system studied using a four inch flow loop*. in *Proceedings of the 6th International Conference on Gas Hydrates, Vancouver, BC, Canada*. 2008.

61. Nicholas, J.W., C.A. Koh, E.D. Sloan, L. Nuebling, H. He, and B. Horn, *Measuring hydrate/ice deposition in a flow loop from dissolved water in live liquid condensate*. *AIChE Journal*, 2009. **55**(7): p. 1882-1888.
62. Wang, W., S. Fan, D. Liang, and Y. Li, *Experimental study on flow characteristics of tetrahydrofuran hydrate slurry in pipelines*. *Journal of Natural Gas Chemistry*, 2010. **19**(3): p. 318-322.
63. Vijayamohan, P., A. Majid, P. Chaudhari, E.D. Sloan, A.K. Sum, C.A. Koh, E. Dellacase, and M. Volk. *Hydrate modeling & flow loop experiments for water continuous & partially dispersed systems*. in *Offshore Technology Conference*. 2014. Offshore Technology Conference.
64. Fu, W., Z. Wang, W. Duan, Z. Zhang, J. Zhang, and B. Sun, *Characterizing methane hydrate formation in the non-Newtonian fluid flowing system*. *Fuel*, 2019. **253**: p. 474-487.
65. Rao, Y., Z. Wang, S. Wang, and M. Yang, *Investigation on gas hydrate slurry pressure drop properties in a spiral flow loop*. *Energies*, 2018. **11**(6): p. 1384.
66. Peng, B.-Z., J. Chen, C.-Y. Sun, A. Dandekar, S.-H. Guo, B. Liu, L. Mu, L.-Y. Yang, W.-Z. Li, and G.-J. Chen, *Flow characteristics and morphology of hydrate slurry formed from (natural gas+ diesel oil/condensate oil+ water) system containing anti-agglomerant*. *Chemical engineering science*, 2012. **84**: p. 333-344.
67. Straume, E.O., C. Kakitani, D. Merino-Garcia, R.E. Morales, and A.K. Sum, *Experimental study of the formation and deposition of gas hydrates in non-emulsifying oil and condensate systems*. *Chemical Engineering Science*, 2016. **155**: p. 111-126.

68. Chen, J., K.-L. Yan, G.-J. Chen, C.-Y. Sun, B. Liu, N. Ren, D.-J. Shen, M. Niu, Y.-N. Lv, and N. Li, *Insights into the formation mechanism of hydrate plugging in pipelines*. Chemical Engineering Science, 2015. **122**: p. 284-290.
69. Ding, L., B. Shi, X. Lv, Y. Liu, H. Wu, W. Wang, and J. Gong, *Hydrate formation and plugging mechanisms in different gas–liquid flow patterns*. Industrial & Engineering Chemistry Research, 2017. **56**(14): p. 4173-4184.
70. Majid, A.A., G. Grasso, J.L. Creek, H. Qin, T. Charlton, D. Estanga, M. Rivero, B. Bbosa, A. Waturuocha, and M. Volk. *A review of hydrate formation for partially dispersed systems in multiphase flow conditions and the detection of hydrate deposits*. in *Offshore Technology Conference*. 2017. Offshore Technology Conference.
71. Majid, A.A., W. Lee, V. Srivastava, L. Chen, P. Warriar, G. Grasso, P. Vijayamohan, P. Chaudhari, E.D. Sloan, and C.A. Koh, *Experimental investigation of gas-hydrate formation and particle transportability in fully and partially dispersed multiphase-flow systems using a high-pressure flow loop*. SPE Journal, 2018. **23**(03): p. 937-951.
72. Lv, X., J. Gong, W. Li, B. Shi, D. Yu, and H. Wu, *Experimental study on natural-gas-hydrate-slurry flow*. Spe Journal, 2013. **19**(02): p. 206-214.
73. Di Lorenzo, M., Z.M. Aman, G. Sanchez Soto, M. Johns, K.A. Kozielski, and E.F. May, *Hydrate formation in gas-dominant systems using a single-pass flowloop*. Energy & Fuels, 2014. **28**(5): p. 3043-3052.
74. Kumar, A., M. Di Lorenzo, K. Kozielski, A. Singh, E.F. May, and Z.M. Aman. *Hydrate Management in Restart Operations of a Subsea Jumper*. in *Offshore Technology Conference Asia*. 2020. OnePetro.

75. Kumar, A., M. Di Lorenzo, K. Kozielski, P. Glénat, E. F May, and Z. M Aman. *Hydrate blockage assessment in a pilot-scale subsea jumper*. in *Offshore Technology Conference*. 2020. OnePetro.
76. Herri, J.-M., J.-S. Pic, F. Gruy, and M. Cournil, *Methane hydrate crystallization mechanism from in-situ particle sizing*. *AIChE Journal*, 1999. **45**(3): p. 590-602.
77. Hussain, S., A. Kumar, S. Laik, A. Mandal, and I. Ahmad, *Study of the kinetics and morphology of gas hydrate formation*. *Chemical Engineering & Technology: Industrial Chemistry-Plant Equipment-Process Engineering-Biotechnology*, 2006. **29**(8): p. 937-943.
78. Meindinyo, R.-E.T. and T.M. Svartaas, *Gas hydrate growth kinetics: a parametric study*. *Energies*, 2016. **9**(12): p. 1021.
79. Longinos, S.N. and M. Parlaktuna, *Examination of methane hydrate formation by the use of dual impeller combinations*. *Reaction Kinetics, Mechanisms and Catalysis*, 2021. **133**(2): p. 729-740.
80. Davies, S.R., J.A. Boxall, C. Koh, E.D. Sloan, P.V. Hemmingsen, K.J. Kinnari, and Z.-G. Xu, *Predicting hydrate-plug formation in a subsea tieback*. *SPE Production & Operations*, 2009. **24**(04): p. 573-578.
81. Creek, J.L., S. Subramanian, and D.A. Estanga. *New method for managing hydrates in deepwater tiebacks*. in *Offshore Technology Conference*. 2011. Offshore Technology Conference.
82. Norris, B.W., L.E. Zerpa, C.A. Koh, M.L. Johns, E.F. May, and Z.M. Aman, *Rapid assessments of hydrate blockage risk in oil-continuous flowlines*. *Journal of Natural Gas Science and Engineering*, 2016. **30**: p. 284-294.

83. Zi, M., D. Chen, and G. Wu, *Molecular dynamics simulation of methane hydrate formation on metal surface with oil*. Chemical Engineering Science, 2018. **191**: p. 253-261.
84. Zhang, D., Q. Huang, H. Zheng, W. Wang, X. Cheng, R. Li, and W. Li, *Effect of Wax Crystals on Nucleation during Gas Hydrate Formation*. Energy & Fuels, 2019.
85. Zi, M., D. Chen, H. Ji, and G. Wu, *Effects of asphaltenes on the formation and decomposition of methane hydrate: a molecular dynamics study*. Energy & Fuels, 2016. **30**(7): p. 5643-5650.
86. Sule, I., A. Adedeji, C. Obeng, A. Okosun, M. Morshed, M. Rahman, and K. Hawboldt, *CFD analysis of hydrate formation in pipelines*. Petroleum Science and Technology, 2015. **33**(5): p. 571-578.
87. Jujuly, M., M.A. Rahman, A. Maynard, and M. Adey, *Hydrate-induced vibration in an offshore pipeline*. SPE Journal, 2020. **25**(02): p. 732-743.
88. Yao, S., Y. Li, W. Wang, G. Song, Z. Shi, X. Wang, and S. Liu, *Investigation of hydrate slurry flow behaviors in deep-sea pipes with different inclination angles*. Oil & Gas Science and Technology–Revue d'IFP Energies nouvelles, 2019. **74**: p. 48.
89. Lo, S. *CFD modelling of hydrate formation in oil-dominated flows*. in *Offshore Technology Conference*. 2011. OnePetro.
90. Balakin, B., A. Hoffmann, P. Kosinski, and S. Høiland, *Turbulent flow of hydrates in a pipeline of complex configuration*. Chemical engineering science, 2010. **65**(17): p. 5007-5017.
91. Balakin, B., A. Hoffmann, and P. Kosinski, *Experimental study and computational fluid dynamics modeling of deposition of hydrate particles in a pipeline with turbulent water flow*. Chemical Engineering Science, 2011. **66**(4): p. 755-765.

92. Yarveicy, H. and M.M. Ghiasi, *Modeling of gas hydrate phase equilibria: Extremely randomized trees and LSSVM approaches*. Journal of Molecular Liquids, 2017. **243**: p. 533-541.
93. Kamari, A., A. Bahadori, A.H. Mohammadi, and S. Zendehboudi, *New tools predict monoethylene glycol injection rate for natural gas hydrate inhibition*. Journal of Loss Prevention in the Process Industries, 2015. **33**: p. 222-231.
94. Mesbah, M., S. Habibnia, S. Ahmadi, A.H.S. Dehaghani, and S. Bayat, *Developing a robust correlation for prediction of sweet and sour gas hydrate formation temperature*. Petroleum, 2020.
95. Mesbah, M., E. Soroush, and M. Rezakazemi, *Development of a least squares support vector machine model for prediction of natural gas hydrate formation temperature*. Chinese journal of chemical engineering, 2017. **25**(9): p. 1238-1248.
96. Mehrizadeh, M., *Prediction of gas hydrate formation using empirical equations and data-driven models*. Materials Today: Proceedings, 2021. **42**: p. 1592-1598.
97. Amar, M.N., *Prediction of hydrate formation temperature using gene expression programming*. Journal of Natural Gas Science and Engineering, 2021. **89**: p. 103879.
98. Qin, H., V. Srivastava, H. Wang, L.E. Zerpa, and C.A. Koh. *Machine Learning Models to Predict Gas Hydrate Plugging Risks Using Flowloop and Field Data*. in *Offshore Technology Conference*. 2019. Offshore Technology Conference.
99. Yarveicy, H., M.M. Ghiasi, and A.H. Mohammadi, *Determination of the gas hydrate formation limits to isenthalpic Joule–Thomson expansions*. Chemical Engineering Research and Design, 2018. **132**: p. 208-214.
100. Creek, J., *Efficient hydrate plug prevention*. Energy & Fuels, 2012. **26**(7): p. 4112-4116.

101. Aja, O.C. and M. Ramasamy, *Thermal management of flow assurance challenges in offshore fields-a review*. 2006.
102. Paez, J. and R. Blok. *Problems in hydrates: mechanisms and elimination methods*. in *SPE Production and Operations Symposium*. 2001. Society of Petroleum Engineers.
103. Wu, M., S. Wang, and H. Liu, *A study on inhibitors for the prevention of hydrate formation in gas transmission pipeline*. *Journal of Natural Gas Chemistry*, 2007. **16**(1): p. 81-85.
104. Lee, J.D. and P. Englezos, *Unusual kinetic inhibitor effects on gas hydrate formation*. *Chemical Engineering Science*, 2006. **61**(5): p. 1368-1376.
105. Lim, V.W., P.J. Metaxas, M.L. Johns, G. Haandrikman, D. Crosby, Z.M. Aman, and E.F. May, *The delay of gas hydrate formation by kinetic inhibitors*. *Chemical Engineering Journal*, 2021. **411**: p. 128478.
106. Khatinzadeh, G., S. Taghipoor, A. Mehdizadeh, and A. Roozbehani, *Synergistic Effect of Glycol Ethers with a Kinetic Inhibitor (Poly (VP-VCap)) for Sweet Natural Gas Hydrate Formation:(Concentration Effect of Glycol Ethers)*. *Journal of Petroleum Science and Technology*, 2019. **9**(2): p. 46-53.

## **2.CHAPTER TWO**

# **Computational Fluid Dynamic Modeling of Methane Hydrate Formation in Subsea Jumper**

### **Preface**

A version of this manuscript has been published in the Journal of Natural Gas Science and Engineering Volume 98, February 2022, 104381. Marziyeh Zare, Vandad Talimi, Sohrab Zendehboudi, and Majid Abedinzadegan Abdi are the authors of this paper. The first author (Marziyeh Zare) prepared this paper with the help of the co-authors. The literature review, methodology, simulations, and results analysis were performed by the first author. Vandad Talimi provided advice for simulations and checked the results. The first draft of this paper was written by Marziyeh Zare and revised by co-authors. The feedback from co-authors, Vandad Talimi, Sohrab Zendehboudi, Majid Abedinzadegan Abdi, and journal reviewers were applied by the first author. Co-authors supervised the first author in the project and edited the manuscript.

## **ABSTRACT**

Gas hydrate in subsea pipelines is a serious flow assurance issue that may impose operational challenges to offshore petroleum production and transportation. The effects of fluid properties on hydrate formation in complex geometries such as jumpers are not fully understood. This study aims to assess hydrate formation in the jumper for the water-methane system using the Eulerian multiphase flow model through employing computational fluid dynamic (CFD) software (STAR CCM+). The numerical model is developed through consideration of transport phenomena equations, including conservation of mass, momentum, and energy in which mass transfer, hydrate reaction kinetics model, and heat of hydrate formation are incorporated in the multiphase flow equations in the form of source terms in the CFD software. In this study, first, the hydrate mass fraction for the fluid velocity of 5 m/s with an inlet temperature of 7 °C and a gas volume fraction of 0.2 is calculated. The sensitivity analysis is then performed considering the influences of changes in the inlet fluid velocity, gas volume fraction, inlet temperature, and subcooling on the hydrate formation. The results reveal that the developed CFD model is capable of predicting hydrate formation behaviors in the jumper with acceptable precision. An increase in liquid inlet velocity and gas inlet temperature lowers the amount of hydrate formed in the jumper. In contrast, an increase in subcooling and gas volume fraction leads to more hydrate formation. The proposed CFD model can be successfully used to simulate hydrate formation in pipelines under various process and thermodynamic conditions so that it can help to find reliable/effective methods for hydrate management.

**Keywords:** Hydrate formation; Sensitivity analysis; Methane; Jumper; Computational fluid dynamic

## 2.1 INTRODUCTION

Gas hydrate is a crystal ice structure including a mixture of gas and water molecules in which gas molecules are trapped in cages with water molecules [1-3]. In general, there are three types of hydrate structures: cubic I, cubic II, and hexagonal H [4]. Gas hydrate can be a threat to oil and gas facilities, particularly for offshore in normal and transient operations when the appropriate circumstances (high pressures and low temperatures) for hydrate formation occur. Transient conditions such as shut-in and start-up are at a high risk of hydrate formation because the pipeline conditions might go toward higher pressures and lower temperatures. In this situation, water has a chance to accumulate in small areas [1, 5]. Gas hydrate formation is a significant issue that can negatively impact oil and gas production (and transportation), mainly when the hydrate creates a blockage in pipelines. Various strategies, including pressure reduction (e.g., blowdown), injection of chemicals (e.g., methanol or low dosage hydrate inhibitor in shutdown/restart conditions), and electrical heating, can be used to tackle this problem [6-8].

Hydrate blockage in oil and gas facilities can cause a significant economic impact in terms of deferred production and cost remediation, particularly in harsh conditions (e.g., deep water). Financial considerations and safety concerns have motivated most operating companies to manage hydrate formation based on a complete hydrate avoidance strategy. In recent years, this strategy shifted to hydrate risk management [8, 9]. The goal of hydrate avoidance is not to permit to enter the hydrate formation area, while in hydrate risk management, the system can be in the hydrate zone if the risk is acceptable [10]. One of the common methods applied for hydrate avoidance strategy is using thermodynamic inhibitors (including methanol or mono ethylene glycol) and adding them to the free water which may be considerably expensive due to the need for a large amount of inhibitors [11, 12]. However, several methods can be used for hydrate risk management to prevent hydrate plugging in production and transportation systems. For example, the offshore shut-ins condition in which no-touch time is less than 10 hours, and there is no need to follow any

anti-hydrate procedure before restart; in some cases, hydrate kinetic inhibitors, and antiagglomerants can be implemented [8, 11, 12].

Hydrate plug formations may occur during transient and abnormal conditions, such as start-up, restart in an emergency condition, operational shut-in, and inhibitor injection failure; however, hydrate formation does not accumulate in normal operation due to the design of the system for flow assurance [13]. Some offshore oil and gas production occurs approximately at various depths, including deepwater and ultra-deepwater, where hydrate formation can be observed further in subsea facilities (between the wellhead and processing units) due to environmental conditions. Hydrate may form in some equipment in Floating Production Storage and Offloading (FPSOs) system, including subsea trees, manifold, Jumpers, and flowlines. Furthermore, hydrate can block tubings, valves, orifices, and Blowout Preventers (BOP) during drilling operations [14]. Reyna and Stewart [15] reported hydrate formation and plugging during a well-testing operation in deep water (Quad 204 in 2,750' of water) on the UK Atlantic Margin, West of the Shetland Islands. Hydrate formed in the landing tube string between the seafloor and the surface during the initial clean-up period of the well test and then solidified during the initial pressure build-up test. Some reasons, including high pressure and low-temperature conditions, insufficient chemical inhibitor injection, and high produced water, may provide a good condition for hydrate formation in this oil facility. The operators tried many methods to solve the issue of hydrate blockages, such as mechanical force, Depressurisation, chemical inhibitors, coiled tubing, etc. However, the operation with coiled tubing was more successful than other methods [15]. Oil reservoirs in Brazil are located in deep water, where Petrobras operated these fields in the range of 1000 m water depth (WD) in 1998. In these facilities, hydrate formation and agglomeration occurred due to unwashed water left in the pipes and subsea equipment. Removing the hydrate plug and melting it has been accomplished using depressurization, alcohol injection, and fluid circulation which are expensive. However, hydrate problems increased in the later years due to operating oil facilities in higher water depth and operating pressure. Although there are many key elements that may create flow assurance

problems, such as hydrate formation, Petrobras tried to operate the subsea production system by considering the flow assurance items and with more flexibility [16].

## 2.2 REVIEW OF THE LITERATURE

Although many experiments were conducted in high-pressure stirred reactors several years ago [17-25], hydrate formation mechanisms governing in petroleum pipeline systems are different from these experiments. Therefore, researchers attempted to study hydrates formation mechanisms and behaviors using flow loops where their operating conditions are more similar to field process conditions [20, 26]. For instance, Liu et al. [26] developed a visual flow loop at 8 MPa and  $-20\text{ }^{\circ}\text{C}$  in which hydrate nucleation, growth, and deposition during fluid flow can be observed. Such a flow loop could assist in monitoring and understanding the mechanisms of hydrate formation in offshore pipelines [26]. Studies related to methane hydrate formation in the water-continuous flow loop were conducted in different ranges of void fractions (2.6 to 5.0%), velocities (1.24 to 1.57 m/s), subcooling temperatures (4.5 to 7.2  $^{\circ}\text{C}$ ), and hydrate particle concentrations (0 to 0.14 kg/kg). The results showed that higher hydrate formation occurs when the flow velocity increases [27]. The dissociation process of natural gas hydrate in water-in-oil emulsion systems was studied by Shi et al. [28] in a high-pressure flow loop equipped with a beam reflectance measurement (FBRM) probe and a particle video microscope (PVM) probe. The influences of initial pressure, flow rate, and water cut on hydrate dissociation were examined. According to the results, a high-pressure drop was experienced when the hydrate particle agglomeration was observed in the flow loop, which led to increased hydrate plugging risk; therefore, the hydrate dissociating process in this situation requires more accurate monitoring [28]. Aman et al. [29] investigated the hydrate growth and particle deposition rates for gas-dominated systems in a single-pass flow loop with subcooling temperatures varying from 1 to 20  $^{\circ}\text{C}$  and a holdup range of 1 -10 vol %. It was shown that if the gas velocity decreases from 8.7 to 4.6 m/s at a constant subcooling of 6  $^{\circ}\text{C}$ , the total rate of hydrate formation is reduced by six times. However, the hydrate formation rate was much more sensitive to velocity than subcooling (about 40 times). According to various

tests in the laboratory flow loop for gas-dominated systems, hydrate growth over and around the liquid at the bottom of pipes could lead to blockage of flowlines. Based on the tests for an oil-dominated system with moderate water content, the risk of plugging for a system under shut-in conditions could be higher than the oil system with low water content [30]. Kumar et al. (2020) developed a flow loop with a jumper shape (HyJump flow loop), in which 12 pressure and temperature sensors were installed, to estimate the hydrate formation performance in shutdown and restart situations. The preliminary restart gas tests in this flow loop provided the apparent proof of hydrate deposition when the gas velocity was less than 0.26 ft/s [31]. Furthermore, they conducted restart tests by injecting monoethylene glycol (MEG) in the concentration range of 0 – 30 wt%. It was found that hydrate deposition could be prevented considerably using 20 wt % MEG injection. This MEG content is approximately 50 percent less than the amount of thermodynamic inhibitors. It should be noted that 38 wt% MEG is normally used on the commercial scale with the same thermodynamic conditions as those in the experiment [32].

Hydrate formation data, including location, pressure, and temperature, are essential for the oil and gas operating systems. These data are needed to develop suitable models for monitoring and predicting hydrate formation in different circumstances in pipelines. Several simulators and models have been introduced in the literature [33-39]. Olga was the first computational fluid dynamic (CFD) software (transient multiphase model) that has been used to predict the temperature and pressure of flowlines. The value of predicted parameters indicated the conditions of production facilities in terms of hydrate formation contingency and flow assurance problems [40, 41]. Turner et al. [42] from the Center for Hydrates Research, Colorado School of Mines, developed a hydrate kinetic model with a rate constant that can be adjusted using hydrate kinetics data from the literature. This model, coupled with the transient flow simulator OLGA2000 (CSMHyK), and the data obtained from two flow loops (Texaco and ExxonMobil flow loop) were used for the model verification. Researchers from the Colorado School of Mines have improved the accuracy of CSMHyK using various modeling, experimental, pilot, and field results/data [43-46]. CSMHyK is a

transient hydrate formation model developed for oil-dominated systems that include three submodels: kinetic model, transport model, and cold flow model [44].

A new transport model was proposed by Zerpa for oil and water-dominated systems [44]. This model was verified with data of the flow loop and then applied for a subsea tieback system to simulate hydrate formation in oil-dominated pipelines [47]. CFD model, using the ANSYS CFX-workbench 14 software, was used to forecast the hydrate formation behaviors in a subsea pipeline where a sensitivity analysis was performed to explore the impacts of fluid velocity, geometry (diameter), fluid viscosity, and water fraction on hydrate formation. It was concluded that these parameters have significant influences on hydrate formation in flowlines [48]. In their work, the hydrate formation conditions were predicted without including any reaction kinetics rate or methane mass transfer equation in the software. Jujuly et al. [49] employed the CFD software (ANSYS 2019) integrated with a commercial subsea pipeline visualization tool to investigate the effect of gas hydrate flow in pipelines. They used two cases, including a jumper and a pipeline system from the literature, to validate the model. The agglomeration and breakup mechanisms of hydrate were studied using the population balance method (PBM). In addition, they calculated the maximum stress and deformation under different flow rates in different regions of the jumper [49]. The Eulerian–Eulerian two-fluid multiphase flow model, which was combined with the PBM, was used to simulate hydrate slurry flow in pipes with different inclination angles [50]. A pipeline with three phases, including oil (as a continuous phase) and gas bubbles and water droplets as the dispersed phase, was simulated using Star CCM+. This model was developed based on the Eulerian multiphase flow approach in which the equations of dissolved gas in the oil phase, mass transfer of gas from the oil phase to water, and the reaction kinetics of hydrate formation were added to the transport equations to simulate the hydrate formation in the pipeline [51]. Balakin et al. (2010 , 2011) used the Eulerian–Eulerian CFD model to investigate the accumulation of Freon R11 hydrate in a turbulent flow of water. The model was validated using the flow loop data. This model included an expression for variable hydrate particle size which was compared with the data obtained from population balance numerical methods.

Furthermore, they investigated the effect of gravity on the hydrate particles under low Reynolds number conditions [52, 53].

Wellhead trees are connected to manifolds through jumpers with an M-shaped geometry. They are potentially exposed to a high risk of hydrate formation due to considerable driving force during well restart after a long time shutdown. Some studies have been performed in the open literature that has used CFD software to predict hydrate formation in pipelines. Simulation of hydrate formation in subsea jumpers is not well-understood, and there are rarely published papers available for the simulation of hydrate formation in jumpers. Thus, this study aimed to cover this gap. On the other hand, researchers mainly focus on hydrate formation in gas-dominated and oil-dominated systems, while water-dominated systems need to be systematically studied particularly when dealing with high water cuts in mature oil and natural gas fields [27]. In this chapter, for water-dominated systems, the transient turbulent CFD model which is based on Eulerian multiphase flow is employed to investigate the hydrate formation behaviors in a jumper geometry.

## **2.3 CFD MODELING: THEORY AND METHODOLOGY**

CFD is a branch of computational science that has a high potential to solve complicated fluid mechanics problems in a cost-effective way. A CFD problem can be divided into three steps, namely, pre-processing, solving, and post-processing. Geometry selection and mesh creation are accomplished in the pre-processing step while selecting models and considering boundary and initial conditions are a part of the solving step. It is noted that after the solving step, the grid independence test should be conducted before analyzing and visualizing the results in the post-processing step.

### **2.3.1 Model Geometry and Mesh Creation**

The system used in this study is a jumper based on the flow loop which was published by Kumar (2020). They constructed a HyJump flow loop according to subsea jumpers to study the hydrate formation behavior in different situations, including restart and shutdown [31, 32]. The jumper section of this flow

loop is symmetrical; therefore, in this study, only half of the system is considered for simulation purposes. However, the size of the jumper is scaled down to 1/3 of the HyJump flow loop in order to reduce the simulation time. Figure 2-1 depicts the jumper and its dimensions used in this study.

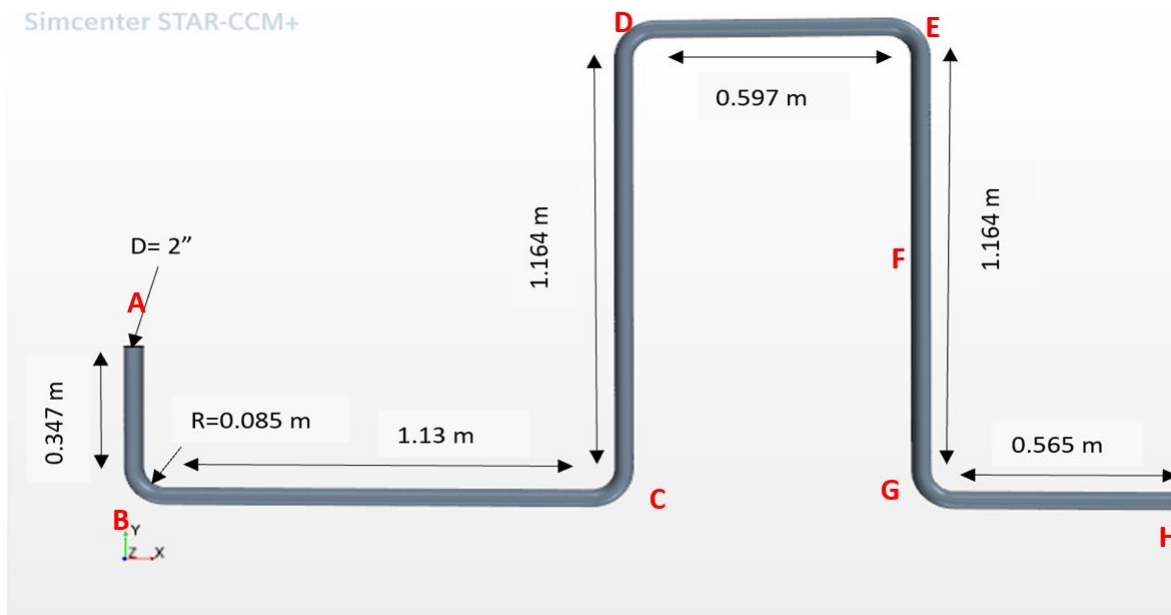


**Figure 2-1.** Three-dimensional CAD model of the jumper.

According to Figure 2-1, the jumper is a three-dimensional system where the total length of the pipes is about 5 m with a diameter of 2'' (5.08 cm). The curvature of the 90° bent sections is five times larger than the pipe with the radius of 10'' (25.4 cm).

In order to solve flow features such as viscous boundary layer gradient and phase distribution, the mesh should be sufficiently fine. Although mesh resolution can have a considerable impact on the simulation results, an increase in the resolution leads to longer simulation runs [54]. The mesh independence test is performed to provide corresponding results for obtaining optimal mesh size. In this study, the mesh independence test is based on the hydrate mass fraction and inlet pressure. Comparing the simulation results for cases with different polyhedral volume cells of 154073, 195797, 223773, and 245471 reveals that the model with 154073 meshes results in an acceptable precision, which is not higher than 3% discrepancy.

The polyhedral mesh includes the four-layer prismatic subsurface near the wall area to take into account the boundary layer effects, as shown in Figure 2-2 .

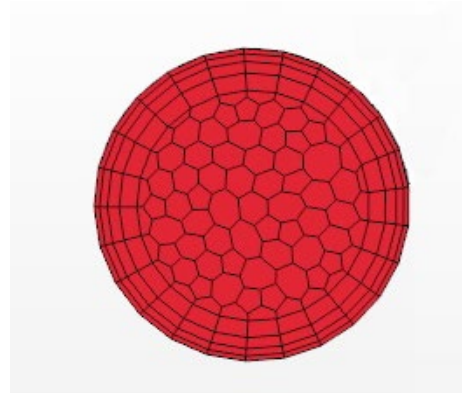


**Figure 2-2.** Polyhedral meshing scheme.

### 2.3.2 Boundary and Initial Conditions

For the jumper, three boundaries are considered in this work, including inlet, outlet, and wall. The fluid velocity is selected as the inlet velocity ranging from 5 to 20 m/s. The outlet boundary is set as an outlet pressure with a value of 100 bar. The wall boundary is a solid wall with a temperature of 4°C and no-slip condition. Table 2-1 lists the boundary parameters that are utilized in the transient model. The values of initial parameters/conditions are also similar to the boundary parameters such as gas volume fraction, temperature, gas axial velocity, and pressure.

**Table 2-1.** Boundary conditions considered for the model.

Parameters	Value
Inlet velocity	5-20 m/s
Outlet pressure	100 bar
Wall temperature	4 °C
Gas volume fraction	0.2-0.5
Inlet temperature	7-25 °C

### 2.3.3 Numerical Model

In this study, the main flow is water that carries hydrate particles and gas bubbles. Two phases are considered, including water plus hydrate as a continuous phase and methane bubbles as a dispersed phase

[51]. The multiphase Eulerian model is selected to study hydrate formation in the jumper. This numerical model is solved by considering the transport equations, including the conservation of mass, momentum, and energy. There are some assumptions with this simulation: 1) although gas and liquid enter the pipe together, the model simulates the liquid phase in which water + hydrate is a continuous fluid, and the gas bubbles form a dispersed phase [55], 2) water is converted to hydrate when it meets the methane gas bubbles, 3) the model is transient, 4) the wall is at the isothermal condition, and 5) interface momentum transfer associated with mass transfer is not considered.

Referring to the second assumption, the phenomenon of methane mass transfer from the gas bubbles to the water to form hydrate should be modeled. The mass fraction of hydrate in the water is called the hydrate fraction (the proportion of water turned into hydrate) and is denoted by  $f_{hyd}$ . When  $f_{hyd} = 0$ , it shows that only pure water exists in the system; when  $f_{hyd} = 1$ , it implies that pure hydrate is in the system.

Thus, the transport equations should be solved to calculate the hydrate fraction in the system.

**Transport equations.** The continuity equation for phase ‘k’ is written as follows [39, 51, 56]:

$$\frac{\partial}{\partial t} \alpha_k \rho_k + \bar{\nabla} \cdot \alpha_k \rho_k \vec{u}_k = \sum_{j=1}^N (\dot{m}_{jk} - \dot{m}_{kj}) \quad (2-1)$$

where  $\alpha_k$  refers to the volume fraction of phase  $k$ ;  $t$  is the time;  $\rho_k$  stands for the phase density;  $\vec{u}_k$  represents the velocity of phase  $k$ ; and  $\dot{m}$  introduces the mass transfer rate. The sum of the volume fractions is equal to 1, as given below:

$$\sum_k \alpha_k = 1 \quad (2-2)$$

The momentum equation for phase  $k$  is given below:

$$\frac{\partial}{\partial t} \alpha_k \rho_k \vec{u}_k + \bar{\nabla} \cdot (\alpha_k \rho_k \vec{u}_k \vec{u}_k) - \bar{\nabla} \cdot (\alpha_k \mu_k (\bar{\nabla} \vec{u}_k + (\bar{\nabla} \vec{u}_k)^T)) = -\alpha_k \bar{\nabla} p + \alpha_k \rho_k \vec{g} + M_k \quad (2-3)$$

where

$$M_K = \sum_{j \neq k} (F_{kj}^D + F_{kj}^{VM} + F_{kj}^{TD}) + \sum_{j=1}^N (\dot{m}_{jk} \vec{u}_j - \dot{m}_{kj} \vec{u}_k) \quad (2-4)$$

where  $\mu_k$  is the phase viscosity;  $p$  denotes the pressure;  $\vec{g}$  refers to gravity acceleration, and  $M$  represents the sum of interfacial forces and momentum associated with the mass transfer.

In this study, the interfacial momentum transfer corresponding to the mass transfer and lift force is not considered; therefore,  $M$  is included in the drag, virtual mass, and turbulent dispersion (or turbulent drag) forces as shown by the following equation [56, 57]:

$$M_K = \sum_{j \neq k} (F_{kj}^D + F_{kj}^{VM} + F_{kj}^{TD}) \quad (2-5)$$

where  $F_{kj}^D$  stands for the drag force;  $F_{kj}^{VM}$  is the virtual mass flow; and  $F_{kj}^{TD}$  refers to the turbulent dispersion force.

The forces are defined as force per cell volume on phase  $k$  due to phase  $j$ , as defined below:

$$F_{jk} = -F_{kj} \quad (2-6)$$

The inter-phase drag force is a function of the drag coefficient and the relative velocity between two phases (gas and liquid) that can be determined by the following expression [56, 57]:

$$F_{kj}^D = \sum_j \frac{1}{2} W_j C_D \rho_c |\vec{u}_j - \vec{u}_k| \left( \frac{a_{kj}}{4} \right) (\vec{u}_j - \vec{u}_k) \quad (2-7)$$

where  $W_j$  denotes the weight function;  $C_D$  symbolizes the drag coefficient; and  $a_{kj}$  represents the interfacial area density [39, 56].  $C_D$  is calculated based on Schiller-Naumann equation [53, 56, 58] as follows:

$$C_D = \begin{cases} \frac{24}{Re_d} (1 + 0.15Re_d^{0.687}) & 0 < Re_d \leq 1000 \\ 0.44 & Re_d > 1000 \end{cases} \quad (2-8)$$

The dispersed Reynolds number ( $Re_d$ ) is calculated by the following equation:

$$Re_d = \frac{\rho_C |\bar{u}_j - \bar{u}_k| l}{\mu_k} \quad (2-9)$$

where  $\rho_C$  introduces the density of the continuous phase;  $\mu_k$  is the dynamic viscosity of the continuous phase; and  $l$  shows the interaction length scale or bubble size [56].

The acceleration of a particle that is submerged in the flow is influenced by the inertia of the surrounding.

This impact is represented as a “virtual mass” in the inviscid flow theory, as written below:

$$F_{kj}^{VM} = C_{VM} \rho_C \alpha_d (a_j - a_k) \quad (2-10)$$

where  $c$  is the continuous phase in the phase interaction  $kj$ ;  $d$  refers to the dispersed phase in the phase interaction  $kj$ ;  $C_{VM}$  introduces the virtual mass coefficient for interaction  $kj$ ; and  $a_j$  and  $a_k$  are the acceleration of phases  $j$  and  $k$ , respectively [56].

The energy conversation for phase  $k$  is given below:

$$\frac{\partial}{\partial t} (\alpha_k \rho_k h_k) + \bar{\nabla} \cdot (\alpha_k \rho_k \bar{u}_k h_k) - \bar{\nabla} \cdot \left[ \alpha_k \left( \lambda_k (\bar{\nabla} T_k + \frac{\mu_{tk}}{\sigma_t} \bar{\nabla} h_k) \right) \right] = Q \quad (2-11)$$

where  $h$  is the phase enthalpy;  $\lambda$  denotes the thermal conductivity;  $\mu$  symbolizes the turbulent viscosity;  $\sigma_t$  is the turbulent Prantle number which is 0.9, and  $Q$  is the heat source [51].

**Hydrate equations.** The summation of volume fraction for two phases (methane gas and water, which contain hydrate) is equal to unity.

$$\alpha_g + \alpha_w = 1 \quad (2-12)$$

The methane hydrate phase is formed based on the chemical reaction when methane gas is dissolved in water in the interphase, as represented below:



where  $n_{CH_4}$ ,  $n_{H_2O}$ , and  $n_{hyd}$  are the stoichiometric coefficients with the values of 1, 5.75, and 1, respectively.

According to continuity equation (2-1), the mass transfer should occur between two phases for the hydrate formation. The continuity equations for the gas, water, and hydrate phases are written as:

$$\frac{\partial}{\partial t}(\alpha_g \rho_g) + \bar{\nabla} \cdot (\alpha_g \rho_g \bar{u}_k) = -\dot{m}_{CH_4} \quad (2-14)$$

$$\frac{\partial}{\partial t}(\alpha_w \rho_w f_w) + \bar{\nabla} \cdot (\alpha_w \rho_w \bar{u}_k f_w) = \dot{m}_{CH_4} \left(1 - \frac{W_{hyd} n_{hyd}}{W_{CH_4} n_{CH_4}}\right) \quad (2-15)$$

$$\frac{\partial}{\partial t}(\alpha_w \rho_w f_{hyd}) + \bar{\nabla} \cdot (\alpha_w \rho_w \bar{u}_k f_{hyd}) = \dot{m}_{CH_4} \left(\frac{W_{hyd} n_{hyd}}{W_{CH_4} n_{CH_4}}\right) \quad (2-16)$$

where  $f_w$  and  $f_{hyd}$  represent the mass fractions of water and hydrate in the liquid phase ( $f_w + f_{hyd} = 1$ );  $W_{hyd}$  (=119.65 kg/mol) refers to the molar mass of methane hydrate;  $W_{CH_4}$  (= 16.04 kg/mol) stands for the molar mass of methane gas; and  $\dot{m}_{CH_4}$  is the amount of methane gas, which is dissolved in the water and then changed to hydrate due to the chemical hydrate reaction [39].

In this work, we assume that hydrate nucleation occurs immediately after a specific subcooling that is introduced by the following equation [43, 44]:

$$\Delta T_{sub} = T_{hyd} - T_{system} \quad (2-17)$$

$\dot{m}_{CH_4}$  is the methane consumption rate, which is calculated using the following intrinsic kinetics equation:

$$-\frac{dm_{gas}}{dt} = uk_1 \exp\left(\frac{k_2}{T_{sys}}\right) A_s (\Delta T_{sub}) \quad (2-18)$$

Methane gas consumption rate is a function of intrinsic rate constants ( $k_1$  and  $k_2$ ), surface area ( $A_s$ ), and subcooling as a driving force which is the difference between hydrate equilibrium temperature and actual system temperature at the system pressure. This intrinsic kinetics equation was proposed by Vysniauskas and Bishnoi (1983) and Englezos et al. (1987) [59, 60]. They conducted some hydrate tests to measure gas consumption rates in different temperatures and subcooling for methane and ethane hydrates without considering mass and heat resistance. The values of  $k_1$  and  $k_2$  were  $7.3548 \times 10^{17}$  and -13600, respectively. To attain a good match with flow loop data, Boxall et al. (2009) suggested a coefficient to correct gas consumption rate ( $u = 1/500$ ) [61]; mass and heat transfer resistances were included in this correction [46].

Hydrate formation is an exothermic reaction. Therefore, the heat of hydrate formation as a function of hydrate equilibrium temperature is used in the energy equation (as a heat source) as given below [51]:

$$\dot{q}_{hyd} = \dot{m}_{CH_4} Cp_{hyd} T_{hyd} \quad (2-19)$$

where  $Cp_{hyd}$  is the heat capacity of hydrate;  $T_{hyd}$  stands for the hydrate equilibrium temperature; and  $\dot{m}_{CH_4}$  resembles the consumption rate of methane gas changed to hydrate.

### 2.3.4 Model Solution

Equations (2-1)-(2-19) are solved using the implicit SIMPLE technique, which is included in the commercial CFD-package STAR-CCM+ revision 15.04.010 where various relaxation factors, including 0.8

for K-Epsilon turbulence, 0.3 for pressure, 0.5 for volume fraction, and 0.9 for segregation species and energy are used. Although equations (2-1)-(2-19) are solved using the built-in solver of STAR-CCM+, this system of nonlinear functional equations (PDE and transcendental) can be solved by a relatively novel and efficient solver called the multistage Adomian decomposition method (MADM) [62-64]. The residual value as the criterion for ending the simulation runs is  $10^{-4}$ . The required parameters for methane and water, such as density, dynamic viscosity, and specific heat, are calculated using PVTsim Nova software. However, the hydrate parameters are adopted from the reference [42]. Table 2-2 lists the key parameters of various phases with their corresponding values. In order to ensure transient stability and numerical accuracy, an appropriate time step is required. Therefore, time steps of 0.1, 0.01, and 0.001 and various simulation times between 1 and 60 seconds are examined to find an appropriate time step and simulation time. The hydrate mass fraction values for different time steps are approximately the same with an acceptable accuracy; thus, the time step of 0.01 with a simulation time of 10 seconds is selected once the system reached a steady-state condition. The standard  $k - \varepsilon$  turbulence and Realizable k-epsilon two-layer are used in this transient model. The model specifications are summarized in Table 2-3.

**Table 2-2.** Values of main parameters used in the model.

<b>Parameter</b>	<b>Value</b>
Water phase density	1000.00 kg/m <sup>3</sup>
Water dynamic viscosity	0.001 Pa-s
Water specific heat	4813.03 J/kg K
Hydrate phase density	807.80 kg/m <sup>3</sup>
Hydrate dynamic viscosity	0.002 Pa-s
Hydrate thermal conductivity	0.34 W/m K
Hydrate specific heat	2100 J/kg K
Methane thermal conductivity	0.05 W/m-K
Methane dynamic viscosity	1.39 E-5 Pa-s
Methane specific heat	3096.4 J/kg K
Hydrate temperature	285.5 K

**Table 2-3.** Model specifications for hydrate formation in the jumper.

Space	Three dimensional
Meshing	Polyhedral with near-wall effect
Simulation type	Implicit unsteady with the time step 0.01 s and time duration of 10 s.
Main model	Eulerian multiphase model
Turbulent Model	Standard $k - \varepsilon$ turbulence, Realizable k-epsilon two-layer
Fluid	Methane and water
Pipe wall	No-slip conditions
g	9.8 m/s <sup>2</sup>

## 2.4 RESULTS AND DISCUSSIONS

In this chapter, the hydrate formation in a jumper geometry with two phases of methane as the dispersed phase and water + hydrate as the continuous phase is simulated. Simulation runs are conducted based on the modeling methodology described in section 2.2. In the first step, the transient two-phase Eulerian CFD model is applied to investigate hydrate formation at a gas velocity of 5 m/s and a gas volume fraction of 0.2. Then the mass fraction of hydrate in the outlet is calculated in various ranges of fluid velocity (5 to 20 m/s), gas volume fraction (0.2 to 0.5), and fluid inlet temperature (7 to 25°C ). In addition, the influence of these parameters on the hydrate formation behavior in the jumper is discussed.

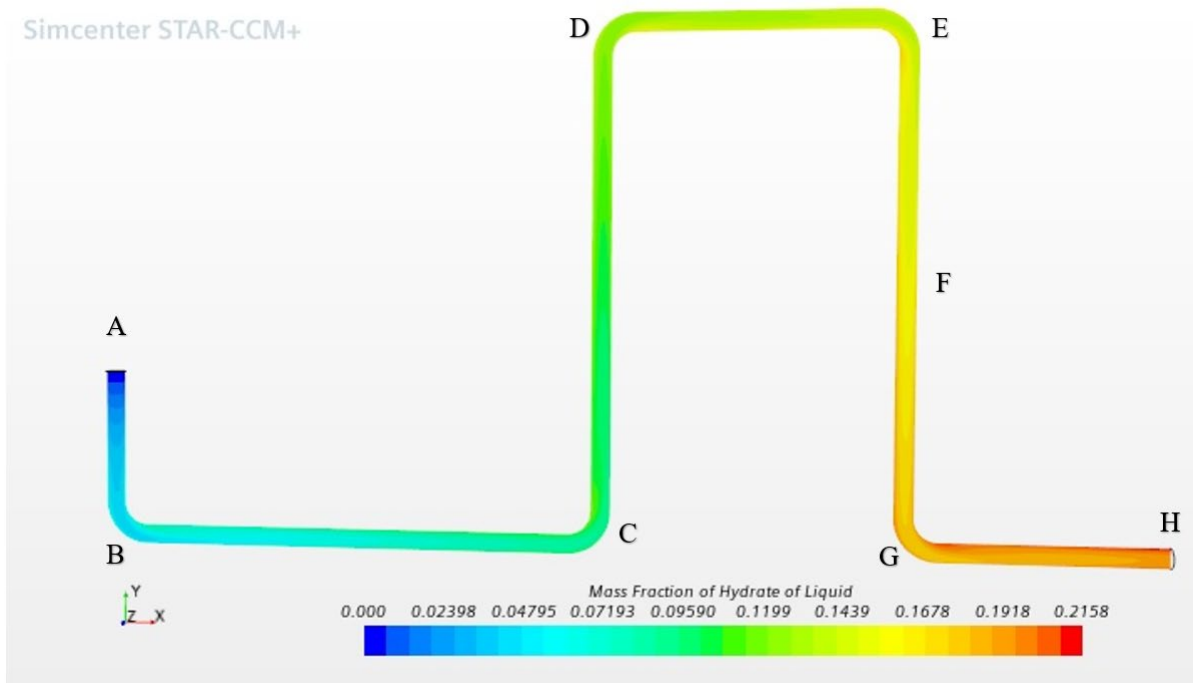


**Figure 2-3.** Contour plots of mass fraction of hydrate in the jumper [Fluid velocity =5 m/s; gas volume fraction (VF) = 0.2; and fluid inlet temperature = 7°C].

Figure 2-3 depicts the mass fraction of hydrate in the liquid phase in different jumper sections for a case where the inlet gas velocity is 5 m/s, the gas volume fraction is 0.2, and the fluid inlet temperature is 7 °C. Other parameters are given in Table 2-2. According to Figure 2-3, the hydrate mass fraction is zero at point A (the inlet point) and is gradually increased along the bends and straight pipes, reaching approximately 0.2158 at the outlet section of H. However, a higher concentration area is located near the wall where the temperature is lower (wall temperature is 4 °C). The hydrate mass fraction distribution contours for cross-section areas of points B, C, E, and H at a time of 10 seconds, based on Figure 2-3, are demonstrated in Figure 2-4. It can be seen from Figure 2-4 that the concentration of hydrate particles in the middle region is less than in the near-wall region. In fact, the mass fraction of hydrate is gradually increased from the middle area forward to the wall. The pipe wall condition can explain this behavior with lower temperatures (4 °C). This phenomenon confirms that hydrate forms in low-temperature and high-pressure conditions. On the other hand, the gas consumption rate is proportional to subcooling so that the hydrate formation near the pipe wall region is significantly more than that of the pipe middle due to an increase in subcooling [65]. A comparison of two cross-sections of two points, B and C, reveals that the mass fractions of hydrate in the middle region are 0.0403 and 0.09812, respectively, while the magnitudes of this parameter for points E and H are 0.1155 and 0.1904.

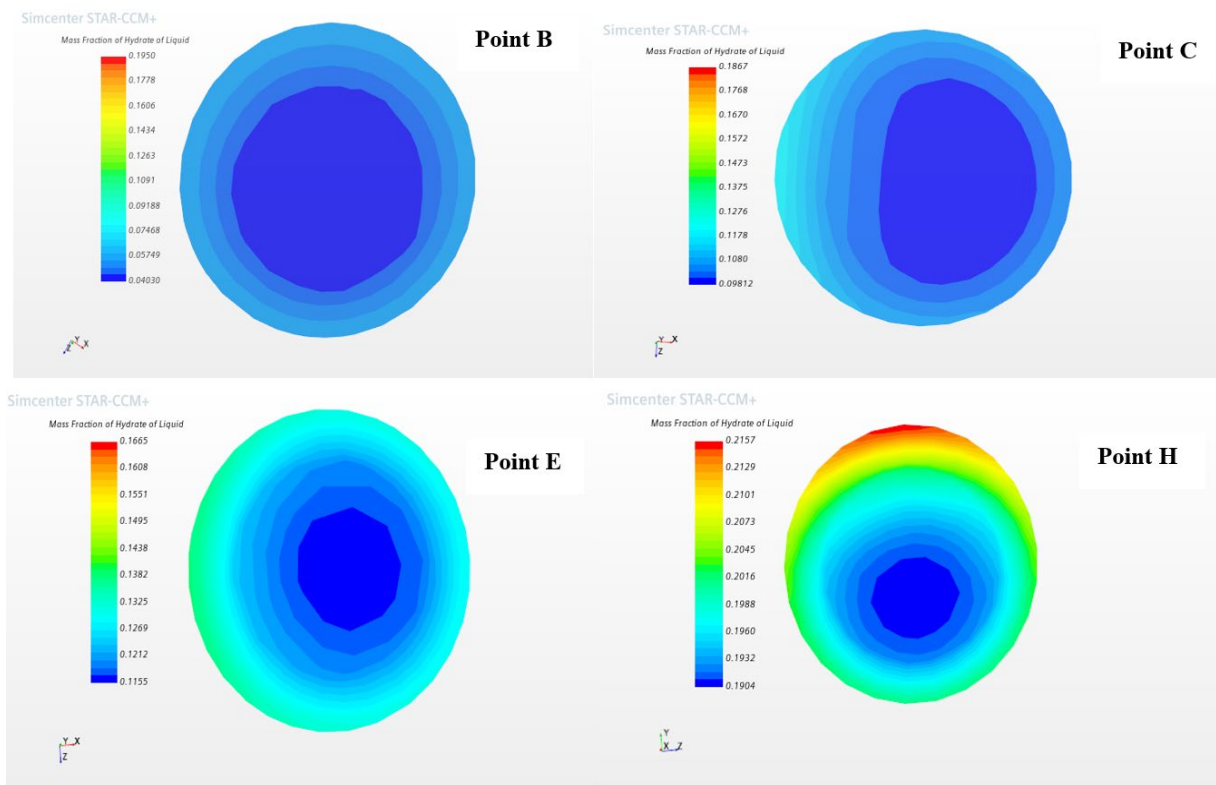


**Figure 2-4.** Hydrate mass fraction contours for points of B, C, E, and H [fluid velocity =5 m/s; gas volume fraction (VF) = 0.2; and fluid inlet temperature = 7 °C].

The magnitude of liquid velocity in various positions is illustrated in Figure 2-5. It can be observed that the liquid velocity is achieved its maximum value around the center of pipes and bend areas, while it decreases when the liquid reaches near the wall and it becomes zero at non-slip walls. Liquid velocity is 6.433 m/s in the bend areas. The reason is that in the bend areas, there is a significant pressure drop due to hydrate formation and geometry type, resulting in an increase in the velocity value.

Sensitivity analysis of flow parameters involved in hydrate formation occurrence can improve the knowledge of the hydrate phenomenon in the jumper geometry and give a deeper insight into this phenomenon.

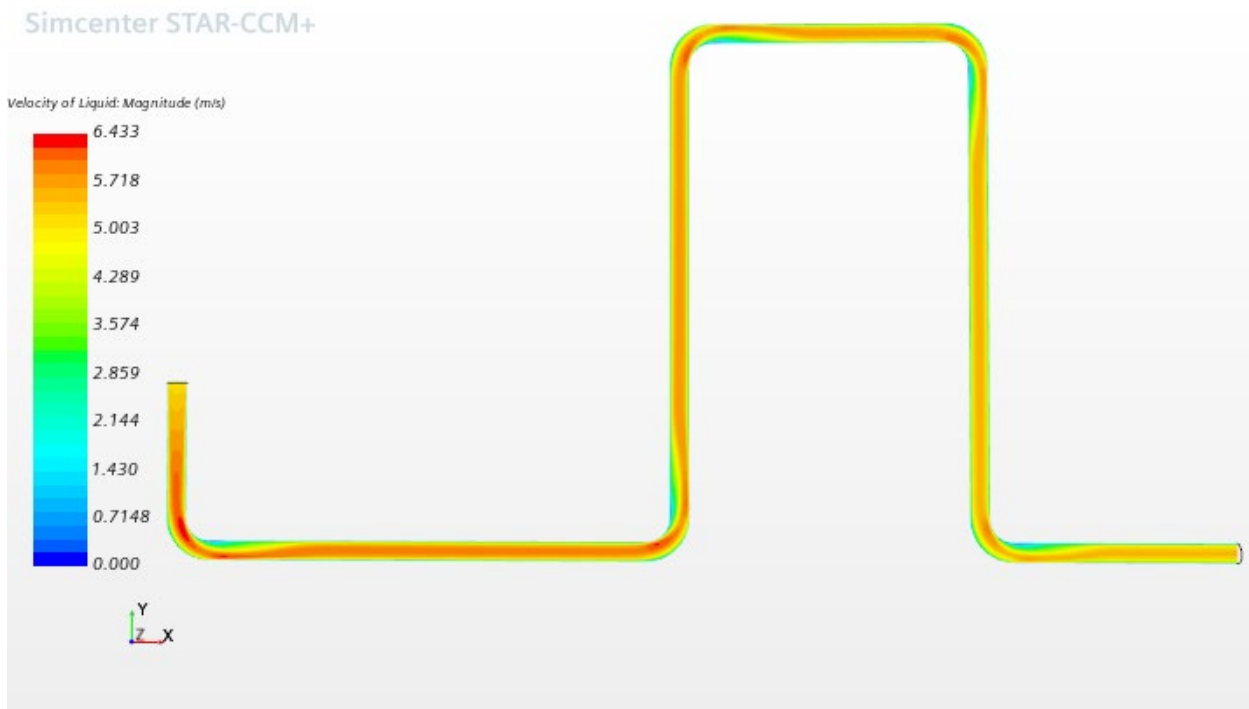


**Figure 2-5.** Contour plots of liquid velocity in the jumper [inlet velocity =5 m/s; gas volume fraction (VF) = 0.2; and fluid inlet temperature =7°C].

#### 2.4.1 Effect of Inlet Liquid Velocity on Hydrate Formation

The hydrate mass fraction is determined in different cases with the liquid inlet velocities of 5, 10, 15, and 20 m/s, where the values of the gas volume fraction and fluid inlet temperature are 0.2 and 16 °C, respectively. For a systematic analysis, section F-G-H of the jumper, according to Figure 2-1 is selected. Figure 2-6 displays the contour plots of methane hydrate mass fraction at different liquid velocities for the F-G-H section. It can be seen that as the liquid inlet velocity increases, the hydrate formation decreases gradually, where the mass fraction of hydrate for the case with a velocity of 5 m/s is maximized in the outlet section (H), equal to 0.159. However, this parameter is 0.062 for case 4 with a velocity of 20 m/s. This is because, at a higher velocity, the transportability of the system increases. In this condition, the residence time of the methane molecules inside the jumper may not be sufficient; this means that the reactants do not spend enough time reacting in the jumper, and the amount of hydrate formation lowers. Therefore, the hydrate formation decreases with an increase in liquid velocity. The common point among the various cases

in Figure 2-6 is that the hydrate concentration near the cold wall regions is more than that of the pipe center area. The hydrate mass fraction in the outlets for cases 2 and 3 with the velocity of 10 and 15 m/s is 0.099 and 0.076. The hydrate volume for different liquid velocities versus time step until 10 seconds is presented in Figure 2-7. It is concluded that the higher the flow velocity, the lower hydrate formation on different jumper parts; also, all curves reach a steady-state condition after 10 seconds.

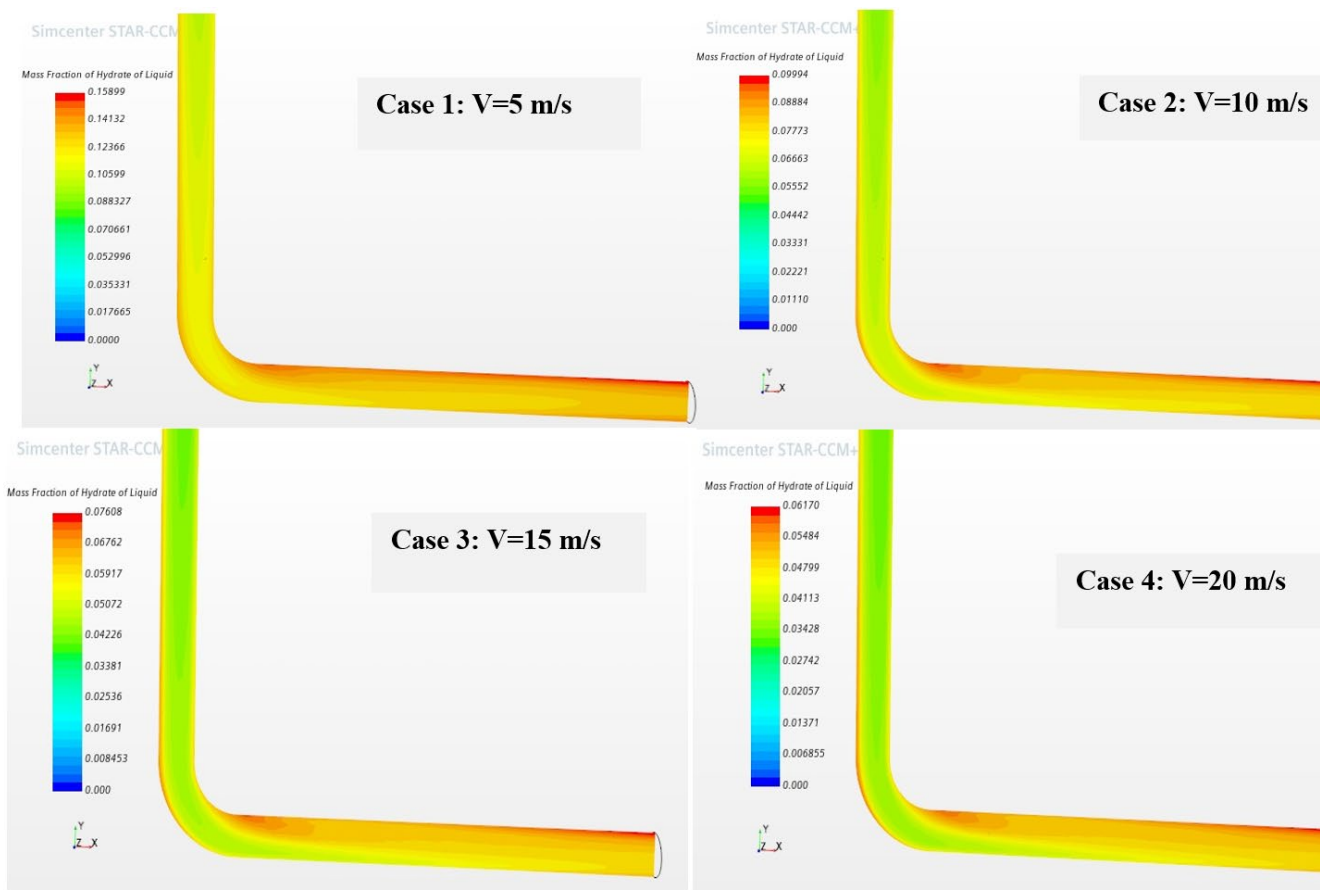


**Figure 2-6.** Contour plots of hydrate mass fraction at various liquid velocities in the jumper [gas volume fraction (VF) =0.2; and fluid inlet temperature =16°C].

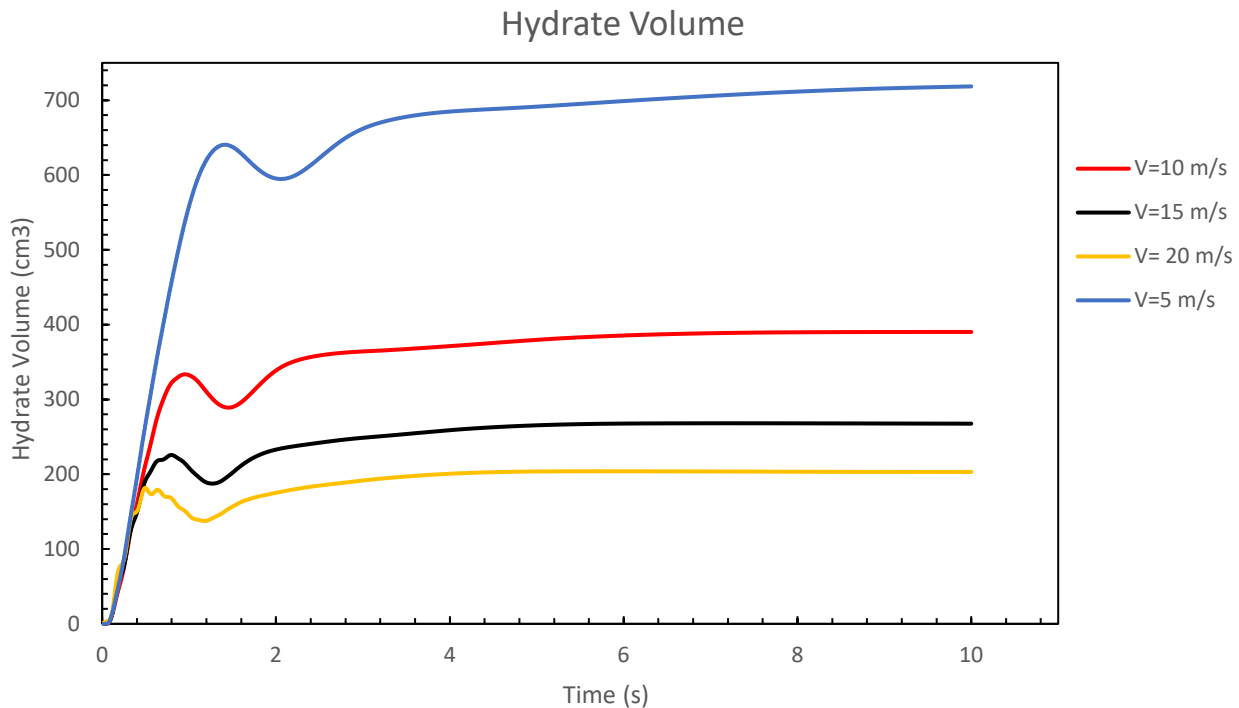


**Figure 2-7.** Effect of liquid velocity on the mass fraction of hydrate in different time steps [gas volume fraction (VF) = 0.2; and fluid inlet temperature = 16 °C].

Figure 2-8 presents the contours of the liquid velocity distribution in the outlet cross-section of the jumper. It can be found from Figure 2-8 that the liquid velocity at non-slip walls is zero under simulated conditions, while this parameter at the middle region of the outlet cross-section of the jumper reaches its maximum value. In two cases 1 and 2, the velocity distribution is symmetrical; however, it is asymmetrical around a horizontal plane through the jumper axis for cases 3 and 4. The values of velocity at the middle area of the outlet cross-section for cases 1, 2, 3, and 4 are 5.783, 11.60, 17.27, and 22.59 m/s, respectively.

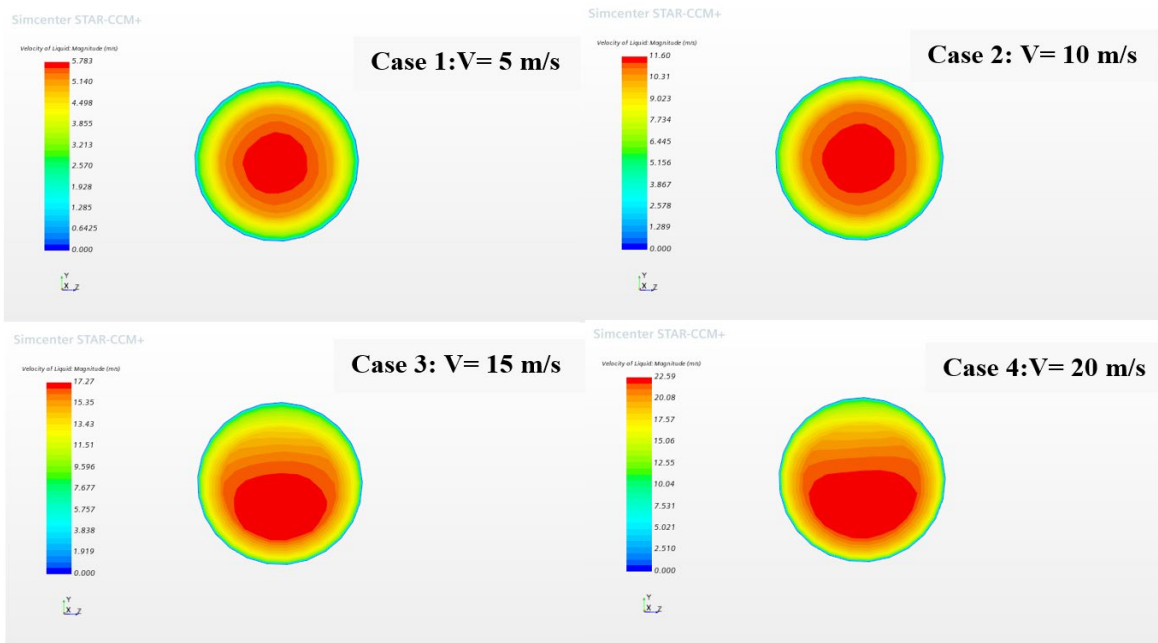


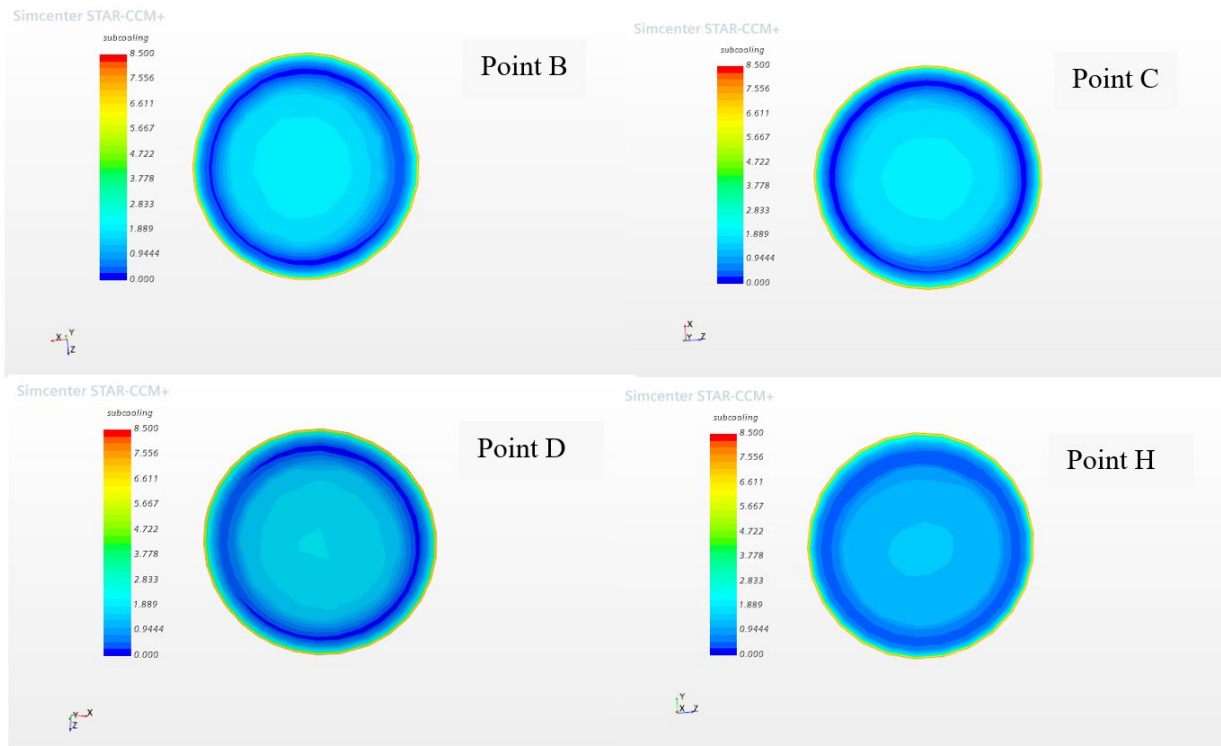
**Figure 2-8.** Cross-sectional contour plots of the liquid velocity in the jumper outlet for various inlet fluid velocities [gas volume fraction (VF)=0.2; fluid inlet temperature = 7 °C].

#### 2.4.2 Effect of Fluid Inlet Temperature and Subcooling on Hydrate Formation

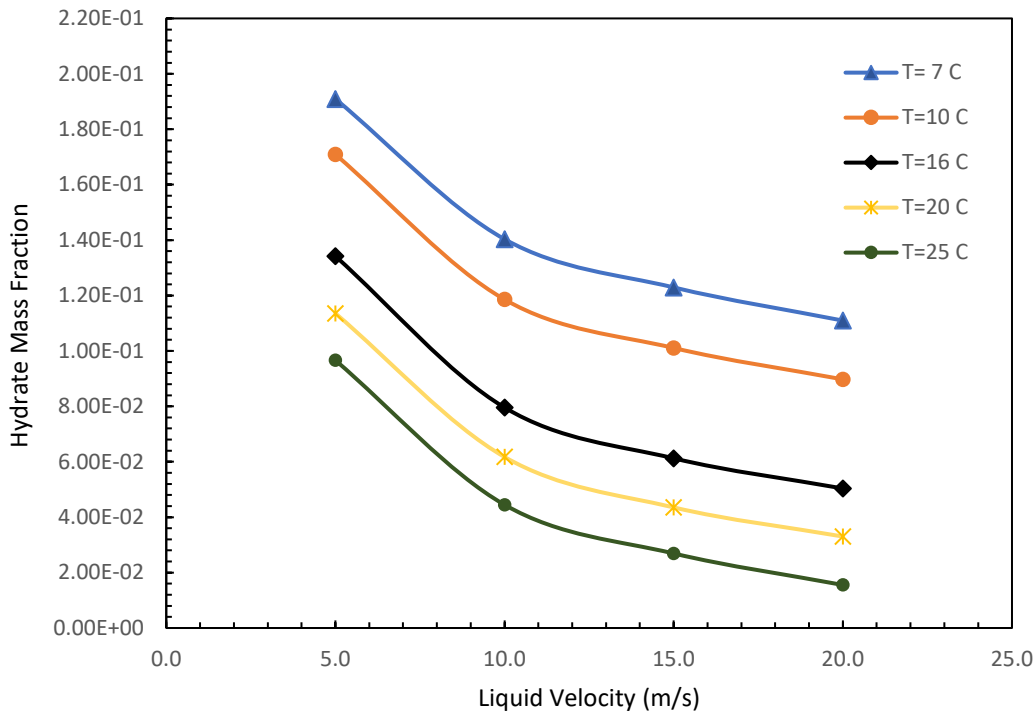
The driving force for hydrate formation is subcooling, the difference between hydrate equilibrium temperature and actual system temperature at the system pressure [66]. Methane gas consumption rate is a function of subcooling, where subcooling (as a function of fluid temperature) is a key parameter in hydrate formation in the jumper. Figure 2-9 illustrates the cross-sectional contour plots of subcooling for regions of B, C, D, and H according to Figure 2-1. It can be observed that subcooling near the wall for these stations (B, C, D, and H) is at the highest level (around 8°C), while in the middle region, it is about 1 °C. As mentioned earlier, the hydrate formation is proportional to subcooling; thus, the hydrate formation near the wall is more than that of the pipe center. This is because the wall temperature is 4°C, and the liquid velocity is relatively small (close to zero) which leads to an increase in the hydrate formation rate.

Figure 2-10 depicts the hydrate mass fraction for various liquid velocities and inlet gas temperatures when the volume fraction of gas is 0.2. It can be concluded that a decrease in the fluid inlet temperature causes a significant increase in the value of hydrate formation at different velocities. In the case with 10 °C as fluid

inlet temperature and the liquid velocity of 5 m/s, the hydrate mass fraction is maximized in the H region (jumper outlet) with the value of 0.1709, while it is 0.0897 for the 20 m/s case, which is minimum. This parameter also for cases with 10 m/s and 15 m/s in the jumper outlet is 0.1186 and 0.1011, respectively. According to Figure 2-10, when the fluid inlet temperature increases from 7 °C to 25 °C, the magnitude of hydrate mass fraction decreases from 0.1229 to 0.0269 for the fluid with a constant velocity of 15 m/s and a gas volume fraction of 0.2. In this case, the hydrate mass fraction at the temperature of 16 °C is 0.0612, while it is equal to 0.0269 when the inlet temperature is 25 °C.



**Figure 2-9.** Cross-sectional contour plots of subcooling at jumper stations [gas volume fraction (VF) = 0.2; fluid inlet temperature = 10 °C; and liquid velocity = 5 m/s].



**Figure 2-10.** Effect of liquid velocity and fluid inlet temperature on the hydrate mass fraction in the jumper.

### 2.4.3 Effect of Gas Volume Fraction on Hydrate Formation

The gas/water volume fraction (water cut) of the fluid is also a critical factor in hydrate formation in the jumper. Sensitivity analysis of flow specifications, including inlet fluid temperature and gas volume fraction, can assist in having a more profound vision of hydrate formation phenomena in complicated jumper geometries, as shown in Figure 2-11. In the simulation trials, the liquid velocity is constant (e.g., 5 m/s). It can be observed that the mass fraction of hydrate in the jumper increases with increasing gas volume fraction, while it decreases with increasing temperature. According to Figure 2-11, the slope of changes for hydrate formation in two temperatures of 7 °C and 10 °C is significantly higher than that of two other temperatures (15 and 20 °C). The maximum hydrate mass fraction is 0.4158 for the fluid with the inlet temperature of 7 °C and gas volume fraction of 0.5. It is important to note that although the volume of water decreases when the gas volume increases, methane is a limiting reactant due to low solubility in the hydrate reaction. Hence, increasing gas volume fraction helps increase the hydrate reaction rate, and as a result, the

amount of formed hydrate increases in this case. When the fluid has a temperature of 25 °C, and the gas volume fraction is 0.2, the amount of hydrate is minimum with the value of 0.0966. It is found, that at a constant gas volume fraction, as the temperature of the fluid increases, the hydrate mass fraction decreases significantly.

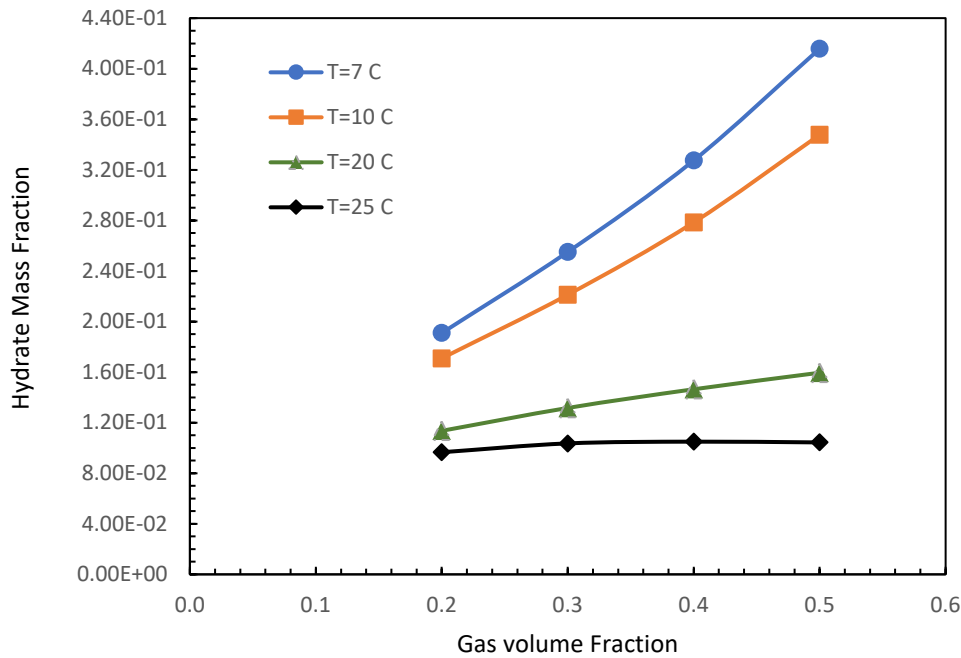


**Figure 2-11.** Effect of gas volume fraction and fluid inlet temperature on the hydrate mass fraction in the jumper.

## 2.5 CONCLUSIONS

In this chapter, hydrate formation for two phases of water and methane is simulated using Star CCM+ (CFD software), in which the multiphase Eulerian model is chosen to investigate the hydrate formation in the jumper. Transport equations, including conservation of mass, momentum, and energy, are solved simultaneously where the mass transfer, hydrate kinetics, and heat of hydrate formation are incorporated in the mass and energy equations, respectively. Pre-processing steps, including geometry selection, meshing, and mesh independency analysis, are conducted before the solving and post-processing steps. Then, hydrate formation is simulated in a jumper for the fluid velocity of 5 m/s with the inlet temperature of 7 °C and gas volume fraction of 0.2. Sensitivity analysis to explore the impacts of the inlet fluid velocity, water volume

fraction, inlet temperature, and subcooling on the hydrate formation is then performed. The main conclusions drawn from this research work are given below:

1. Comparing the results of various transient simulation runs using two-phase Eulerian model shows that a time step of 0.01 s with the total simulation time of 10 s seems proper to reach the steady-state conditions.
2. The hydrate formation is successfully simulated in the jumper at the gas velocity of 5 m/s and the gas volume fraction of 0.2. The amount of hydrate formation is zero at the inlet, then gradually reaches a maximum extent (e.g., 0.2158). The hydrate mass fraction in the middle region of pipes is less than the near-wall region due to the cold wall temperature (4 °C) and higher subcooling. Moreover, the liquid velocity value is almost zero near the non-slip wall, while it attains its maximum value (6.44 m/s) in the center and bend areas of the jumper.
3. According to the contour plots, the lower inlet fluid velocities are favorable for higher hydrate mass fractions in the jumper. The reason for this finding is that at a higher value of inlet fluid velocity, the methane molecules do not have sufficient time to be dissolved in the water due to increased fluid transportability. Hence, the highest hydrate mass fraction might be obtained when the velocity is 5 m/s.
4. The gas consumption rate is directly proportional to subcooling in the jumper. The subcooling value near the non-slip wall is higher than that of the pipe center due to the wall temperature. When the fluid inlet temperature decreases, a significant increase in the amount of formed hydrate is observed. Moreover, increasing the fluid inlet temperature at a constant velocity leads to a reduction in hydrate mass fraction.
5. The high gas volume fraction and low fluid inlet temperature are favorable for more hydrate formation, particularly near the walls. Based on the hydrate reaction equation, methane is a limiting reactant due to low solubility; therefore, increasing gas volume fraction leads to dissolving more methane gas in the water as a reactant. As a result, the gas volume fraction and inlet temperature might play a significant

role in the methane hydrate formation in the jumper. Furthermore, at a constant gas volume fraction, the higher the fluid inlet temperature, the lower the hydrate forms.

This CFD simulation will help to further understand hydrate formation phenomena in the jumper. This tool also may assist the oil and gas industry in designing subsea pipes with greater efficiency in terms of hydrate formation control in petroleum facilities. Further experimental and modeling studies are required to validate the introduced model as the next step of this research. In addition, adding the oil phase to the fluid can lead to an interesting hydrate system for future work in terms of theoretical and practical aspects.

## ACKNOWLEDGMENTS

The authors would like to acknowledge Memorial University (NL, Canada), the Natural Sciences and Engineering Research Council of Canada (NSERC), Equinor Canada, and InnovateNL for offering financial assistance.

## NOMENCLATURES

Acronyms	
ANSYS	Analysis Systems
CFD	Computational Fluid Dynamic
MEG	Mono Ethylene Glycol
PBM	Population Balance Model
WD	Water Depth
Variables/Letters	
$A_s$	Surface area ( $m^2$ )
$a_j, a_k$	Acceleration of phase $j$ and $k$ ( $m\ s^{-2}$ )
$a_{kj}$	Interfacial area density ( $m^{-1}$ )
$C_D$	Drag coefficient
$C_{p_{hyd}}$	Heat capacity of hydrate ( $J\ Kg^{-1}\ K^{-1}$ )
$C_{VM}$	Virtual mass coefficient for interaction $kj$
$f_{hyd}$	Mass fraction of hydrate in the water
$f_w$	Mass fraction of the water
$F_{kj}^D$	Drag force per unit of volume ( $N\ m^{-3}$ )
$F_{kj}^{VM}$	Virtual mass flow per unit of volume ( $N\ m^{-3}$ )
$F_{kj}^{TD}$	Turbulent dispersion force per unit of volume ( $N\ m^{-3}$ )
$g$	Gravity ( $m\ s^{-1}$ )
$h$	Phase enthalpy ( $J\ Kg^{-1}$ )
$k_1$	Intrinsic kinetics rate constants 1 ( $Kg\ m^{-2}\ s^{-1}\ K^{-1}$ )
$k_2$	Intrinsic kinetics rate constants 2 (K)
$l$	Interaction length scale or bubble size (m)

$n$	Stoichiometric coefficients
$\dot{m}$	Mass transfer rate ( $\text{Kg s}^{-1}$ )
$M_K$	Sum of interfacial forces and momentum associated with mass transfer ( $\text{N m}^{-3}$ )
$p$	System pressure (Pa)
$Q$	Heat source term ( $\text{W m}^{-3}$ )
$\dot{q}_{hyd}$	Heat of Hydrate Formation (J/s)
$Re_d$	Dispersed Reynolds number
$T_{system}$	Actual system temperature (K)
$T_{hyd}$	Hydrate equilibrium temperature at the system pressure (K)
$\bar{u}_k$	Velocity of the k-th phase ( $\text{m s}^{-1}$ )
$u$	Correction Coefficient (1/500)
$W_j$	Weight function
$W_{hyd}$	Molar mass of methane hydrate
$W_{CH_4}$	Molar mass of methane gas

---

### Greek Letters

---

$\alpha_k$	Volume fraction of phase i
$\rho_k$	Density of phase k ( $\text{Kg m}^{-3}$ )
$\lambda$	Thermal conductivity ( $\text{W m}^{-1} \text{K}$ )
$\mu_k$	Dynamic viscosity of the continuous phase ( $\text{Kg m}^{-1} \text{s}^{-1}$ )
$\mu_t$	Turbulent viscosity (Pa s)
$\sigma_t$	Turbulent Prantle number with 0.9 value
$\Delta T_{sub}$	Subcooling (K)

---

### Subscripts and Superscripts

---

$k, j$	Phases
$hyd$	Hydrate
$g$	Gas
$sub$	Subcooling
$d$	Dispersed phase in the phase interaction
$t$	Turbulent
$W$	Water

---

## REFERENCES

1. Gbaruko, B., J. Igwe, P. Gbaruko, and R. Nwokeoma, *Gas hydrates and clathrates: Flow assurance, environmental and economic perspectives and the Nigerian liquified natural gas project*. Journal of Petroleum Science and Engineering, 2007. **56**(1-3): p. 192-198.
2. Zerpa, L.E., J.-L. Salager, C.A. Koh, E.D. Sloan, and A.K. Sum, *Surface chemistry and gas hydrates in flow assurance*. Industrial & Engineering Chemistry Research, 2011. **50**(1): p. 188-197.
3. Teixeira, A.M., L. de Oliveira Arinelli, J.L. de Medeiros, and F.A. Ofélia de Queiroz, *Recovery of thermodynamic hydrate inhibitors methanol, ethanol and MEG with supersonic separators in offshore natural gas processing*. Journal of Natural Gas Science and Engineering, 2018. **52**: p. 166-186.
4. Chatti, I., A. Delahaye, L. Fournaison, and J.-P. Petitet, *Benefits and drawbacks of clathrate hydrates: a review of their areas of interest*. Energy conversion and management, 2005. **46**(9-10): p. 1333-1343.
5. Cox, J., *Natural Gas Hydrates: Props., Occurrence and Recovery*. 1983, Buytherworth Publishers, Woburn, MA.
6. Zhang, X., B.R. Lee, J.-H. Sa, K.M. Askvik, X. Li, T. Austvik, and A.K. Sum, *Hydrate management in deadlegs: effect of pipe size on hydrate deposition*. Energy & Fuels, 2019. **34**(2): p. 1422-1431.
7. Mokhatab, S., R.J. Wilkens, and K. Leontaritis, *A review of strategies for solving gas-hydrate problems in subsea pipelines*. Energy Sources, Part A, 2007. **29**(1): p. 39-45.
8. Creek, J., S. Subramanian, D. Estanga, and K. Kreibjerg. *Project design hydrate management by application of multiphase flow simulations tools with hydrate formation and transport*. in *Proc. 7th International Conference on Gas Hydrates*. 2011.
9. Kurup, A.S., O. Hernandez, T. Idstein, C.A. Zamora, L. Greenly, and J. Anderson. *Pushing conventional boundaries of hydrate management in a dry tree facility*. in *Offshore Technology Conference*. 2017. Offshore Technology Conference.

10. Kinnari, K., J. Hundseid, X. Li, and K.M. Askvik, *Hydrate management in practice*. Journal of Chemical & Engineering Data, 2015. **60**(2): p. 437-446.
11. Sloan, E.D., *A changing hydrate paradigm—from apprehension to avoidance to risk management*. Fluid Phase Equilibria, 2005. **228**: p. 67-74.
12. Creek, J., *Efficient hydrate plug prevention*. Energy & Fuels, 2012. **26**(7): p. 4112-4116.
13. Sloan, E.D., *Natural gas hydrates in flow assurance*. 2010: Gulf Professional Publishing.
14. Leon Caceres, S., *Safety Problems Caused by Hydrate Formation in Deepwater Production Operation*. 2017.
15. Reyna, E. and S. Stewart. *Case history of the removal of a hydrate plug formed during deep water well testing*. in *SPE/IADC drilling conference*. 2001. OnePetro.
16. Camargo, R., M. Gonçalves, J. Montesanti, C. Cardoso, and K. Minami. *A perspective view of flow assurance in deepwater fields in Brazil*. in *Offshore Technology Conference*. 2004. OnePetro.
17. Zare, M., A. Haghtalab, A.N. Ahmadi, K. Nazari, and A. Mehdizadeh, *Effect of imidazolium based ionic liquids and ethylene glycol monoethyl ether solutions on the kinetic of methane hydrate formation*. Journal of Molecular Liquids, 2015. **204**: p. 236-242.
18. Zare, M., A. Haghtalab, A.N. Ahmadi, and K. Nazari, *Experiment and thermodynamic modeling of methane hydrate equilibria in the presence of aqueous imidazolium-based ionic liquid solutions using electrolyte cubic square well equation of state*. Fluid Phase Equilibria, 2013. **341**: p. 61-69.
19. Torr e, J.-P., M. Ricaurte, C. Dicharry, and D. Broseta, *CO<sub>2</sub> enclathration in the presence of water-soluble hydrate promoters: hydrate phase equilibria and kinetic studies in quiescent conditions*. Chemical engineering science, 2012. **82**: p. 1-13.
20. Nazeri, M., B. Tohidi, and A. Chapoy, *An evaluation of risk of hydrate formation at the top of a pipeline*. Oil and Gas Facilities, 2014. **3**(02): p. 67-72.

21. Lv, Q.-N., X.-S. Li, C.-G. Xu, and Z.-Y. Chen, *Experimental investigation of the formation of cyclopentane-methane hydrate in a novel and large-size bubble column reactor*. *Industrial & engineering chemistry research*, 2012. **51**(17): p. 5967-5975.
22. Li, A., L. Jiang, and S. Tang, *An experimental study on carbon dioxide hydrate formation using a gas-inducing agitated reactor*. *Energy*, 2017. **134**: p. 629-637.
23. Akhfash, M., M. Arjmandi, Z.M. Aman, J.A. Boxall, and E.F. May, *Gas hydrate thermodynamic inhibition with MDEA for reduced MEG circulation*. *Journal of Chemical & Engineering Data*, 2017. **62**(9): p. 2578-2583.
24. Mohebbi, V. and R. Behbahani, *Experimental study on gas hydrate formation from natural gas mixture*. *Journal of Natural Gas Science and Engineering*, 2014. **18**: p. 47-52.
25. Abdi-Khanghah, M., M. Adelizadeh, Z. Naserzadeh, and H. Barati, *Methane hydrate formation in the presence of ZnO nanoparticle and SDS: application to transportation and storage*. *Journal of Natural Gas Science and Engineering*, 2018. **54**: p. 120-130.
26. Liu, Z., M. Yang, H. Zhang, B. Xiao, L. Yang, and J. Zhao, *A high-pressure visual flow loop for hydrate blockage detection and observation*. *Review of Scientific Instruments*, 2019. **90**(7): p. 074102.
27. Fu, W., Z. Wang, X. Yue, J. Zhang, and B. Sun, *Experimental study of methane hydrate formation in water-continuous flow loop*. *Energy & Fuels*, 2019. **33**(3): p. 2176-2185.
28. Shi, B.-H., S.-F. Song, X.-F. Lv, W.-Q. Li, Y. Wang, L. Ding, Y. Liu, J.-H. Yang, H.-H. Wu, and W. Wang, *Investigation on natural gas hydrate dissociation from a slurry to a water-in-oil emulsion in a high-pressure flow loop*. *Fuel*, 2018. **233**: p. 743-758.
29. Aman, Z.M., M. Di Lorenzo, K. Kozielski, C.A. Koh, P. Warriar, M.L. Johns, and E.F. May, *Hydrate formation and deposition in a gas-dominant flowloop: initial studies of the effect of velocity and subcooling*. *Journal of Natural Gas Science and Engineering*, 2016. **35**: p. 1490-1498.

30. Pickarts, M.A., D. Croce, L.E. Zerpa, and C.A. Koh. *Gas Hydrate Formation & Transportability during Transient Shut-In/Restart Conditions*. in *Offshore Technology Conference*. 2020. Offshore Technology Conference.
31. Kumar, A., M. Di Lorenzo, K. Kozielski, P. Glénat, E. May, and Z. Aman. *Hydrate Blockage Assessment in a Pilot-Scale Subsea Jumper*. in *Offshore Technology Conference*. 2020.
32. Kumar, A., M. Di Lorenzo, K. Kozielski, P. Glénat, E.F. May, and Z.M. Aman, *Hydrate Blockage Assessment in a Pilot-Scale Subsea Jumper*. Offshore Technology Conference, 2020.
33. Haghtalab, A., M. Zare, A. Ahmadi, and K. Nazari, *Prediction of hydrate equilibrium conditions using electrolyte cubic square-well equation of state*. Fluid phase equilibria, 2012. **333**: p. 74-86.
34. Zare, M., J. Kondori, S. Zendehboudi, and F. Khan, *PC-SAFT/UNIQUAC model assesses formation condition of methane hydrate in the presence of imidazolium-based ionic liquid systems*. Fuel, 2020. **266**: p. 116757.
35. Kondori, J., S. Zendehboudi, and L. James, *Evaluation of gas hydrate formation temperature for gas/water/salt/alcohol systems: utilization of extended UNIQUAC model and PC-SAFT equation of state*. Industrial & Engineering Chemistry Research, 2018. **57**(41): p. 13833-13855.
36. Creek, J.L., S. Subramanian, and D.A. Estanga. *New method for managing hydrates in deepwater tiebacks*. in *Offshore Technology Conference*. 2011. Offshore Technology Conference.
37. Jassim, E.I., M.A. Abdi, and Y. Muzychka. *A CFD-based model to locate flow-restriction induced hydrate deposition in pipelines*. in *Offshore technology conference*. 2008. OnePetro.
38. Song, G., Y. Li, W. Wang, K. Jiang, Z. Shi, and S. Yao, *Hydrate agglomeration modeling and pipeline hydrate slurry flow behavior simulation*. Chinese journal of chemical engineering, 2019. **27**(1): p. 32-43.
39. Balakin, B.V., S. Lo, P. Kosinski, and A.C. Hoffmann, *Modelling agglomeration and deposition of gas hydrates in industrial pipelines with combined CFD-PBM technique*. Chemical Engineering Science, 2016. **153**: p. 45-57.

40. Bendiksen, K.H., D. Maines, R. Moe, and S. Nuland, *The dynamic two-fluid model OLGA: Theory and application*. SPE production engineering, 1991. **6**(02): p. 171-180.
41. Makwashi, N., D. Zhao, T. Ismaila, and I. Paiko. *Pipeline Gas Hydrate Formation and Treatment: A Review*. in *3rd National Engineering Conference on Building the Gap between Academia and Industry, Faculty of Engineering, Bayero University, Kano*. 2018.
42. Turner, D., J. Boxall, S. Yang, D. Kleehammer, C. Koh, K. Miller, E. Sloan, Z. Xu, P. Matthews, and L. Talley. *Development of a hydrate kinetic model and its incorporation into the OLGA2000® transient multiphase flow simulator*. in *5th international conference on gas hydrates, Trondheim, Norway*. 2005.
43. Davies, S.R., J.A. Boxall, L.E. Dieker, A.K. Sum, C.A. Koh, E.D. Sloan, J.L. Creek, and Z.-G. Xu, *Predicting hydrate plug formation in oil-dominated flowlines*. Journal of petroleum science and engineering, 2010. **72**(3-4): p. 302-309.
44. Zerpa, L.E., E.D. Sloan, A.K. Sum, and C.A. Koh, *Overview of CSMHyK: A transient hydrate formation model*. Journal of Petroleum Science and Engineering, 2012. **98**: p. 122-129.
45. Marsh, K.N., J.A. Boxall, and R. Lichtenthaler, *Room temperature ionic liquids and their mixtures—a review*. Fluid phase equilibria, 2004. **219**(1): p. 93-98.
46. Davies, S.R., J.A. Boxall, C. Koh, E.D. Sloan, P.V. Hemmingsen, K.J. Kinnari, and Z.-G. Xu, *Predicting hydrate-plug formation in a subsea tieback*. SPE Production & Operations, 2009. **24**(04): p. 573-578.
47. Wang, Y., C.A. Koh, J.A. Dapena, and L.E. Zerpa, *A transient simulation model to predict hydrate formation rate in both oil-and water-dominated systems in pipelines*. Journal of Natural Gas Science and Engineering, 2018. **58**: p. 126-134.
48. Sule, I., A. Adedeji, C. Obeng, A. Okosun, M. Morshed, M. Rahman, and K. Hawboldt, *CFD analysis of hydrate formation in pipelines*. Petroleum Science and Technology, 2015. **33**(5): p. 571-578.

49. Jujuly, M., M.A. Rahman, A. Maynard, and M. Adey, *Hydrate-induced vibration in an offshore pipeline*. SPE Journal, 2020. **25**(02): p. 732-743.
50. Yao, S., Y. Li, W. Wang, G. Song, Z. Shi, X. Wang, and S. Liu, *Investigation of hydrate slurry flow behaviors in deep-sea pipes with different inclination angles*. Oil & Gas Science and Technology–Revue d'IFP Energies nouvelles, 2019. **74**: p. 48.
51. Lo, S. *CFD modelling of hydrate formation in oil-dominated flows*. in *Offshore Technology Conference*. 2011. OnePetro.
52. Balakin, B., A. Hoffmann, and P. Kosinski, *Experimental study and computational fluid dynamics modeling of deposition of hydrate particles in a pipeline with turbulent water flow*. Chemical Engineering Science, 2011. **66**(4): p. 755-765.
53. Balakin, B., A. Hoffmann, P. Kosinski, and S. Høiland, *Turbulent flow of hydrates in a pipeline of complex configuration*. Chemical engineering science, 2010. **65**(17): p. 5007-5017.
54. Talimi, V., P. Thodi, M.A. Abdi, R. Burton, L. Liu, and J. Bruce, *Enhancing harsh environment oil spill recovery using air floatation system*. Safety in Extreme Environments, 2019. **1**(1): p. 27-37.
55. Balakin, B.V., A. Kosinska, and K.V. Kutsenko, *Pressure drop in hydrate slurries: Rheology, granulometry and high water cut*. Chemical Engineering Science, 2018. **190**: p. 77-85.
56. CD-adapco, S., *STAR-CCM+ Documentation-Version 13.06*. 2016.
57. Neto, E. *A mechanistic computational fluid dynamic CFD model to predict hydrate formation in offshore pipelines*. in *SPE Annual Technical Conference and Exhibition*. 2016. OnePetro.
58. Crowe, C.T., J.D. Schwarzkopf, M. Sommerfeld, and Y. Tsuji, *Multiphase flows with droplets and particles*. 2011: CRC press.
59. Kim, H., P.R. Bishnoi, R.A. Heidemann, and S.S. Rizvi, *Kinetics of methane hydrate decomposition*. Chemical engineering science, 1987. **42**(7): p. 1645-1653.
60. Englezos, P., N. Kalogerakis, P. Dholabhai, and P. Bishnoi, *Kinetics of formation of methane and ethane gas hydrates*. Chemical Engineering Science, 1987. **42**(11): p. 2647-2658.

61. Boxall, J., S. Davies, C. Koh, and E.D. Sloan, *Predicting when and where hydrate plugs form in oil-dominated flowlines*. SPE Projects, Facilities & Construction, 2009. **4**(03): p. 80-86.
62. Duan, J.-S., R. Rach, and A.-M. Wazwaz, *A reliable algorithm for positive solutions of nonlinear boundary value problems by the multistage Adomian decomposition method*. Open Engineering, 2014. **5**(1).
63. Fatoorehchi, H., M. Alidadi, R. Rach, and A. Shojaeian, *Theoretical and experimental investigation of thermal dynamics of Steinhart–Hart negative temperature coefficient thermistors*. Journal of Heat Transfer, 2019. **141**(7): p. 072003.
64. González-Parra, G., A.J. Arenas, and L. Jódar, *Piecewise finite series solutions of seasonal diseases models using multistage Adomian method*. Communications in Nonlinear Science and Numerical Simulation, 2009. **14**(11): p. 3967-3977.
65. Grasso, G.A., E.D. Sloan, C. Koh, J. Creek, and G. Kusinski. *Hydrate deposition mechanisms on pipe walls*. in *Offshore Technology Conference*. 2014. Offshore Technology Conference.
66. Arjmandi, M., B. Tohidi, A. Danesh, and A.C. Todd, *Is subcooling the right driving force for testing low-dosage hydrate inhibitors?* Chemical engineering science, 2005. **60**(5): p. 1313-1321.

# **3.CHAPTER THREE**

## **Deterministic Tools to Estimate Induction Time for Methane Hydrate Formation in the Presence of Luvicap 55 W Solutions**

### **Preface**

A version of this manuscript has been published in the Journal of Molecular Liquids Volume 348, 15 February 2022, 118374. The first author of this paper, Marziyeh Zare, designed the manuscript with the help of co-authors (Sohrab Zendehboudi and Majid Abedinzadegan Abdi). Marziyeh Zare developed deterministic tools for predicting induction time in this paper. The first author also conducted a literature review, data analysis, modeling, and results analysis. The first draft was prepared by Marziyeh Zare and revised based on the co-authors' feedback. The feedback from journal reviewers was applied to the manuscript by the first author. The co-authors, Sohrab Zendehboudi and Majid Abedinzadegan Abdi had the supervision role and edited the manuscript.

## ABSTRACT

The formation of gas hydrates in offshore pipelines is a severe flow assurance issue. The hydrates may form quickly in pipelines without any warning. Thus, effective remediation approaches may require to be performed for days or months. Injecting chemicals such as kinetic hydrate inhibitors (KHIs) can be implemented to prevent or manage gas hydrate formation in offshore facilities. KHIs with polymeric structures and various functional groups postpone hydrate nucleation and growth with a subcooling of 8 – 10 °C. In this chapter, a new approach is introduced to predict the induction time of methane hydrate formation in the presence of Luvicap 55 W solutions (as a KHI) with a broad range of concentrations. The intelligent models, including least squares, support vector machine (LSSVM), adaptive network-based fuzzy inference system (ANFIS), and gene expression programming (GEP), are employed in this study, where 440 experimental data are collected. In intelligent modeling, 85% of data are utilized for the training step and 15% for the testing step. The smart tools relate the induction time parameter as a target to input parameters such as the molecular weight of solution, mass fraction of KHI, temperature, pressure, and subcooling. The key statistical parameters, including average relative error percent (ARE %), average absolute relative error (AARE %), and coefficient of determination ( $R^2$ ) are calculated to evaluate the performance of the deterministic models. The values of the coefficient of determination ( $R^2$ ) for the developed GEP model are 0.9582 and 0.9726 in the training and testing steps, respectively. The GEP model exhibits the best performance for induction time estimation compared with the LSSVM and ANFIS models, though the run/computational time of this model (e.g., 18 min) is considerably greater than that of other deterministic approaches. Using the ANFIS model, the most influential parameters affecting the induction time are the system pressure and temperature. In addition, other input parameters, including the molecular weight of the solution,

mass fraction of the Luvicap 55 W, and subcooling, exhibit indirect relationship with the induction time.

**Keywords:** Smart tools; Statistical analysis; Gas hydrates; Induction time; Luvicap 55W

### 3.1 INTRODUCTION

Gas hydrates with a crystal structure are formed when water molecules are linked through hydrogen bonding to make host cavities that can enclose various gases as guests. However, no chemical bondings exist between the guest gases and water molecules. Although various gas molecules, including methane, ethane, propane, isobutane, normal butane, nitrogen, carbon dioxide, and hydrogen sulfide can create the gas hydrates, other nonpolar components between the sizes of argon (0.35 nm) and ethyl cyclohexane (0.9 nm) can also form hydrates [1, 2]. Depending on the nature and size of gas molecules, gas hydrates crystalize in three different structures: I (sI), II (sII), and H (sH) [1-4]. Hydrate gas formation in pipelines primarily depends on pressure, temperature, and composition of the gas/water mixture; other parameters including the high velocity of the gas stream, pressure pulsations, and tiny hydrate crystals or other particles may accelerate hydrate formation [4, 5].

In addition to waxes, asphaltenes, and scales formation in the offshore pipelines, gas hydrates are considered as a major flow assurance issue [6-9]. Hydrate plugs are significant threats to oil and gas production and transportation facilities so that they form quickly without any warning relative to waxes, asphaltenes, and scales, while remediation strategies may require days or months to be completed [10]. There are various methods to prevent hydrate formation and keep the system outside of the hydrate formation zone in offshore facilities: 1- insulation of pipelines or applying direct heating; 2- depressurization of the system in shut-down cases; 3- using chemicals (thermodynamic or low dosage hydrate inhibitors); and 4- water removal and dry gas [11, 12]. For

offshore multiphase pipeline systems, hydrate inhibitors are more applicable, since the isolation method is not an economically viable solution. Furthermore, depressurization requires significant storage space for liquids and flaring a massive amount of gas [12]. Hydrate inhibitors are divided into two groups, i.e., thermodynamic inhibitors (THIs) and low-dose hydrate inhibitors (LDHIs). THIs are injected into the pipeline systems with high volume. The value of inhibitor concentration depends on the required subcooling. THIs shift the hydrate equilibrium curve so that they can allow the hydrate to form in lower temperatures and higher pressures [13]. Methanol, monoethyleneglycol (MEG), and salts are examples of THIs [14-17]. LDHIs, which are used in low volumes with a concentration between 0.5 and 3 wt% based on water, do not shift the equilibrium of the hydrate region since they postpone the hydrate nucleation and inhibit hydrate growth [1, 4, 17]. LDHIs are divided into kinetic hydrate inhibitors (KHIs) and anti agglomerants (AAs). KHI structure typically includes polymeric molecules with different functional groups that can delay hydrate nucleation for subcooling of 8 – 10 °C. The role of AAs, which contain quaternary ammonium compounds [18], is to prevent hydrate agglomeration since they allow hydrate crystals to form in the hydrocarbon phase but inhibit hydrate growth in the pipelines. Some parameters, including water cut, the concentration of salt in the produced water, subcooling, and the existence of gas condensate, are the effective criteria to make a selection between KHIs and AAs [17, 19].

For the first time, LDHI was employed by Kuliev, a Russian engineer. It was decided to use commercial surfactants on the top part of the wells' hydrate in 1970 since the hydrate problems in gas wells had been observed. It was found that gas hydrate problems are resolved after utilizing the surfactants [20]. Then, a few institutes, such as IFP (French Petroleum Institute), SINTEF, and Colorado School of Mine (CSM), conducted research investigations on LDHIs to find appropriate

chemicals to prevent gas hydrate formation [20, 21]. PVP (polyvinylpyrrolidone) was used for the first time in CSM when they were performing tests with their ball stop rig device in 1991. This polymer (first-generation inhibitor) delayed THF hydrate formation and agglomeration [22]. The second generation of KHIs, such as Polyvinylcaprolactam (PVCAP), N-vinyl pyrrolidone/N-vinyl caprolactam (VP/VC), and N-vinyl pyrrolidone/N-vinyl caprolactam/N, N-dimethyl aminoethyl methacrylate, which have a similar structure to PVP with lactam-ring polymer groups, was more effective than PVP with a subcooling of 10-12 °C [23-25]. Two key parameters, namely natural gas hydrate induction time and gas consumption rate, were measured for different systems with and without PVP, L-tyrosine, and MEG. The results revealed that the induction time for the system with 2 wt% PVP and 20 wt% MEG aqueous solutions has the highest value, and the rate of the gas consumption for this system is at the lowest level. Therefore, this inhibitor can be a good option for preventing natural gas hydrate formation in pipelines [26]. Long et al. (2019) synthesized a copolymer which is a combination of the random copolymer of N-vinylcaprolactam and 1-vinylimidazole (PVCap-co-VIM), and measured the induction time for methane hydrate formation. The results were then compared with laboratory-made PVCap and commercial poly(N-vinylpyrrolidone) (PVPK90) under various cooling rates (1.0, 2.0, and 5.0 K/h) and mass concentrations (0.5, 1.0, and 2.0 wt %). It was concluded that PVCap-co-VIM is a better inhibitor with a higher value of induction time compared to PVPK90. However, the subcooling rate was the parameter that did not affect the maximum KHI subcooling [27]. The influence of polyethylene oxide on the performance of KHIs (e.g., GHI, Inhibex 501, Luvicap EG, Luvitec K90, Luvitec VPC 55, VC-713, K65 W, Gaffix, and PVP) was studied for the cases of methane and methane/ethane hydrates, where in some samples non-aqueous liquid phase (n-heptane) was also present. The results of the induction time, gas uptake, and temperature showed that although

polyethylene oxide is not a KHI by itself, it can increase the value of induction time by one order of magnitude, compared to KHI only [28]. Hydrate formation is strongly dependent on driving force. In hydrate kinetic formation rate equation, this parameter is only a function of subcooling; however, it could be as a function of other parameters, including temperature, concentration of KHI, and pressure. The effect of pressure on the induction time for water/methane/NG samples with and without Luvicap EG was investigated at the same degrees of subcooling. It was found that for water/ pure gas samples, the driving force is proportional to the subcooling with a good approximation in a wide range of pressures at isothermal conditions [29]. The induction time of the samples with KHI decreased significantly when the system pressure increased [29]. Different chemicals have been examined in the literature to find appropriate KHIs in terms of their performance and environmental impacts [30-32]. Induction time was measured for hydrate formation of methane in the presence of tetraethylenepentamine polyalkylated amine oxides (TEPA-R-AO) and hyperbranched polyethyleneimine polyalkylated amine oxides (HPEI-R-AO) as KHIs. The results revealed that the HPEI-R-AO with pentyl and hexyl groups is a stronger KHI with a subcooling degree of 11.3 °C , where the HPEI-R-AO with six carbon atoms alkyl groups exhibited high induction time in different experiments [30]. The impact of PVP and L-tyrosine as KHIs on natural gas hydrate formation in a flow mini-loop system was evaluated. It was found that as L-tyrosine is a stronger KHI than PVP; even adding a small value of this inhibitor to PVP could significantly increase the induction time parameter [31]. Lee and Englezos [32] conducted the gas hydrate formation experiments for the mixtures of methane/ethane gases in the presence of KHIs such as GHI 101 and Luvicap EG at the pressure of 5100 kPa and the temperature of 273.7 (and/or 273.9 K). They measured the induction time of polyethylene oxide to study the effect of KHIs and water/solid interface on this parameter. According to the results, GHI 101 and Luvicap

EG were able to postpone hydrate nucleation, while adding polyethylene oxide to the samples with KHIs decreased the effect of hydrate memory on the induction time [32].

Luvicap 55W is a copolymer based on vinylpyrrolidone and vinyl caprolactam with a low molecular weight that is soluble in water. This inhibitor is a commercial inhibitor formulated by BASF. There are a few experimental research studies on the measurement of induction time for methane or natural gas hydrate formation in the presence of Luvicap 55W. Lim et al. (2021) obtained over 3000 experimental data points to investigate the effect of Luvicap 55W as a KHI (0 – 3 wt% in the water) on the methane hydrate formation in terms of subcooling and initial growth rate parameters with the operating pressure about 12 MPa. They utilized seven independent multiple high-pressure stirred automated lag time apparatuses (HPS-ALTA) to conduct the experiments. They made the conclusion that adding KHI reduces the stochastic feature of gas hydrate formation and lowers the average initial growth rates by a factor of five [33]. The impact of glycol ether on Luvicap 55W was investigated for the case of the natural gas hydrate formation with a temperature of 4 °C and pressure of 95 bar. It was found that glycol ether in the samples with different concentrations does not influence the induction time while increasing the glycol ether concentration decreases the growth rate of the hydrate [34].

There are several studies on gas hydrate modelling in the literature. For instance, a number of researchers focused on thermodynamic modeling to predict the temperature and pressure of hydrate formation/dissociation in different systems in the absence and presence of THIs [13, 35-43]. In addition, some studies have been conducted on kinetic hydrate modeling in the presence of KHIs [44-49].

For instance, Vysniauskas and Bishnoi developed a semi-empirical model for methane formation kinetic rate; the developed model is dependent on the interfacial area, pressure, temperature, and

degree of supercooling [50]. They introduced a kinetic model for ethane hydrate formation, and the model results were compared with the experimental data obtained in a temperature range of 274 - 282 K and a pressure range of 0.6-2.6 MPa [45]. In 1994, Skovborg and Rasmussen assumed that in the entire hydrate formation process, mass transfer of gas molecules from the gas phase to the liquid water is a controlling step for the kinetic hydrate formation rate based on the film theory model. They proposed a simplified hydrate kinetic model, and compared the model results with the experimental data [49]. Turner, Boxall [44] developed a hydrate formation rate with a first-order model where the rate constant was adjusted using experimental hydrate kinetic data from the literature. The model was then integrated with OLGA2000 to simulate hydrate formation phenomena in the flow loop, and calculate the pressure drop and fluid viscosity; the predictions were compared with the experimental flow loop data [44]. A natural gas hydrate growth shell model was suggested in which three limitation steps, including intrinsic kinetics, mass transfer, and heat transfer, were considered. This approach could model the natural gas hydrate growth in two inward and outward directions of the shell [46].

## **3.2 LITERATURE REVIEW**

Induction time is an essential parameter in the hydrate formation and growth processes. Researchers have made considerable efforts to find an appropriate model for calculating the induction time of gas hydrates from several years ago. The induction time has been investigated for methane, ethane, and carbon dioxide hydrate through experimental and theoretical studies [51]. According to crystallization phenomena, induction time is a function of the ratio of gas fugacity in experimental conditions to equilibrium conditions [51]. Kashchiev and Firoozabadi [48] defined induction time as the time needed to form a detectable volume of hydrate phase in the system. They developed a theoretical model to determine single gas hydrate formation induction time

where this parameter was a function of supersaturation in hydrate crystallization [48]. The semi-experimental three-parameter model was developed for the induction time of various systems, including methane and ionic liquid solutions, based on the chemical kinetic theory. The model parameters were optimized using experimental data [52]. Talaghat and Khodaverdilo [53] used the Natarajan model to calculate the induction time for different gas systems; in this model, they used the supersaturation ratio defined by [53].

In recent years, there has been growing interest in using deterministic smart tools such as least square support vector machine (LSSVM), adaptive network-based fuzzy inference system (ANFIS), and gene expression programming (GEP) to precisely predict the target parameters of complex systems based on pattern recognition [54-69]. Extremely randomized trees (Extra Trees) and LSSVM were applied to obtain the hydrate formation/dissociation temperature for different systems, including natural gas with salt(s) and alcohol(s). These models are able to correlate the target parameter with  $R^2$  (coefficient of determination) greater than 96%. The average absolute relative deviation percent (AARD%) values of the two models reveal that LSSVM and Extra Trees can predict the hydrate equilibrium temperature and pressure as the objective function with high precision [70]. Kamari et al. (2015) employed LSSVM to calculate natural gas hydrate equilibrium pressure, mono ethylene glycol (MEG) flow rate, and desired depression of the gas hydrate formation temperature (DHFT). The model predictions were in good agreement with experimental data where the total average absolute relative deviation errors for the gas hydrate equilibrium pressure, desired DHFT, and flow rate of MEG parameters were 0.15, 0.58, and 7.17, respectively [71]. Mesbah et al. (2020) developed the LSSVM algorithm to determine hydrate formation temperature (HFT) for natural gases with different components and compositions. This model was a robust model with an  $R^2$  of 0.9918, where it exhibited a high accuracy when compared with

conventional correlations and existing thermodynamic models [66]. The methane hydrate dissociation in the presence of different ionic liquids with anion groups of sulfate, dicyanamide, tetrafluoroborate, and halides was modeled using LSSVM, ANFIS, and classification and regression tree (CART). The independent input parameters for these models were the system pressure, critical pressure and critical temperature of ionic liquids, and composition of ionic liquid solutions. The accuracy of the LSSVM model was greater than two other models since the value of AARD% of this model was 0.08 when compared to CART and ANFIS models with AARD% of 0.31 and 0.10, respectively [56]. Qin et al. (2019) used several machine learning models such as support vector machine (SVM) and artificial neural network (ANN) algorithms to determine hydrate fraction and the possibility of hydrate blockage in the pipeline. They collected 4500 experimental data points using the pilot-scale flow loop facilities, and various independent input parameters such as water cut, gas-oil ratio, hydrate particle cohesive force, fluid velocity, oil viscosity, specific gravity, and interfacial tension were utilized for the modeling [72]. Hydrate may form when a natural gas passes through a throttling process; thus, adjusting the inlet gas temperature is crucial. ANFIS, LSSVM, and radial basis function ANN (RBF-ANN) models were applied to predict the initial gas temperature. It was found that these models could forecast this parameter precisely with an  $R^2$  more than 0.99 and AARD% less than 0.5. However, the results of the RBF-ANN model were more accurate [73]. The hydrate equilibrium pressure for sour gas mixtures in different conditions was modeled using ANFIS, and compared with the results obtained from the available thermodynamic models. It was revealed that the ANFIS model surpasses the existing thermodynamic models so that the introduced model was able to predict the hydrate equilibrium pressure with high accuracy over various ranges of temperatures and sour gas concentrations [67]. Mehrizadeh employed two smart models, including ANN and ANFIS, to

estimate the hydrate formation pressure of various gas systems. It was found that the ANFIS model has a greater predictive performance compared to the ANN model so that the results of the former model were in more agreement with experiments than the latter [74]. Although there are many research studies in the literature that have used the GEP model in different fields [60, 61, 75-77], only one paper was published to determine HFT using the GEP model [78]. The GEP model was employed to predict HFT for various systems (sour gas, acid gas, and sweet gas mixtures) using 279 experimental data. It was concluded that the GEP model could accurately calculate the HFT for different systems with the average absolute relative error (AARE%) of 0.1397% [78].

As earlier mentioned, induction time is a critical parameter for gas hydrate formation in oil and gas facilities, specifically when a KHI is injected into subsea pipelines. KHIs postpone hydrate nucleation and growth in the oil and gas facilities so that the induction time increases dramatically in the system. Therefore, an accurate estimation of induction time is vital to prevent possible problems that may occur over hydrate formation in pipelines when the multiphase flow enters the hydrate formation zone. Several studies are available in the literature that have utilized smart models to calculate/predict the key parameters in the oil and gas industries [59, 79-86]. However, there are rarely published papers for the calculation of induction time for the methane hydrate systems in the presence of Luvicap 55 W as a KHI with various deterministic tools such as LSSVM, ANFIS, and GEP. Thus, this study aims to fill this knowledge gap. Figure 3-1 displays a general sketch of this research. The deterministic models (LSSVM, ANFIS, and GEP) are proposed for accurate prediction of induction time in terms of input parameters, including subcooling, KHI (Luvicap 55 W solution) concentration, molecular weight of the KHI solution, pressure, and temperature. The intelligent models are developed using 440 experimental data, where the data points are divided into two dataset groups, including training (85%) and testing

(15%). This chapter is structured as follows: after the introductory section, the models are briefly described. Then, the methodology is illustrated in section 3. The results and discussion are provided in section 4. Section 5 includes data collection and parametric sensitivity analysis. The conclusions are presented in the final section.

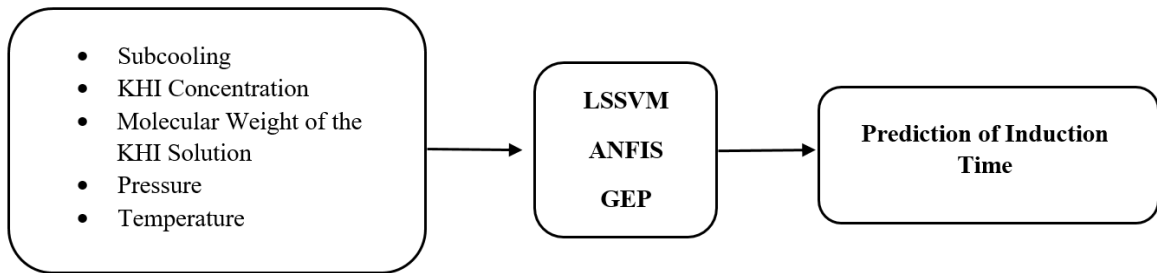


**Figure 3-1.** General sketch for induction time calculation using deterministic models.

### 3.3 THEORY OF DETERMINISTIC MODELS

This section presents a brief theory of three deterministic models, including LSSVM, ANFIS, and GEP.

#### 3.3.1 LSSVM Model

The support vector machine (SVM) was introduced for the first time by Vapnik [87, 88]. This robust mathematical tool can solve various complicated problems and help in systematic data analysis [89]. Although the SVM method is formulated as a quadratic programming problem with linear inequality constraints, it requires a high computational load to solve regression problems with the inequality constraint [17, 90]. The SVM algorithm is not appropriate for large databanks, which is considered as a significant disadvantage of this approach [56]. The least-squares SVM (LSSVM) algorithm, which was introduced by Suykens and Vandewalle (1999), resolved this

issue. This method is able to solve a set of linear equations instead of using a quadratic programming solution; this technique might be easier and faster than the conventional SVM [91, 92]. In other words, the LSSVM algorithm can handle large data sets with a reasonable accuracy where the inequality constraint has changed to equality constraint [93].

Suppose that the input ( $x_k$ ) and output data ( $y_k$ ) are assumed to be in the following form [93]:

$$D = \{(x_1 - y_1), \dots, (x_k - y_k), \dots, (x_n - y_n)\} , \quad x_k \in R^n, y_k \in R \quad (3-1)$$

The experimental data can be approximated by a nonlinear function as shown below [90, 93]:

$$f(x) = w^T g(x) + b \quad (3-2)$$

where  $g(x)$  presents a nonlinear mapping function that assigns  $x$  into  $n$ -dimensional feature space where the linear regression is accomplished. Note that  $w$  stands for the weight vector and  $b$  represents the bias term. The optimization problem for the LSSVM algorithm can be formulated as follows [90, 93]:

$$\min J(w, e) = \frac{1}{2} w^T w + \frac{1}{2} \mu \sum_{k=1}^{Nn} e_k^2 \quad (3-3)$$

According to the above equation, the linear constraint is given below [90, 93]:

$$y_k = (w^T g(x)) + b + e_k \quad k = 1, 2, \dots, n \quad (3-4)$$

where  $e_k$  refers to the regression error,  $\mu \geq 0$  stands for the regularization parameter, and  $T$  presents the transport of weight matrix. If the linear constraint equation is incorporated into the optimization problem, the following expression is obtained [90]:

$$LSSVM = \frac{1}{2} w^T w + \frac{1}{2} \mu \sum_{k=1}^n e_k^2 - \sum_{k=1}^n \beta_k \{(w^T g(x)) + b + e_k - y_k\} \quad (3-5)$$

where  $\beta_k \in R$  symbolizes the Lagrangian multipliers, which can be positive or negative based on the LSSVM equation. According to the Lagrangian multipliers, differentiation of the LSSVM equation with respect to  $b$ ,  $w$ ,  $\beta_k$ , and  $e_k$  gives [90, 93]:

$$\begin{cases} \frac{\partial LSSVM}{\partial b} = 0, & \Rightarrow \sum_{k=1}^n \beta_k = 0 \\ \frac{\partial LSSVM}{\partial w} = 0 & \Rightarrow w = \sum_{k=1}^n \beta_k g(x_k) \\ \frac{\partial LSSVM}{\partial \beta_k} = 0 & \Rightarrow (w^T g(x)) + b + e_k - y_k = 0, \quad k = 1, 2, \dots, n \\ \frac{\partial LSSVM}{\partial e_k} = 0 & \Rightarrow \beta_k = \mu e_k, \quad k = 1, 2, \dots, n \end{cases} \quad (3-6)$$

When a linear relationship between the dependent and independent variables for the LSSVM model is assumed, the following equation can be written [90] :

$$y = \sum_{k=1}^n \beta_k x_k^T x + b \quad (3-7)$$

The above equation is only valid for linear regression problems. However, the Kernel function ( $K(x_k, x)$ ) should be inserted in the above equation to make solving nonlinear regression problems possible, as given below [90]:

$$y = \sum_{k=1}^n \beta_k K(x_k, x) + b \quad (3-8)$$

The Kernel function of  $K(x_k, x)$  is calculated using the inner product of  $g(x)$  and  $g(x_k)$  vectors as shown below [90]:

$$K(x_k, x) = g(x)g(x_k)^T \quad (3-9)$$

There are a number of Kernel equations that can be employed in the LSSVM model [94, 95]; however, RBF function (Eq. (10)) and polynomial function (Eq. (11) ) are usually used in the LSSVM algorithm, as written below

$$K(x_k, x) = \exp (-\|x_k - x\|^2/\sigma^2) \quad (3-10)$$

$$K(x_k, x) = (1 + x_k^T x)^d \quad (3-11)$$

where  $\sigma^2$  stands for the Kernel width that is optimized in the training phase, and  $d$  refers to the degree of the polynomial [92, 93, 96]. Figure 3-2 depicts the simple architecture of the LSSVM model.

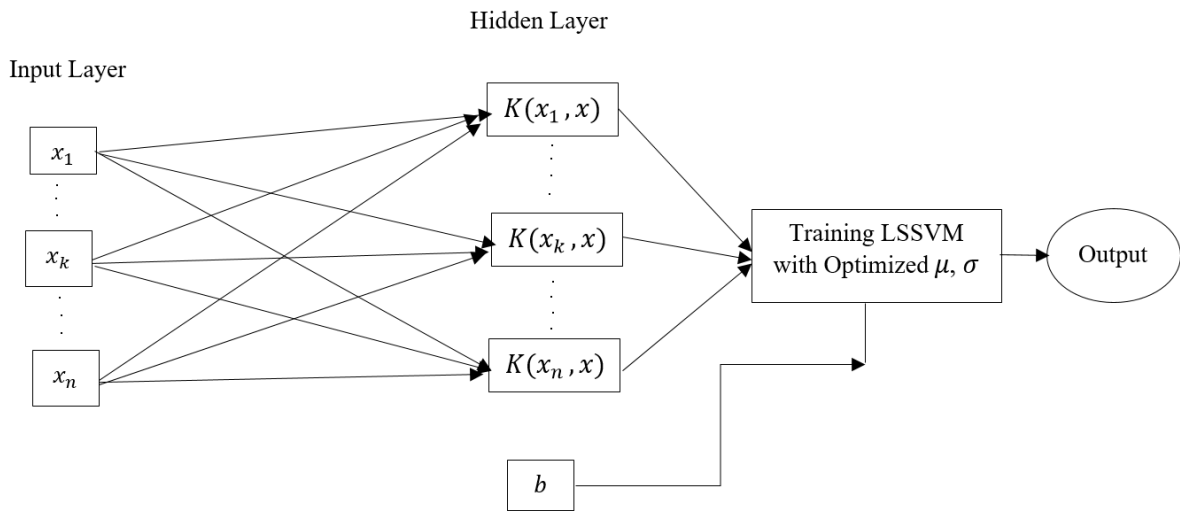


**Figure 3-2.** Structure of the LSSVM method (modified after Shaberi and Suhartono [97]).

### 3.3.2 ANFIS Model

The adaptive network-based fuzzy inference system (ANFIS) was developed by Jang [98]. It combines an artificial neural network (ANN) system with a fuzzy inference system (FIS) so that its algorithm is able to eliminate the disadvantages of ANN and FIS [73]. The ANFIS model is based on a fuzzy logic model with particular rules, where they are developed during the model training phase [99]. In the ANFIS theory, Takagi–Sugeno systems are used for the FIS part since they are computationally efficient in conjunction with optimization methodologies [73]. Figure 3-3 illustrates the ANFIS model structure, which includes six layers for a system with two inputs and one output parameter. In this model, layer zero involves the input nodes ( $x_1$  and  $x_2$ ), layer 6 refers to the output node ( $f$ ), and the hidden layers include the nodes of membership functions (MFs) and rules. In the ANFIS model, if-then fuzzy rules are used for the relationship between the input and output parameters [99].

Although there are three fuzzy logic categories (Mamdani-type, the relational equation, and the Takagi–Sugeno–Kang (TSK)) that can be employed for the fuzzy section, only TSK model with zero or first order is used in the ANFIS approach to increase the computational efficiency and guarantee the continuity of output surface. The TSK with R rules models in the ANFIS method can be defined as follows [98-100]:

$$\text{Rule 1: if } x_1 \text{ is } K_1^i \text{ and } x_2 \text{ is } K_2^i \dots, \text{ and } x_n \text{ is } K_s^i = K_n^i \quad (s = 1, 2, 3, \dots, n) \quad (3-12)$$

$$\text{then } f_i(x) = c_0^i + c_1^i x_1 + c_2^i x_2 + \dots + c_n^i x_n \quad (i = 1, 2, 3, \dots, R), \quad (j = 0, 1, 2, 3, \dots,$$

.,  $n$ )

where  $c_j^i$  denotes the consequence parameters that can be calculated during the training process,  $f_i(x)$  presents the output of  $i^{\text{th}}$  rule, and  $K_s^i$  introduces the linguistic label. As mentioned earlier, the ANFIS model has six layers; layer zero and layer six are the input and output, while other layers from one to five are the Fuzzification, Rule, Normalization, Defuzzification, and Summation layers.

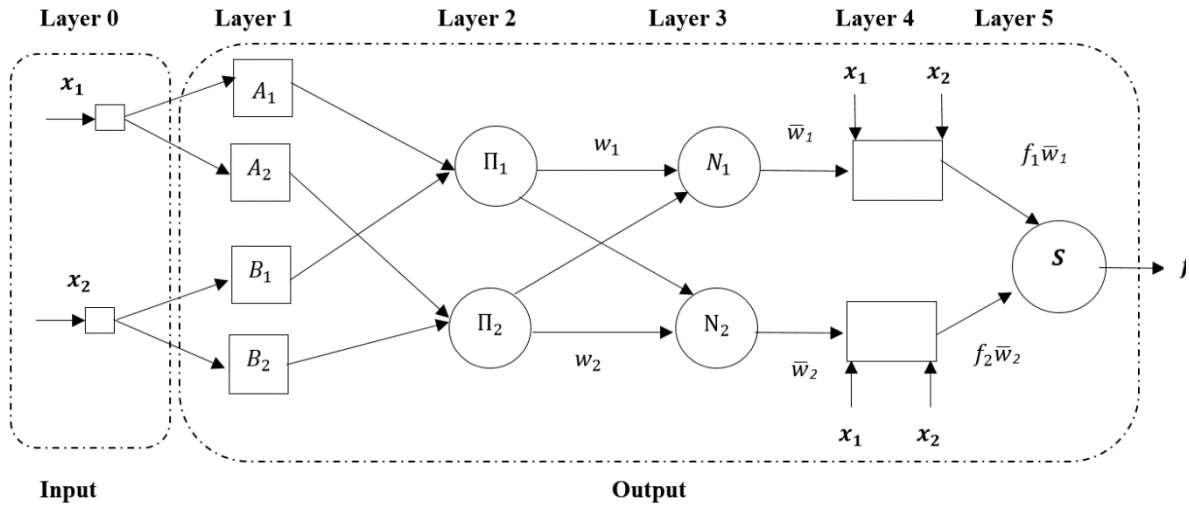


**Figure 3-3.** ANFIS model structure for a system with two inputs  $x_1, x_2$ , and one output (modified after [99]).

In the ANFIS model, the layers for transforming input to output can be defined as follows:

Layer zero includes the input parameters such as  $x_1$  and  $x_2$ . In the first layer (the Fuzzification layer), the MFs are employed for input parameters where every node  $i$  is an adaptive node with a function node, as shown below [98-100]:

$$Q_1^i = \mu_{K_s^i(x_s)} \quad s=1, 2, \dots, n \quad (3-13)$$

where  $Q_1^i$  is the output of layer one,  $x_s$  symbolizes the input into node  $i$ , and  $\mu_{K_s^i(x_s)}$  stands for a MF for  $x_s$ . In the second layer or rule layer, there are the fixed nodes with the label of  $\Pi_i$  where

the output of these nodes equals the product of Gaussian membership function nodes of the first layer, as given below [98-100]:

$$Q_2^i = w_i(x) = \prod_{s=1}^n \mu_{K_s^i}(x_s) \quad (3-14)$$

where  $Q_2^i$  presents the output of the second layer and  $w_i$  resembles the firing strength of the  $i$ th rule. The third layer is the normalized layer, in which the nodes are the normalized values of firing strengths,  $w_i$ . The formulation of the firing strengths normalization is defined as follows [98-100]:

$$Q_3^i = \bar{w}_i(x) = \frac{w_i(x)}{\sum_{i=1}^R w_i(x)} \quad (3-15)$$

where  $Q_3^i$  stands for the output of the third layer and  $\bar{w}_i$  refers to the normalized firing strength.

In the fourth layer or Defuzzification layer, the adaptive nodes with a function node fuzzified in the first layer are defuzzified based on the following equation [98-100]:

$$Q_4^i = \bar{w}_i(x) f_i(x) = Q_3^i (c_0^i + c_1^i x_1 + c_2^i x_2 + \dots + c_n^i x_n) \quad (3-16)$$

The fifth layer is the overall output layer, which is the summation of all layers (1 to 4) for  $R$  rules as follows [100]:

$$Q_5^i = f(x) = \sum_{i=1}^R Q_4^i \quad (3-17)$$

### 3.3.3 GEP Model

Gene expression programming (GEP) is a new artificial intelligence technique that was introduced by Ferreira [101]. This method has more advantages compared with genetic programming [78]. GEP algorithm was created based on genetic algorithms (GA) and genetic programming (GP), where this integrated computer program is much faster than standalone GA [61, 102]. The GEP model requires a set of data to develop a mathematical function using the genetic operators of GA

[102]. In the GEP model, an initial population of various correlations, which are codified in the form of chromosomes with linear strings and the fixed sizes, is created. These chromosomes are converted into the expression tree (ET) with terminals and the head involving functions in the GEP algorithm. The combination of ET and chromosomes results in a model with high precise and reliable performance [61]. According to the GEP algorithm, the symbols of nodes and chromosomes are displayed in the tree, where the rules of the model can define the nodes in the tree and their interaction types in sub-ETs. GEP model has two languages, including genetic and ET languages, where this bilingual notation is called Karva in this model. Figure 3-4 demonstrates the ET with a mathematical expression of  $(x\sqrt{ab + cd})$  [103]. The steps followed to run the GEP model and attain the best regression for the output parameter are given in Figure 3-5. According to Figure 3-5, in the beginning, random chromosomes are generated from the initial population after the data analysis step. Then, these chromosomes evaluate fitness after converting to the ET. Based on the fitness evaluation, the chromosome is selected in terms of their fitness to reproduce with modification in this step. After that, this process repeats several times until a good solution is achieved from the GEP model [103].

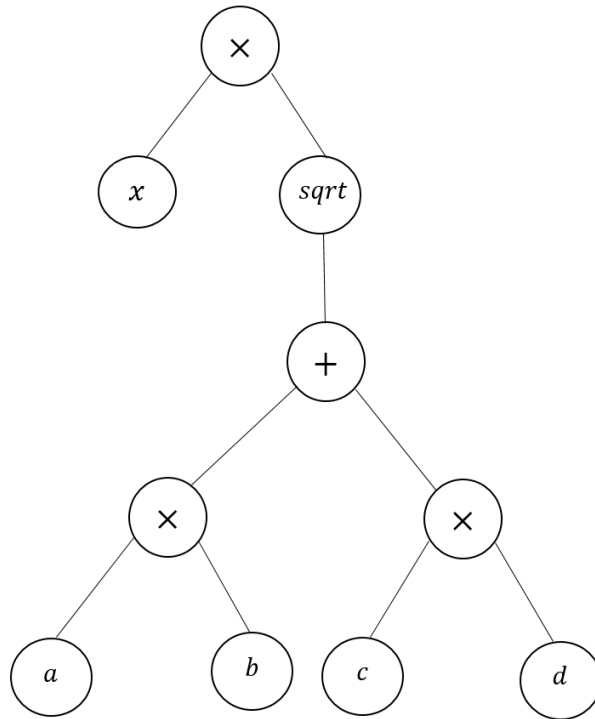


**Figure 3-4.** An example of an expression tree of  $(x\sqrt{ab + cd})$  for GEP model (adapted from Mohammed & Sharifi [103]).

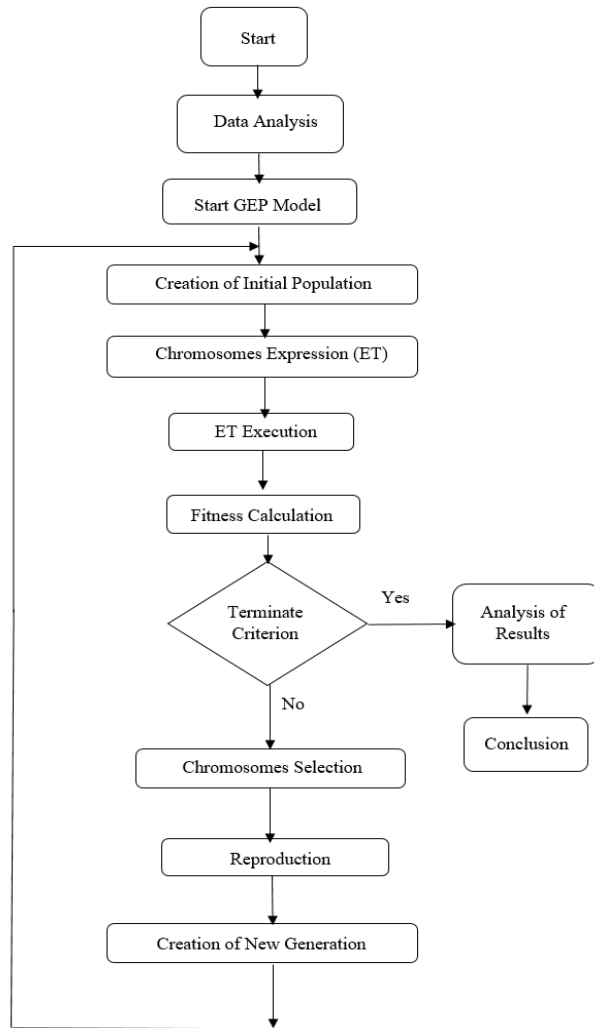


**Figure 3-5.** Flowchart of the GEP model (modified after [104]).

### **3.4 METHODOLOGY: KEY STEPS**

In this chapter, three intelligent models, including LSSVM, ANFIS, and GEP, are employed to calculate the induction time of the methane hydrate formation in the presence of Luvicap 55 W (KHI) solutions. The models are validated using experimental data. The model results are then compared with each other to examine their predictive performances. Furthermore, the parametric

sensitivity analysis is performed based on the ANFIS strategy to determine the importance of each input parameter on the induction time as the objective function.

### 3.4.1 Data Analysis

Gathering a high amount of data from the open sources is the first step to introduce proper deterministic models. The dependent and independent parameters should be then specified as the output and inputs of the models. Induction time can be considered a vital specification of KHIs such as Luvicap 55 W that may create a delay in the gas hydrate crystallization, growth rate of hydrate crystals, and hydrate particle agglomeration. KHIs with a long induction time seem to be more appropriate in gas and oil production facilities where fluids transport through the subsea pipelines without any blockages due to hydrate formation [48, 105]. In this study, induction time ( $t_i$ ) is considered as a target variable, and is related to the molecular weight of solution ( $MW_{sol}$ ), mass fraction of KHI ( $m_i$ ), temperature ( $T_{exp}$ ), system pressure (P), and subcooling ( $\Delta T$ ) parameters as the input parameters based on previous research studies. For instance, pressure and temperature are two key parameters in gas hydrate formation because the favorite conditions for the methane hydrate formation are high pressures and low temperatures [1, 106]. Although the concentration of KHIs in the aqueous phase is relatively low in production facilities (e.g., 1wt%), different experimental studies reveal that this parameter has a significant impact on the induction time [107-109]. Subcooling is another input parameter that is calculated as a difference between the system temperature and equilibrium temperature on the hydrate phase boundary at the system pressure. This parameter is a driving force in hydrate nucleation and growth [26, 29]. It was found that the molecular weight of the solution is a key input parameter that can influence hydrate formation and induction time [26]. According to the above discussion, the induction time is a function of input parameters in the following form:

$$t_i = f (Mw_{sol}, m_i, T_{exp}, P, \Delta T) \quad (3-18)$$

In Eq. (18),  $t_i$  introduces the induction time,  $Mw_{sol}$  is the molecular weight of the solution, and  $m_i$ ,  $T_{exp}$ ,  $P$ , and  $\Delta T$  refer to the mass fraction of Luvicap 55 W, experiment temperature, system pressure, and subcooling, respectively. Although several technical documents have been published on KHI performances [30, 110-112], there is no sufficient database of induction time measurements for Luvicap 55 W in the literature. Therefore, the required experimental data (440 data points) has been borrowed directly from the authors [33] at the University of Western Australia, for this research work. The histogram of experimental data is displayed in Figure 3-6.

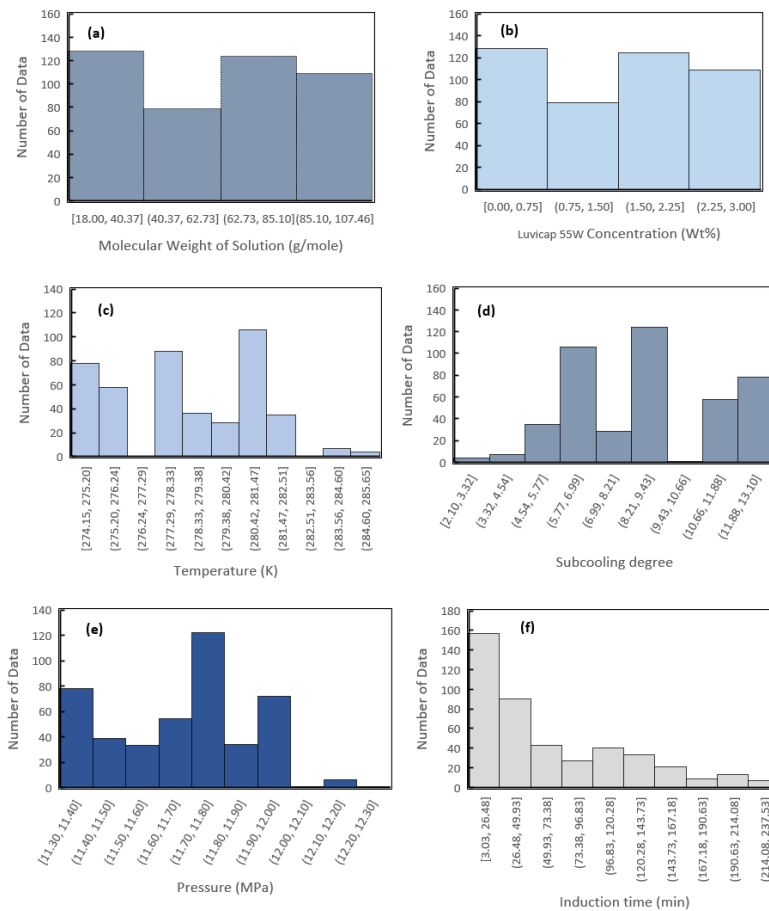


**Figure 3-6.** The histograms of experimental data: (a) Molecular weight of solution, (b) Luvicap 55 W concentration, (c) Temperature, (d) Subcooling, (e) Pressure, and (f) Induction time.

Table 3-1 indicates the statistical analysis of experimental data utilized in this study. It can be seen that the molecular weight of the solution varies between 18 and 107.46 g/gmol, while the concentration (*m*%) of Luvicap 55 W is between 0 to 3 wt%. Subcooling values according to Table 1 change from 2.1 to 13.1. In addition, the experimental temperature and pressure ranges are 274.15 - 285.65 K and 11.3 - 12.3 MPa.

In this study, collected experimental data are split randomly into two subgroups containing training (85%) and testing (15%) sets before running the models. Training data set is needed for developing the models, while the testing data set is used to evaluate the accuracy of the trained models. The criteria for the termination of the modeling is when  $R^2$  value is close to one. It is worth noting that the quality and quantity of the collected data significantly influence the performance of developed models. Therefore, finding reliable data points is vital to develop accurate and reliable developed models.

**Table 3-1.** Summary of experimental data.

<b>Experimental Parameter</b>	<b>Min<sup>a</sup></b>	<b>Mean<sup>b</sup></b>	<b>Max<sup>c</sup></b>	<b>SD<sup>d</sup></b>
Molecular weight of solution(g/mole)	18	64.70	107.46	31.42
Concentration of Luvicap 55W (m%)	0	1.565	3.00	1.054
Temperature (K)	274.15	278.59	285.65	2.832
Pressure (MPa)	11.3	11.71	12.30	0.227
Subcooling degree	2.10	8.88	13.10	2.693
Induction time (min)	3.033	62.66	237.53	58.22

Note: a= Minimum experimental parameter; b= Average of an experimental parameter; c= Maximum experimental parameter; and d= Standard deviation

### 3.4.2 Modeling Tool Selection

In this research, LSSVM and ANFIS models are developed using Matlab software. GeneXproTools software package version 5 is used to develop the GEP model. Three models are applied to determine the induction time of methane/ Luvicap 55 W/ water systems. Using the two

models (LSSVM and ANFIS), the input and target (output) experimental data are normalized between -1 and +1 to prevent numerical overflow in running the programs and obtain convergence.

The normalization of the data is performed based on the following equation:

$$\hat{x} = 2 \frac{x_i - x_{min}}{x_{max} - x_{min}} - 1 \quad (3-19)$$

where  $\hat{x}$  is the normalized value of  $x_i$ , and  $x_{max}$  and  $x_{min}$  present the maximum and minimum values of experimental data.

### 3.4.3 Model Evaluation Criteria

To examine the performance of LSSVM, ANFIS, and GEP models, statistical parameters, including average relative error percent (ARE%), average absolute relative error (AARE%), and coefficient of determination ( $R^2$ ), are employed. The mathematical expressions of these statistical evaluation parameters are given below [56, 66, 113, 114]:

$$ARE\% = 100 \sum_{i=1}^n \left( \frac{x_t^i - x_p^i}{x_t^i} \right) / n \quad (3-20)$$

$$AARE\% = 100 \sum_{i=1}^n \left| \frac{x_t^i - x_p^i}{x_t^i} \right| / n \quad (3-21)$$

$$R^2 = 1 - \frac{\sum_{i=1}^n (x_t^i - x_p^i)^2}{\sum_{i=1}^n (x_p^i - \text{average}(x_t^i))^2} \quad (3-22)$$

in which,  $x_t^i$ ,  $x_p^i$ , and  $n$  resemble the experimental value, calculated/predicted value, and number of data points, respectively. Generally, lower values of ARE% and AARD% (close to zero) and  $R^2$  close to 1 imply that the models are able to produce more reliable data.

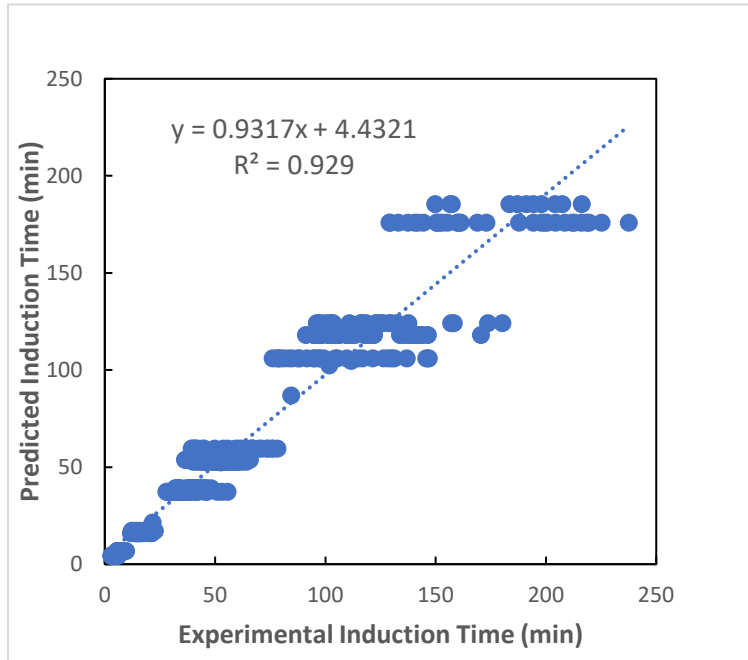
## 3.5 RESULTS AND DISCUSSION

In this study, three models (LSSVM, ANFIS, and GEP) are employed to calculate the induction time for the methane/Luvicap 55W/ water samples using input data of  $Mw_{sol}$ ,  $m_i$ ,  $T_{exp}$ ,  $P$ , and subcooling. 440 experimental data points are utilized for training and then testing these models. The performance of the deterministic models is discussed in this section.

### 3.5.1 LSSVM Model Performance Evaluation

LSSVM with radial kernel function, which includes two parameters of kernel width ( $\sigma^2$ ) and regularization parameter ( $\mu$ ), is used to determine the induction time of methane/ Luvicap 55W/ water systems. Finding the optimized kernel parameters is important for the accurate prediction of induction time. In this work, the optimum values of kernel width ( $\sigma^2$ ) and regularization parameter ( $\mu$ ) are 5.397 and 18.064, respectively. Figure 3-7 displays the experimental data and predicted induction time for two cases of training and testing using the LSSVM model. It should be noted that the run time of this model is five seconds. According to Figure 3-7, there is good agreement between the actual data and the LSSVM predictions, where the  $R^2$  for the training and testing phases are 0.929 and 0.940, respectively. The histogram of the average relative errors (ARD%) for the LSSVM model is demonstrated in Figure 3-8. ARD% values show whether a model underestimates or overestimates the target parameter. It is concluded that ARD% for about 40 experimental data is between -0.51 and 0.005, while 4 data points have an error of more than 0.394.

(a) Training



(b) Testing

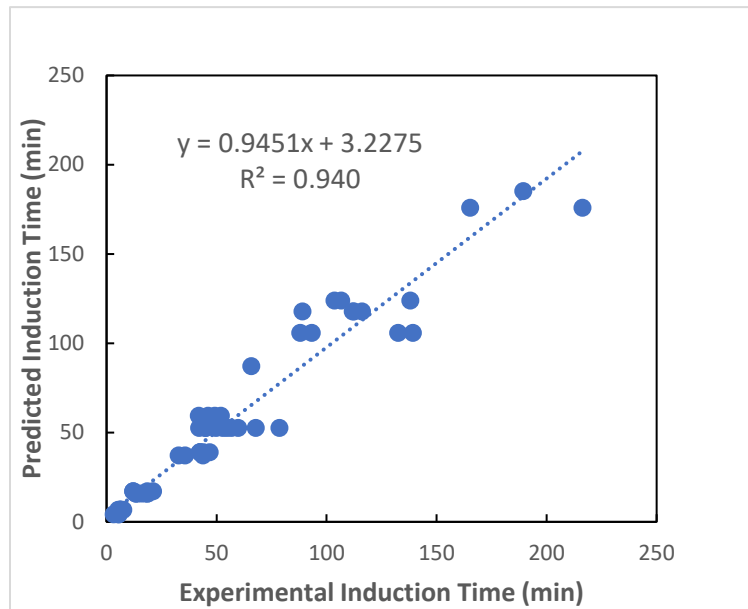


**Figure 3-7.** Performance of LSSVM model: (a) Training and (b) Testing.

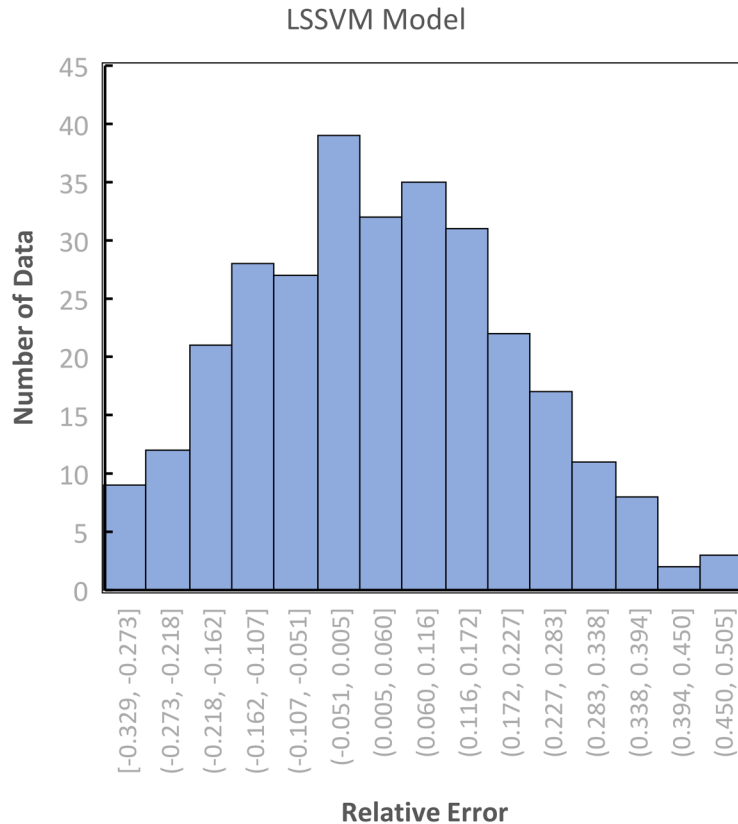


**Figure 3-8.** Histogram of relative errors for LSSVM model.

### 3.5.2 ANFIS Model Performance Evaluation

The ANFIS algorithm is based on Takagi-Sugeno Fuzzy inference system [98]. This model is capable of learning from introduced data because the Fuzzy part of the ANFIS model uses linguistic terms and If-Then rules [56]. The specifications of the developed ANFIS model are given in Table 3-2. In this study, the MF employed for the ANFIS model is Gaussian. MF is a function that shows the degree of an independent parameter that belongs to a set. MFs of the independent parameters (input parameters) after the learning process are displayed in Figure 3-9. Prior to the prediction step, the data of training and testing phases for the input and target variables are normalized to avoid numerical overflow due to the presence of too large and/or too small values.

Figure 3-10 depicts the training and testing performance of the developed ANFIS model for the induction time predictions according to Gaussian-based MFs. It can be seen that the  $R^2$  values of the training and testing phases for the ANFIS model are 0.9299 and 0.9437, respectively, and there is an acceptable match between the model calculations and experimental data. Figure 3-11 shows the ARD% of the developed ANFIS model. ARD% with a negative value indicates that the ANFIS model underestimates the objective function, while ARD% with a positive value shows the model overestimates the induction time. According to Figure 3-11, the ARD% for 58 data points is between -0.04 and 0.02, while less than 5 experimental data points have an error of higher than 0.37.

**Table 3-2.** ANFIS model specifications to predict the induction time for methane + Luvicape 55W+ water systems.

<b>Parameter</b>	<b>Definition/Value</b>
Fuzzy structure	Sugeno-type
Initial FIS for training	Genfis2
Membership function type	Gaussian
Output membership function	Linear
Number of inputs	5
Number of outputs	1
Number of Fuzzy rules	11
Maximum number of epochs	700
Initial step size	0.03
Step size decrease rate	0.9
Step size increase rate	1.1

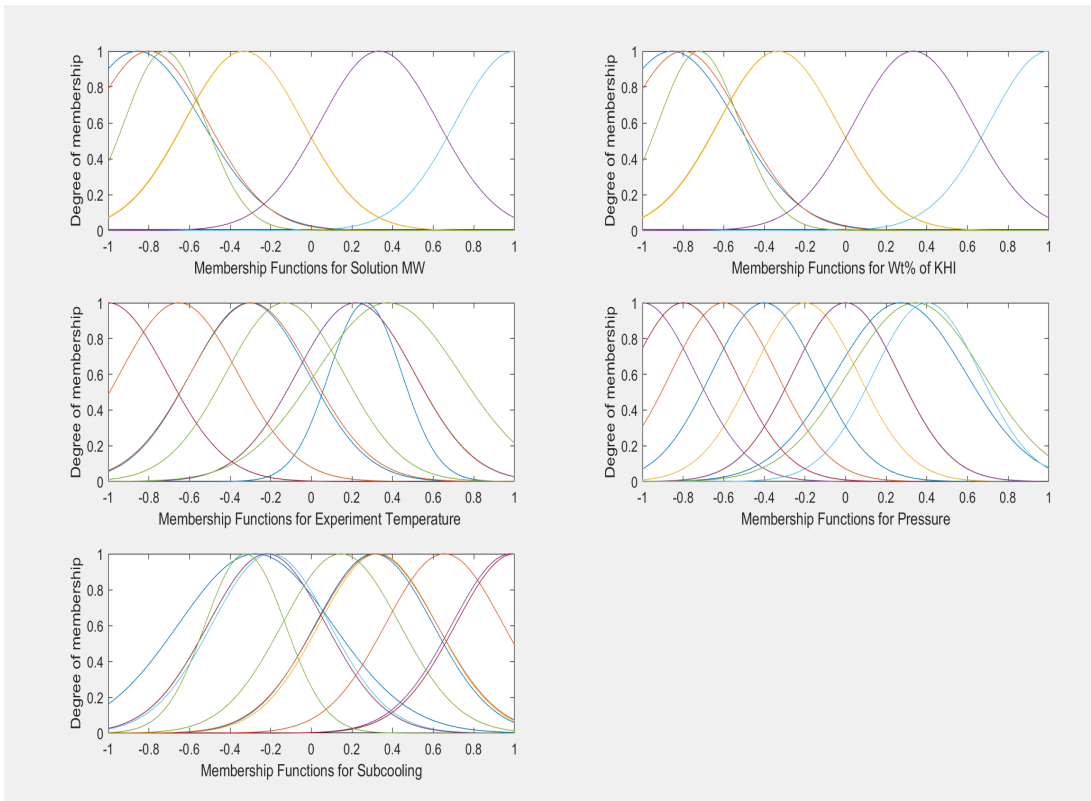
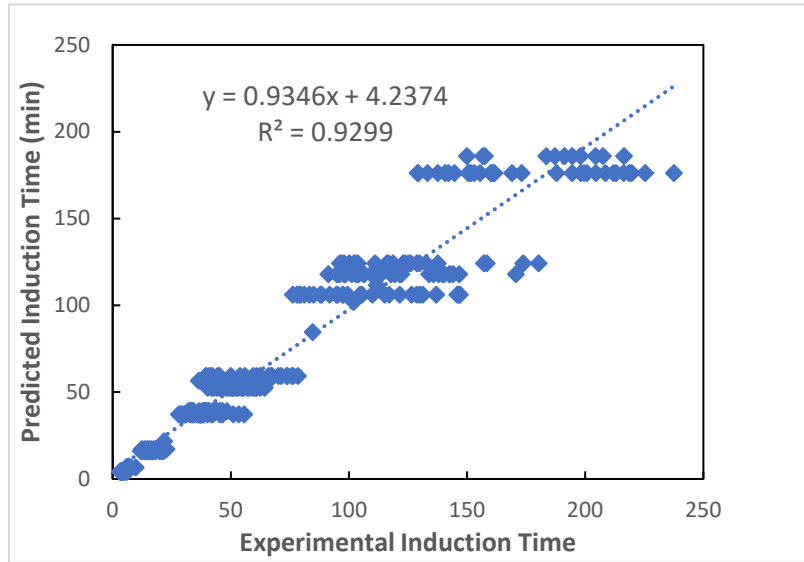


**Figure 3-9.** Membership functions for input parameters of developed ANFIS model.

(a) Training



(b) Testing

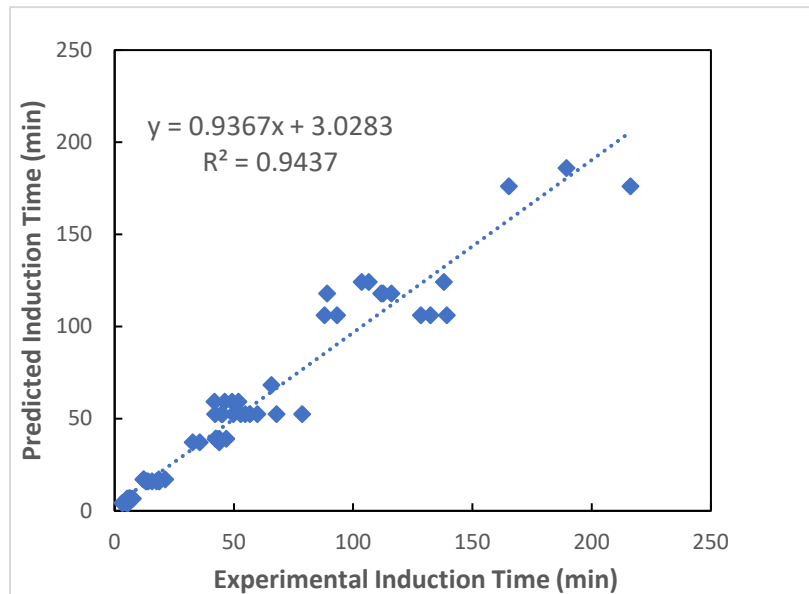


**Figure 3-10.** Performance of ANFIS model: (a) Training and (b) Testing.

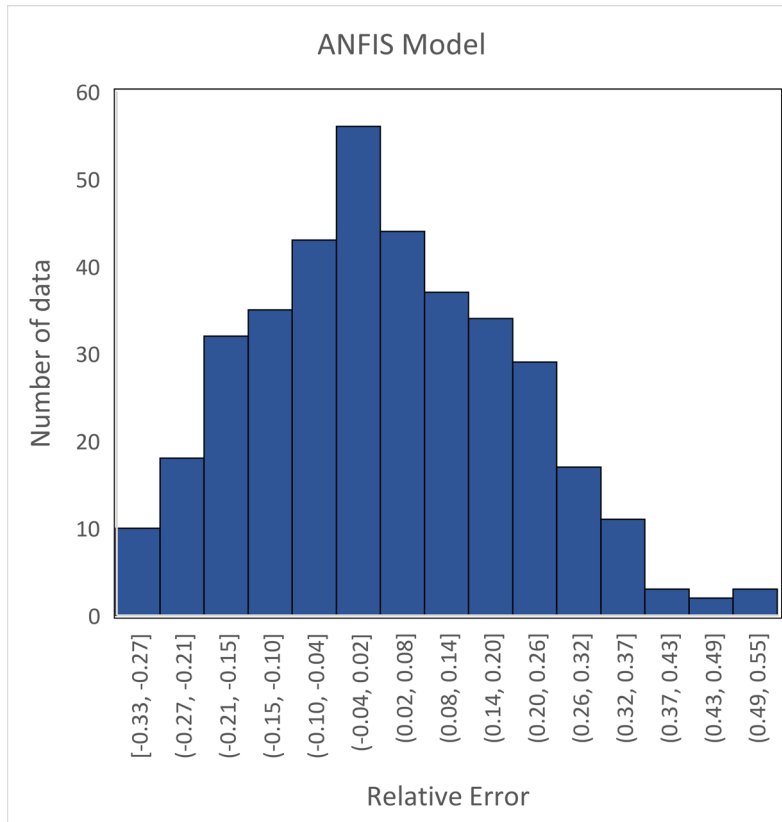


**Figure 3-11.** Histogram of relative errors for ANFIS model.

### 3.5.3 GEP Model Performance Evaluation

The predictive performance of the GEP method is evaluated for the calculation of induction time of methane hydrate formation in the presence of the Luvicap 55W solutions. The adjustable parameters of the GEP model are calibrated properly to ensure robustness in the modeling calculation. The accuracy of the model increases when the number of genes and chromosomes increases. In this study, the numbers of genes and chromosomes are set to 4 and 70, respectively. Table 3-3 lists the final values of adjustable parameters employed in this study. As Figure 3-12 displays, the values of  $R^2$  for the training and testing phases are 0.9726 and 0.9582. According to Figure 3-12, there is an excellent agreement between the experimental data and calculated/predicted results of the GEP model. The histogram of ARD% for the deterministic GEP

model is demonstrated in Figure 3-13. As it is clear from Figure 3-13, ARD% for most of the data is between -0.66 and 0.54; only less than 15 data points have the maximum errors between 3.54% and 3.84%. The ETs of the developed GEP model based on four-gene chromosomes are depicted in Figure 3-14. Several computational runs are performed based on the trial and error procedure to find the best explicit correlation, which is expressed below:

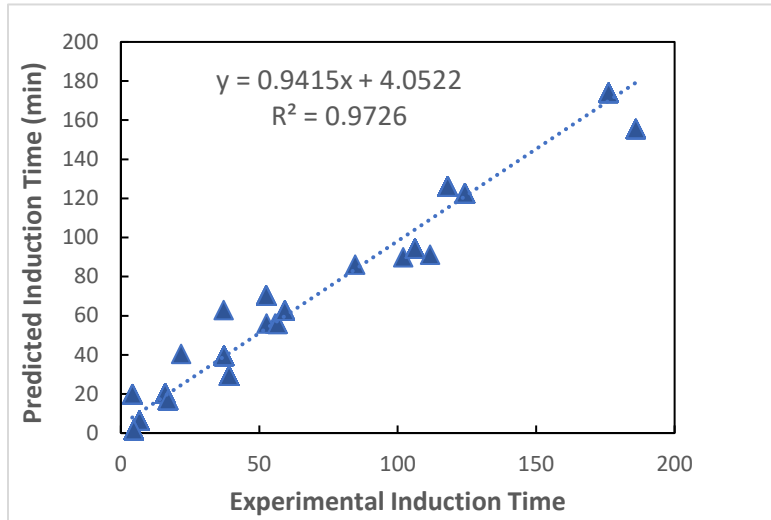
$$t_i = 0.5 x_3 + A_1 + A_2 - 4.881 \times A_4 \times \log(\exp(x_2 + A_3)) - P + A_5 + 63.1024 \times A_6 \quad (3-23)$$

where the expressions of  $A_1$  to  $A_6$  are presented in Table 3-4. Note that  $x_1$  to  $x_6$  introduce the input variables, including the molecular weight of solution ( $Mw_{sol}$ ), mass fraction of KHI ( $m_i$ ), temperature (Texp), system pressure (P), subcooling ( $\Delta T$ ) parameters, and induction time ( $t_i$ ).

**Table 3-3.** Specifications of GEP model to determine the induction time for methane + Luvicap 55W+ water systems.

<b>Parameter</b>	<b>Value</b>
Chromosome	70
Gene	4
Mutation rate	0.009
Inversion rate	0.005

(a) Training



(b) Testing

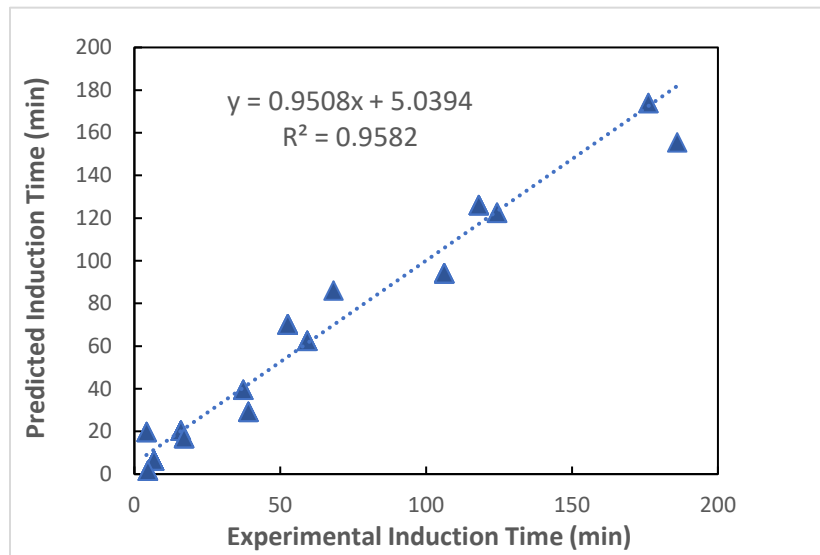
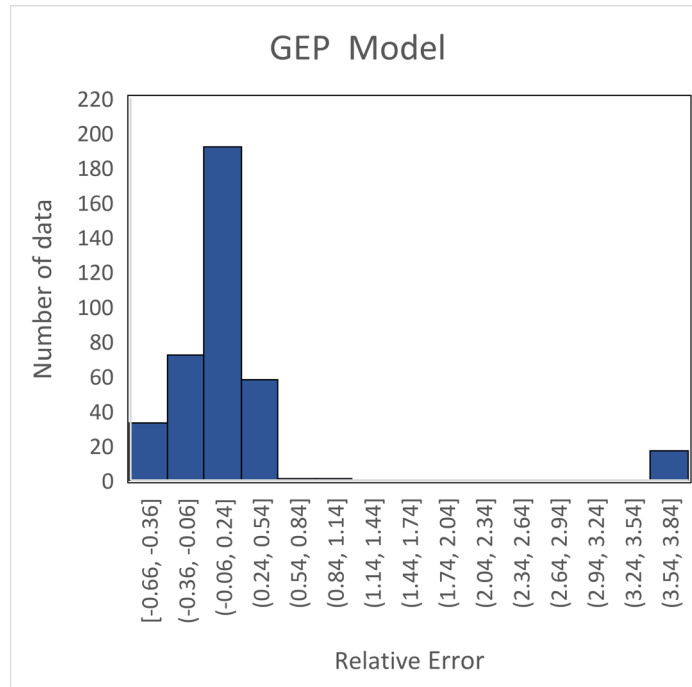


Figure 3-12. Performance of GEP model: (a) Training and (b) Testing.

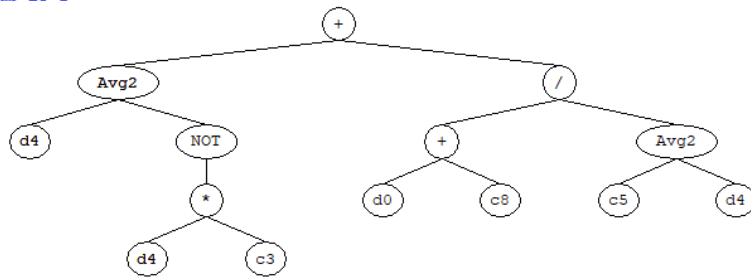


**Figure 3-13.** Histogram of relative errors for GEP model.

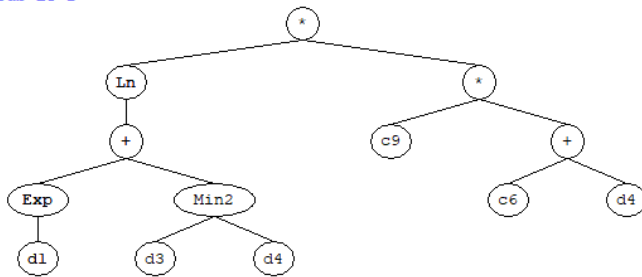
**Table 3-4.** The parameters of GEP correlation.

<b>Parameter</b>	<b>Mathematical Formulation</b>
$A_1$	$(1 - x_3 \times 3.9097)/2$
$A_2$	$2 \times (x_1 - 7.2639)/(x_3 - 4.2393)$
$A_3$	$\min(P, x_3)$
$A_4$	$x_3 - 5.7767$
$A_5$	$\min[(x_3 + \sqrt[3]{T \times x_1}), (4.6488 \times (x_3 - 9.1186)^2)]$
$A_6$	$\arctan(\sqrt[3]{x_1})$

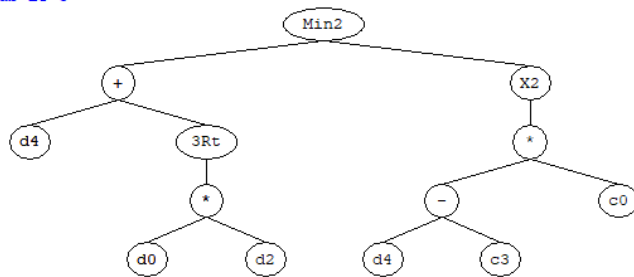
Sub-ET 1



Sub-ET 2



Sub-ET 3



Sub-ET 4

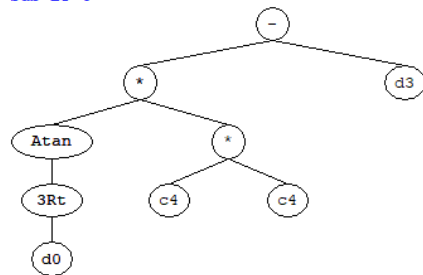


Figure 3-14. Expression trees of the developed GEP model.

### 3.5.4 Comparison of the Results of LSSVM, ANFIS, and GEP Models

As mentioned earlier, the statistical parameters including ARE, AARE%, and  $R^2$  are calculated to evaluate the performance of the deterministic models. Table 5 includes the values of the statistical parameters obtained for the developed LSSVM, ANFIS, and GEP models. It is found that among the three developed models, GEP gives the highest value of  $R^2$  when estimating induction time, while it has the highest value of AARD% and ARD%. According to Table 3-5, the GEP model has the highest run time of 18 min, whereas the run times for the LSSVM and ANFIS models are 5 and 26 s, respectively. Figure 3-15 reports that the values of  $R^2$  for the developed GEP model for training and testing steps are 0.9582 and 0.9726, respectively. The LSSVM and ANFIS models have approximately the same value of  $R^2$  for the testing and training steps. Figure 3-16 shows and compares the experimental and predicted induction times based on the three deterministic models. According to Figure 3-16, there is a better match between the experimental and induction times determined from the GEP model compared to the LSSVM and ANFIS models.

**Table 3-5.** Error analysis results for the introduced models.

Model	Dataset	Calculated Parameter				
		$R^2$	ARD%	AARD%	Max AARD%	Run Time
ANFIS	Train	0.9299	2.817	13.83	0.551	26 sec.
	Test	0.9437	2.648	14.36	0.414	
GEP	Train	0.9726	14.428	33.63	3.840	18 min
	Test	0.9582	18.925	34.93	3.841	
LSSVM	Train	0.9293	3.406	14.03	0.505	5 sec.
	Test	0.9404	3.822	14.96	0.419	

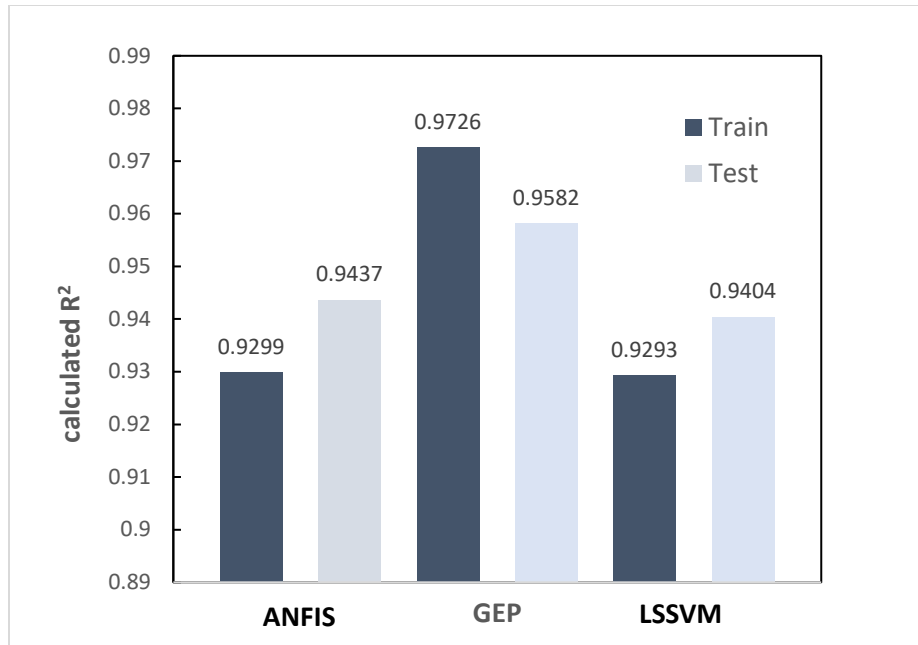


**Figure 3-15.** R<sup>2</sup> value for the developed models of ANFIS, LSSVM, and GEP.

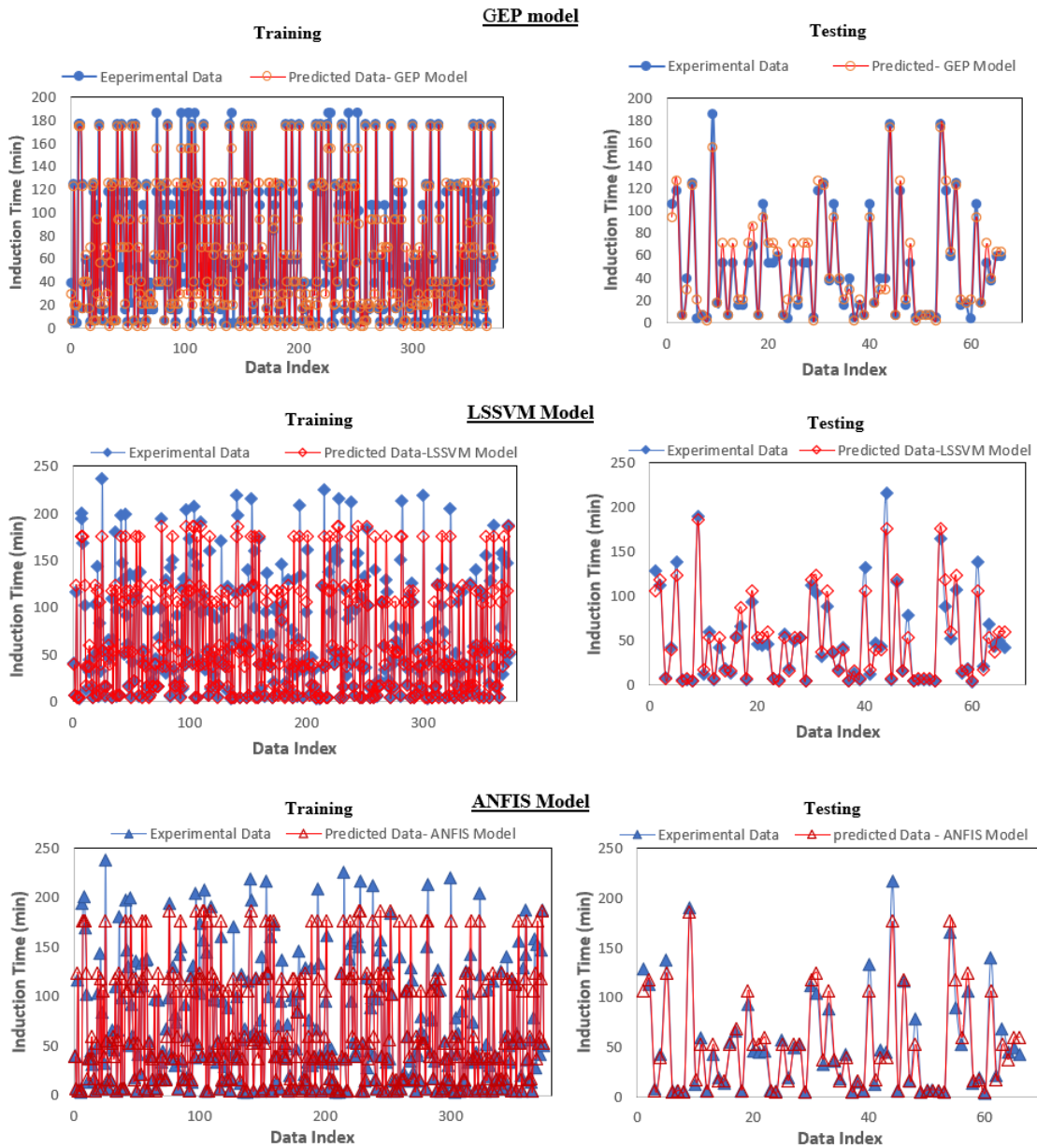


**Figure 3-16.** Comparing experimental and predicted induction times obtained from LSSVM, ANFIS, and GEP models for two phases: (a) Training, and (b) Testing.

### 3.5.5 Sensitivity Analysis of ANFIS Model

The sensitivity analysis is conducted to identify the relationships between the target (induction time) and input parameters based on the developed ANFIS model. The strength of the linear

relationship between two parameters can be determined using the correlation coefficient method [78, 115, 116]. This approach can be employed to identify which input parameters have the highest impact on the target parameter. There are different ways to calculate the correlation coefficient ( $r$ ), which determines the degree of a linear relationship [117]. The Pearson product-moment correlation is one of the best/common methods to calculate  $r$ , as defined below [78, 116]:

$$r_{x_1x_2} = \frac{\sigma_{x_1x_2}}{\sigma_{x_1}\sigma_{x_2}} \quad (3-24)$$

where  $x_1$  and  $x_2$  introduce the two parameters,  $\sigma_{x_1}$  and  $\sigma_{x_2}$  stand for the standard deviation of two parameters, and  $\sigma_{x_1x_2}$  is the covariance.  $\sigma_{x_1x_2}$  is expressed as follows:

$$\sigma_{x_1x_2} = \frac{\sum_{i=1}^N (x_1 - \bar{x}_1)(x_2 - \bar{x}_2)}{N - 1} \quad (3-25)$$

where  $N$  refers to the number of experimental data; and  $\bar{x}_1$  and  $\bar{x}_2$  denote the average of two variables  $x_1$  and  $x_2$ .

The calculated correlation coefficient has a value between [-1 +1]. If the value of  $r$  is zero, it indicates there is no linear relationship between the two parameters. Two variables may have a positive; it implies a strong linear relationship if calculated  $r$  is close to 1, whilst there is a negative strong linear relationship if  $r$  is close to -1. The results of sensitivity analysis are presented in Figure 3-17 shows the relationship between each input parameter and predicted induction time. As it is clear from Figure 3-17, the correlation coefficient calculated for pressure and temperature is high and positive. Figure 3-18 indicates the Pearson correlation coefficient calculated for the target parameter (induction time) with respect to the input parameters (molecular weight of solution ( $Mw_{sol}$ ), the mass fraction of KHI ( $m_i$ ), temperature ( $T_{exp}$ ), system pressure ( $P$ ), and subcooling ( $\Delta T$ ). According to Figure 3-18, the most important factors affecting the induction time are the system pressure and temperature with  $r$ -values of 0.751 and 0.802, respectively. However, the

induction time is negatively related to other input parameters, including the molecular weight of the solution, mass fraction of Luvicap 55 W, and subcooling as the correlation coefficients obtained for these parameters are negative with the values of -0.094, -0.094, and -0.807, respectively.

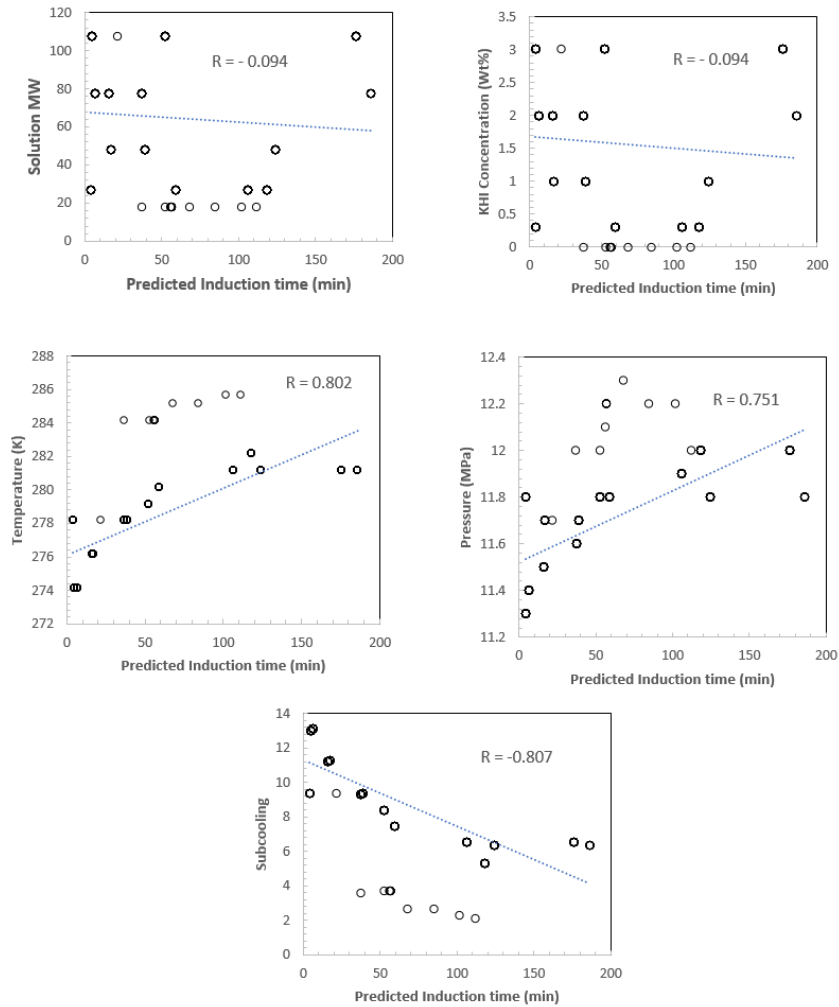


**Figure 3-17.** Pearson correlation coefficient between the induction time and input parameters, including the molecular weight of solution ( $Mw_{sol}$ ), the mass fraction of KHI ( $m_i$ ), temperature ( $T_{exp}$ ), system pressure (P), and subcooling ( $\Delta T$ ).

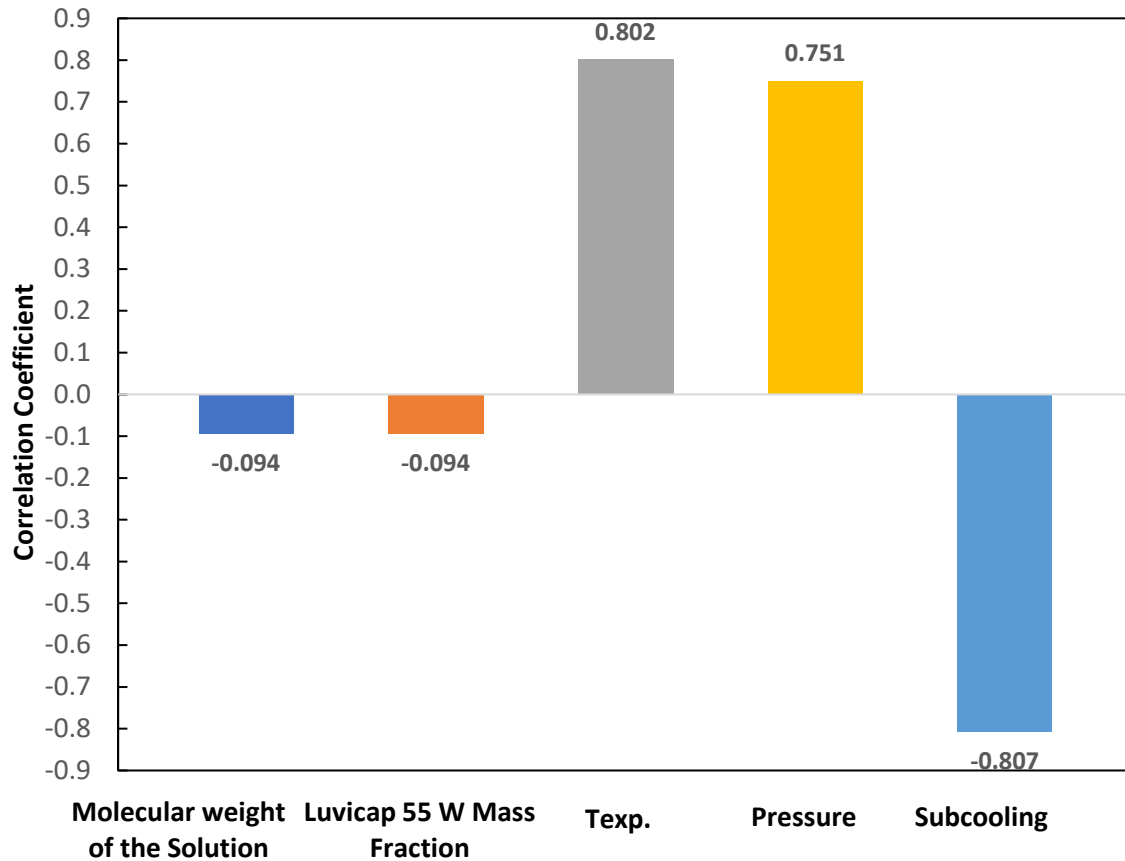


**Figure 3-18.** Correlation coefficient values for induction time with respect to input parameters.

### 3.6 CONCLUSIONS

Induction time is a critical parameter for gas hydrate formation in the presence of KHIs that exhibits the quality of KHIs. This chapter employs deterministic models to predict the induction time for methane/ Luvicap 55W/ water systems. To achieve this goal, LSSVM, ANFIS, and GEP models are introduced using 440 experimental data, where 85% of the data are utilized for the training step and 15% for the testing step. The input parameters include the molecular weight of the solution ( $Mw_{sol}$ ), mass fraction of KHI ( $m_i$ ), temperature ( $T_{exp}$ ), system pressure (P), and

subcooling ( $\Delta T$ ). ARE, AARE%, and  $R^2$  as the key statistical parameters to evaluate the performance of the deterministic models. The main conclusions drawn from this research work are given below:

1. Comparing the induction time predictions with experimental data using the LSSVM model (with radial kernel function) reveals that the introduced model is able to estimate the induction time with a good accuracy, where the  $R^2$  values for the training and testing phases are 0.929 and 0.940, respectively. For the ANFIS model, the coefficient deterministic ( $R^2$ ) values for the training and testing phases also imply that there is an acceptable match between the calculated and experimental induction time.
2. The prediction results reveal that GEP has the best predictive performance for induction time in the training and testing phases when compared with LSSVM and ANFIS models. Nevertheless, the run time of this model is much more than that of other models, with a value of 18 minutes. An excellent agreement between the experimental data and the induction time predictions is noticed.
3. The model parameters are determined through a trial and error procedure to ensure the optimized models are developed. For future work, it is recommended to use optimization tools to obtain the optimal values of the parameters.
4. According to the sensitivity analysis and calculated Pearson correlation coefficient, the most influential parameters are the system pressure and temperature. Other input parameters, such as the molecular weight of the solution, mass fraction of the Luvicap 55 W, and subcooling, have indirect relationships with the induction time. This study introduces valuable tools for predicting the induction time of methane/ Luvicap 55W

solution. The new equation developed from the GEP approach for calculating induction time can be employed by engineers and researchers in the oil and gas industry.

5. Calculation of induction time parameter for other KHIs is recommended as a future study. Furthermore, it is suggested to develop new correlations for calculating the induction time of the natural gas hydrate formation in the presence of KHIs using hybrid models.

## ACKNOWLEDGMENTS

We would like to thank Dr. May and his team from the University of Western Australia for providing the experimental data. Moreover, the financial assistance offered by Memorial University (NL, Canada), the Natural Sciences and Engineering Research Council of Canada (NSERC), Equinor Canada, and InnovateNL is greatly appreciated.

## NOMENCLATURES

---

### Acronyms

---

AAs	Anti Agglomerants
ANFIS	Adaptive Network-based Fuzzy Inference System
AARE	Average Absolute Relative Error
ANN	Artificial Neural Network
ARE	Average Relative Error
CART	Classification And Regression Tree
CSM	Colorado School of Mine
DHFT	Depression of the gas hydrate formation temperature
EG	Ethylene Glycol
ET	Expression Tree
GA	Genetic Algorithms
GP	Genetic Programming

GEP	Gene Expression Programming
HPEI-R-AO	Hyperbranched polyethyleneimine polyalkylated amine oxides
HPS-ALTA	High-Pressure Stirred Automated Lag Time Apparatus
IFP	French Petroleum Institute
KHIs	Kinetic Hydrate Inhibitors
LDHIs	Low Dose Kinetic Inhibitors
LSSVM	Least Squares Support Vector Machine
MEG	Mono Ethylene Glycol
MF	Membership function
NG	Natural Gas
NN	Neural Networks
PVCAP	Polyvinylcaprolactam
PVP	Poly(N-vinylpyrrolidone)
RBF-ANN	Radial Basis Function Artificial Neural Network
$R^2$	Coefficient of determination
SVM	Support Vector Machine
sI	structure I
sII	structure II
sH	Structure Hexagonal
TSK	Takagi–Sugeno–Kang
TEPA-R-AO	Tetraethylenepentamine polyalkylated amine oxides
THF	Tetrahydrofuran
THIs	Thermodynamic Inhibitors
VP/VC	N-vinyl pyrrolidone/N-vinyl caprolactam

---

**Variables/Letters**

$b$	Bias term
$c_j^i$	Consequence parameters
$d$	Degree of the polynomial
$f_i(x)$	Output of $i$ th rule
$e_k$	Regression error
$g(x)$	Nonlinear mapping function

$K$	Kernel function
$K_s^i$	Linguistic labels
$m_i$	Mass fraction of KHI
$Mw_{sol}$	Weight of solution
$P$	System pressure
$Q_1^i$	Output of layer
$r$	Correlation coefficient
$T$	Weight matrix.
$T_{exp}$	Temperature
$t_i$	Induction time
$\Delta T$	Subcooling
$w$	Weight vector
$w_i$	Firing strengths
$\bar{w}_i$	Normalized firing strength
$x_k$	Input data
$\hat{x}$	Normalized value of experimental data.
$x_{max}$	Maximum experimental data
$x_{min}$	Minimum experimental data
$\bar{x}_i$	Average of variables $x_1$
$y_k$	Output data

---

### Greek Letters

---

$\mu$	Regularization parameter
$\beta_k$	Lagrangian multipliers
$\sigma^2$	Kernel width
$\sigma_{x_1x_2}$	Covariance
$\mu_{K_s^i(x_s)}$	Membership function (MF)

---

### Subscripts and Superscripts

---

$k, s, i, n$	Number of data
exp	Experiment

**REFERENCES**

1. Sloan Jr, E.D. and C.A. Koh, *Clathrate hydrates of natural gases*. 2007: CRC press.
2. Gabitto, J.F. and C. Tsouris, *Physical properties of gas hydrates: A review*. Journal of Thermodynamics, 2010. **2010**.
3. Demirbas, A., *Methane gas hydrate: as a natural gas source*. 2010: Springer.
4. Sloan, E.D., *Gas hydrates: review of physical/chemical properties*. Energy & fuels, 1998. **12**(2): p. 191-196.
5. Hammerschmidt, E., *Formation of gas hydrates in natural gas transmission lines*. Industrial & Engineering Chemistry, 1934. **26**(8): p. 851-855.
6. Edmonds, B., T. Moorwood, R. Szczepanski, and X. Zhang, *Simulating wax deposition in pipelines for flow assurance*. Energy & Fuels, 2008. **22**(2): p. 729-741.
7. Hilbert, J. *Flow assurance: Wax deposition and gelling in subsea oil pipelines*. in *SPE Asia Pacific Oil and Gas Conference and Exhibition*. 2010. OnePetro.
8. Hammami, A. and J. Ratulowski, *Precipitation and deposition of asphaltenes in production systems: a flow assurance overview*, in *Asphaltenes, heavy oils, and petroleomics*. 2007, Springer. p. 617-660.
9. Jordan, M., K. Sjuraether, I. Collins, N. Feasey, and D. Emmons. *Life cycle management of scale control within subsea fields and its impact on flow assurance, Gulf of Mexico and the North Sea basin*. in *SPE Annual Technical Conference and Exhibition*. 2001. OnePetro.
10. Sloan, E., C. Koh, A. Sum, A. Ballard, G. Shoup, N. McMullen, J. Creek, and T. Palermo, *Hydrates: state of the art inside and outside flowlines*. Journal of petroleum technology, 2009. **61**(12): p. 89-94.

11. Gbaruko, B., J. Igwe, P. Gbaruko, and R. Nwokeoma, *Gas hydrates and clathrates: Flow assurance, environmental and economic perspectives and the Nigerian liquified natural gas project*. Journal of Petroleum Science and Engineering, 2007. **56**(1-3): p. 192-198.
12. Hatscher, S. and L. Ugueto. *A New Flow Assurance Strategy for the Vega Asset: Managing Hydrate and Integrity Risks on a Long Multiphase Flowline of a Norwegian Subsea Asset*. in *SPE Offshore Europe Conference and Exhibition*. 2019. OnePetro.
13. Delavar, H. and A. Haghtalab, *Thermodynamic modeling of gas hydrate formation conditions in the presence of organic inhibitors, salts and their mixtures using UNIQUAC model*. Fluid Phase Equilibria, 2015. **394**: p. 101-117.
14. Zhao, X., Z. Qiu, G. Zhou, and W. Huang, *Synergism of thermodynamic hydrate inhibitors on the performance of poly (vinyl pyrrolidone) in deepwater drilling fluid*. Journal of Natural Gas Science and Engineering, 2015. **23**: p. 47-54.
15. Kim, J., H. Kim, Y. hoon Sohn, D. Chang, Y. Seo, and S.-P. Kang, *Prevention of methane hydrate re-formation in transport pipeline using thermodynamic and kinetic hydrate inhibitors*. Journal of Petroleum Science and Engineering, 2017. **154**: p. 114-125.
16. Cha, M., K. Shin, J. Kim, D. Chang, Y. Seo, H. Lee, and S.-P. Kang, *Thermodynamic and kinetic hydrate inhibition performance of aqueous ethylene glycol solutions for natural gas*. Chemical Engineering Science, 2013. **99**: p. 184-190.
17. Morales, N.L., J. Anthony, J.F. Garming, R.A. Trompert, G.J. de Vries, and P.A. Webber. *A Mature Southern North Sea Asset Considers Conversion to Wet Gas Operation Which Requires the Development of Compatible and Novel Chemistries for Flow-Assurance and Asset Integrity*. in *Offshore Technology Conference*. 2013. OnePetro.

18. Norland, A.K. and M.A. Kelland, *Crystal growth inhibition of tetrahydrofuran hydrate with bis-and polyquaternary ammonium salts*. *Chemical engineering science*, 2012. **69**(1): p. 483-491.
19. Makwashi, N., D. Zhao, T. Ismaila, and I. Paiko. *Pipeline Gas Hydrate Formation and Treatment: A Review*. in *3rd National Engineering Conference on Building the Gap between Academia and Industry, Faculty of Engineering, Bayero University, Kano*. 2018.
20. Kelland, M.A., *History of the development of low dosage hydrate inhibitors*. *Energy & fuels*, 2006. **20**(3): p. 825-847.
21. Sugier, A., P. Bourgmayer, E. Behar, and E. Freund, *Process for transporting a fluid which forms hydrates*. European Patent Application, 1989. **323307**.
22. Sloan, E., *Patent 5,420,370*. 1995, May.
23. Singh, A. and A. Suri, *A review on gas hydrates and kinetic hydrate inhibitors based on acrylamides*. *Journal of Natural Gas Science and Engineering*, 2020: p. 103539.
24. Kelland, M.A., T.M. Svartaas, J. Øvsthus, and T. Namba, *A new class of kinetic hydrate inhibitor*. *Annals of the New York Academy of Sciences*, 2000. **912**(1): p. 281-293.
25. Lederhos, J., J. Long, A. Sum, R. Christiansen, and E. Sloan Jr, *Effective kinetic inhibitors for natural gas hydrates*. *Chemical Engineering Science*, 1996. **51**(8): p. 1221-1229.
26. Saberi, A., A. Alamdari, A. Rasoolzadeh, and A.H. Mohammadi, *Insights into kinetic inhibition effects of MEG, PVP, and L-tyrosine aqueous solutions on natural gas hydrate formation*. *Petroleum Science*, 2021. **18**(2): p. 495-508.
27. Long, Z., Z. Lu, Q. Ding, X. Zhou, J. Lei, and D. Liang, *Evaluation of Kinetic Inhibition of Methane Hydrate Formation by a Copolymer of N-Vinylcaprolactam with 1-Vinylimidazole*. *Energy & Fuels*, 2019. **33**(10): p. 10133-10142.

28. Lee, J.D. and P. Englezos, *Enhancement of the performance of gas hydrate kinetic inhibitors with polyethylene oxide*. Chemical engineering science, 2005. **60**(19): p. 5323-5330.
29. Arjmandi, M., B. Tohidi, A. Danesh, and A.C. Todd, *Is subcooling the right driving force for testing low-dosage hydrate inhibitors?* Chemical engineering science, 2005. **60**(5): p. 1313-1321.
30. Zhang, Q. and M.A. Kelland, *Kinetic inhibition performance of alkylated polyamine oxides on structure I methane hydrate*. Chemical Engineering Science, 2020. **220**: p. 115652.
31. Talaghat, M.R., *Experimental investigation of induction time for binary mixtures during gas hydrate formation in the simultaneous presence of the PVP and L-Tyrosine as kinetic inhibitors in a flow mini-loop apparatus*. Journal of Chemical and Petroleum Engineering, 2011. **45**(2): p. 153-166.
32. Lee, J.D. and P. Englezos, *Unusual kinetic inhibitor effects on gas hydrate formation*. Chemical engineering science, 2006. **61**(5): p. 1368-1376.
33. Lim, V.W., P.J. Metaxas, M.L. Johns, G. Haandrikman, D. Crosby, Z.M. Aman, and E.F. May, *The delay of gas hydrate formation by kinetic inhibitors*. Chemical Engineering Journal, 2021. **411**: p. 128478.
34. Khatinzadeh, G., S. Taghipoor, A. Mehdizadeh, and A. Roozbehani, *Synergistic Effect of Glycol Ethers with a Kinetic Inhibitor (Poly (VP-VCap)) for Sweet Natural Gas Hydrate Formation:(Concentration Effect of Glycol Ethers)*. Journal of Petroleum Science and Technology, 2019. **9**(2): p. 46-53.

35. Haghtalab, A., M. Zare, A. Ahmadi, and K. Nazari, *Prediction of hydrate equilibrium conditions using electrolyte cubic square-well equation of state*. Fluid phase equilibria, 2012. **333**: p. 74-86.
36. Zare, M., A. Haghtalab, A.N. Ahmadi, and K. Nazari, *Experiment and thermodynamic modeling of methane hydrate equilibria in the presence of aqueous imidazolium-based ionic liquid solutions using electrolyte cubic square well equation of state*. Fluid Phase Equilibria, 2013. **341**: p. 61-69.
37. Zare, M., J. Kondori, S. Zendejboudi, and F. Khan, *PC-SAFT/UNIQUAC model assesses formation condition of methane hydrate in the presence of imidazolium-based ionic liquid systems*. Fuel, 2020. **266**: p. 116757.
38. Kondori, J., S. Zendejboudi, and L. James, *Evaluation of gas hydrate formation temperature for gas/water/salt/alcohol systems: utilization of extended UNIQUAC model and PC-SAFT equation of state*. Industrial & Engineering Chemistry Research, 2018. **57**(41): p. 13833-13855.
39. Dehaghani, A.H.S. and M.H. Badizad, *Thermodynamic modeling of gas hydrate formation in presence of thermodynamic inhibitors with a new association equation of state*. Fluid Phase Equilibria, 2016. **427**: p. 328-339.
40. Avula, V.R., P. Gupta, R.L. Gardas, and J.S. Sangwai, *Thermodynamic modeling of phase equilibrium of carbon dioxide clathrate hydrate in aqueous solutions of promoters and inhibitors suitable for gas separation*. Asia-Pacific Journal of Chemical Engineering, 2017. **12**(5): p. 709-722.

41. Deka, B., A. Barifcani, A. Al Helal, D. Badi, V. Mahto, and H. Vuthaluru, *Generation of methane gas hydrate equilibrium curve for the thermodynamic gas hydrate inhibitor propylene glycol*. Journal of Petroleum Science and Engineering, 2021. **199**: p. 108312.
42. Bharathi, A., O. Nashed, B. Lal, and K.S. Foo, *Experimental and modeling studies on enhancing the thermodynamic hydrate inhibition performance of monoethylene glycol via synergistic green material*. Scientific reports, 2021. **11**(1): p. 1-10.
43. Li, S., J. Wang, X. Lv, K. Ge, Z. Jiang, and Y. Li, *Experimental measurement and thermodynamic modeling of methane hydrate phase equilibria in the presence of chloride salts*. Chemical Engineering Journal, 2020. **395**: p. 125126.
44. Turner, D., J. Boxall, S. Yang, D. Kleehammer, C. Koh, K. Miller, E. Sloan, Z. Xu, P. Matthews, and L. Talley. *Development of a hydrate kinetic model and its incorporation into the OLGA2000® transient multiphase flow simulator*. in *Proceedings of the 5th international conference on gas hydrates, Trondheim, Norway*. 2005.
45. Vysniauskas, A. and P. Bishnoi, *Kinetics of ethane hydrate formation*. Chemical Engineering Science, 1985. **40**(2): p. 299-303.
46. Shi, B.-H., J. Gong, C.-Y. Sun, J.-K. Zhao, Y. Ding, and G.-J. Chen, *An inward and outward natural gas hydrates growth shell model considering intrinsic kinetics, mass and heat transfer*. Chemical engineering journal, 2011. **171**(3): p. 1308-1316.
47. Mu, L., S. Li, Q.-L. Ma, K. Zhang, C.-Y. Sun, G.-J. Chen, B. Liu, and L.-Y. Yang, *Experimental and modeling investigation of kinetics of methane gas hydrate formation in water-in-oil emulsion*. Fluid Phase Equilibria, 2014. **362**: p. 28-34.
48. Kashchiev, D. and A. Firoozabadi, *Induction time in crystallization of gas hydrates*. Journal of crystal growth, 2003. **250**(3-4): p. 499-515.

49. Skovborg, P. and P. Rasmussen, *A mass transport limited model for the growth of methane and ethane gas hydrates*. Chemical Engineering Science, 1994. **49**(8): p. 1131-1143.
50. Vysniauskas, A. and P. Bishnoi, *A kinetic study of methane hydrate formation*. Chemical Engineering Science, 1983. **38**(7): p. 1061-1072.
51. Natarajan, V., P. Bishnoi, and N. Kalogerakis, *Induction phenomena in gas hydrate nucleation*. Chemical Engineering Science, 1994. **49**(13): p. 2075-2087.
52. Rasoolzadeh, A., J. Javanmardi, A. Eslamimanesh, and A.H. Mohammadi, *Experimental study and modeling of methane hydrate formation induction time in the presence of ionic liquids*. Journal of Molecular Liquids, 2016. **221**: p. 149-155.
53. Talaghat, M.R. and A.R. Khodaverdilo, *Study of different models of prediction of the simple gas hydrates formation induction time and effect of different equations of state on them*. Heat and Mass Transfer, 2019. **55**(5): p. 1245-1255.
54. Ghiasi, M.M., A.H. Mohammadi, and S. Zendehboudi, *Use of hybrid-ANFIS and ensemble methods to calculate minimum miscibility pressure of CO<sub>2</sub>-reservoir oil system in miscible flooding process*. Journal of Molecular Liquids, 2021. **331**: p. 115369.
55. Ghiasi, M.M. and S. Zendehboudi, *Application of decision tree-based ensemble learning in the classification of breast cancer*. Computers in Biology and Medicine, 2021. **128**: p. 104089.
56. Ghiasi, M.M., A.H. Mohammadi, and S. Zendehboudi, *Modeling stability conditions of methane Clathrate hydrate in ionic liquid aqueous solutions*. Journal of Molecular Liquids, 2021. **325**: p. 114804.

57. Kondori, J., M.I. Miah, S. Zendehboudi, F. Khan, and D. Heagle, *Hybrid connectionist models to assess recovery performance of low salinity water injection*. Journal of Petroleum Science and Engineering, 2021. **197**: p. 107833.
58. Ghiasi, M.M., S. Zendehboudi, and A.A. Mohsenipour, *Decision tree-based diagnosis of coronary artery disease: CART model*. Computer methods and programs in biomedicine, 2020. **192**: p. 105400.
59. Seyyedattar, M., M.M. Ghiasi, S. Zendehboudi, and S. Butt, *Determination of bubble point pressure and oil formation volume factor: Extra trees compared with LSSVM-CSA hybrid and ANFIS models*. Fuel, 2020. **269**: p. 116834.
60. Esene, C., S. Zendehboudi, H. Shiri, and A. Aborig, *Deterministic tools to predict recovery performance of carbonated water injection*. Journal of Molecular Liquids, 2020. **301**: p. 111911.
61. Hamed, H., M. Ehteshami, S.A. Mirbagheri, and S. Zendehboudi, *New deterministic tools to systematically investigate fouling occurrence in membrane bioreactors*. Chemical Engineering Research and Design, 2019. **144**: p. 334-353.
62. Sinehbaghizadeh, S., A. Roosta, N. Rezaei, M.M. Ghiasi, J. Javanmardi, and S. Zendehboudi, *Evaluation of phase equilibrium conditions of clathrate hydrates using connectionist modeling strategies*. Fuel, 2019. **255**: p. 115649.
63. Ghiasi, M.M., A. Bahadori, and S. Zendehboudi, *Estimation of triethylene glycol (TEG) purity in natural gas dehydration units using fuzzy neural network*. Journal of Natural Gas Science and Engineering, 2014. **17**: p. 26-32.

64. Ghiasi, M.M. and A.H. Mohammadi, *Rigorous modeling of CO<sub>2</sub> equilibrium absorption in MEA, DEA, and TEA aqueous solutions*. Journal of Natural Gas Science and Engineering, 2014. **18**: p. 39-46.
65. Landgrebe, M.K. and D. Nkazi, *Toward a Robust, Universal Predictor of Gas Hydrate Equilibria by Means of a Deep Learning Regression*. ACS omega, 2019. **4**(27): p. 22399-22417.
66. Mesbah, M., S. Habibnia, S. Ahmadi, A.H.S. Dehaghani, and S. Bayat, *Developing a robust correlation for prediction of sweet and sour gas hydrate formation temperature*. Petroleum, 2020.
67. ZareNezhad, B. and A. Aminian, *Accurate prediction of sour gas hydrate equilibrium dissociation conditions by using an adaptive neuro fuzzy inference system*. Energy conversion and management, 2012. **57**: p. 143-147.
68. Chamkalani, A., S. Zendehboudi, A. Bahadori, R. Kharrat, R. Chamkalani, L. James, and I. Chatzis, *Integration of LSSVM technique with PSO to determine asphaltene deposition*. Journal of Petroleum Science and Engineering, 2014. **124**: p. 243-253.
69. Yarveicy, H. and M.M. Ghiasi, *Modeling of gas hydrate phase equilibria: Extremely randomized trees and LSSVM approaches*. Journal of Molecular Liquids, 2017. **243**: p. 533-541.
70. Kamari, A., A. Bahadori, A.H. Mohammadi, and S. Zendehboudi, *New tools predict monoethylene glycol injection rate for natural gas hydrate inhibition*. Journal of Loss Prevention in the Process Industries, 2015. **33**: p. 222-231.

71. Qin, H., V. Srivastava, H. Wang, L.E. Zerpa, and C.A. Koh. *Machine Learning Models to Predict Gas Hydrate Plugging Risks Using Flowloop and Field Data*. in *Offshore Technology Conference*. 2019. OnePetro.
72. Yarveicy, H., M.M. Ghiasi, and A.H. Mohammadi, *Determination of the gas hydrate formation limits to isenthalpic Joule–Thomson expansions*. *Chemical Engineering Research and Design*, 2018. **132**: p. 208-214.
73. Mehrizadeh, M., *Prediction of gas hydrate formation using empirical equations and data-driven models*. *Materials Today: Proceedings*, 2021. **42**: p. 1592-1598.
74. Rostami, A. and A. Shokrollahi, *Accurate prediction of water dewpoint temperature in natural gas dehydrators using gene expression programming approach*. *Journal of Molecular Liquids*, 2017. **243**: p. 196-204.
75. Roy, S., A. Ghosh, A.K. Das, and R. Banerjee, *A comparative study of GEP and an ANN strategy to model engine performance and emission characteristics of a CRDI assisted single cylinder diesel engine under CNG dual-fuel operation*. *Journal of natural gas science and engineering*, 2014. **21**: p. 814-828.
76. Amar, M.N., A. Larestani, Q. Lv, T. Zhou, and A. Hemmati-Sarapardeh, *Modeling of methane adsorption capacity in shale gas formations using white-box supervised machine learning techniques*. *Journal of Petroleum Science and Engineering*, 2021: p. 109226.
77. Amar, M.N., *Prediction of hydrate formation temperature using gene expression programming*. *Journal of Natural Gas Science and Engineering*, 2021. **89**: p. 103879.
78. Pelalak, R., A.T. Nakhjiri, A. Marjani, M. Rezakazemi, and S. Shirazian, *Influence of machine learning membership functions and degree of membership function on each input parameter for simulation of reactors*. *Scientific Reports*, 2021. **11**(1): p. 1-11.

79. Yarveicy, H., M.M. Ghiasi, and A.H. Mohammadi, *Performance evaluation of the machine learning approaches in modeling of CO<sub>2</sub> equilibrium absorption in Piperazine aqueous solution*. Journal of Molecular Liquids, 2018. **255**: p. 375-383.
80. Amedi, H.R., A. Baghban, and M.A. Ahmadi, *Evolving machine learning models to predict hydrogen sulfide solubility in the presence of various ionic liquids*. Journal of Molecular Liquids, 2016. **216**: p. 411-422.
81. Mahmoud, A.A., S. Elkatatny, and A. Al-AbdulJabbar, *Application of machine learning models for real-time prediction of the formation lithology and tops from the drilling parameters*. Journal of Petroleum Science and Engineering, 2021. **203**: p. 108574.
82. Baghban, A., M. Kahani, M.A. Nazari, M.H. Ahmadi, and W.-M. Yan, *Sensitivity analysis and application of machine learning methods to predict the heat transfer performance of CNT/water nanofluid flows through coils*. International Journal of Heat and Mass Transfer, 2019. **128**: p. 825-835.
83. Khan, M.R., S. Alnuaim, Z. Tariq, and A. Abdulraheem. *Machine learning application for oil rate prediction in artificial gas lift wells*. in *SPE Middle East Oil and Gas Show and Conference*. 2019. OnePetro.
84. AlRassas, A.M., M.A. Al-qaness, A.A. Ewees, S. Ren, M. Abd Elaziz, R. Damaševičius, and T. Krilavičius, *Optimized ANFIS Model Using Aquila Optimizer for Oil Production Forecasting*. Processes, 2021. **9**(7): p. 1194.
85. Pandey, R.K., A.K. Dahiya, and A. Mandal, *Identifying Applications of Machine Learning and Data Analytics Based Approaches for Optimization of Upstream Petroleum Operations*. Energy Technology, 2021. **9**(1): p. 2000749.

86. Vapnik, V., S.E. Golowich, and A. Smola, *Support vector method for function approximation, regression estimation, and signal processing*. Advances in neural information processing systems, 1997: p. 281-287.
87. Vapnik, V., *The nature of statistical learning theory*. 2013: Springer science & business media.
88. Tavakoli, H., A. Khoshkaram, A. Baghban, and M. Baghban, *Modelling of methane hydrate formation pressure in the presence of different inhibitors*. Petroleum Science and Technology, 2017. **35**(1): p. 92-98.
89. Rashid, S., A. Fayazi, B. Harimi, E. Hamidpour, and S. Younesi, *Evolving a robust approach for accurate prediction of methane hydrate formation temperature in the presence of salt inhibitor*. Journal of Natural Gas Science and Engineering, 2014. **18**: p. 194-204.
90. Wang, H. and D. Hu. *Comparison of SVM and LS-SVM for regression*. in *2005 International Conference on Neural Networks and Brain*. 2005. IEEE.
91. Suykens, J.A. and J. Vandewalle, *Least squares support vector machine classifiers*. Neural processing letters, 1999. **9**(3): p. 293-300.
92. Suykens, J.A., J. De Brabanter, L. Lukas, and J. Vandewalle, *Weighted least squares support vector machines: robustness and sparse approximation*. Neurocomputing, 2002. **48**(1-4): p. 85-105.
93. Muller, K.-R., S. Mika, G. Ratsch, K. Tsuda, and B. Scholkopf, *An introduction to kernel-based learning algorithms*. IEEE transactions on neural networks, 2001. **12**(2): p. 181-201.
94. Gunn, S.R., *Support vector machines for classification and regression*. ISIS technical report, 1998. **14**(1): p. 5-16.

95. Mesbah, M., E. Soroush, and M. Rezakazemi, *Development of a least squares support vector machine model for prediction of natural gas hydrate formation temperature*. Chinese journal of chemical engineering, 2017. **25**(9): p. 1238-1248.
96. Shabri, A. and Suhartono, *Streamflow forecasting using least-squares support vector machines*. Hydrological Sciences Journal, 2012. **57**(7): p. 1275-1293.
97. Jang, J.-S., *ANFIS: adaptive-network-based fuzzy inference system*. IEEE transactions on systems, man, and cybernetics, 1993. **23**(3): p. 665-685.
98. Ghiasi, M.M., M. Arabloo, A.H. Mohammadi, and T. Barghi, *Application of ANFIS soft computing technique in modeling the CO<sub>2</sub> capture with MEA, DEA, and TEA aqueous solutions*. International Journal of Greenhouse Gas Control, 2016. **49**: p. 47-54.
99. Heidari, E. and S. Ghoreishi, *Prediction of supercritical extraction recovery of EGCG using hybrid of Adaptive Neuro-Fuzzy Inference System and mathematical model*. The Journal of Supercritical Fluids, 2013. **82**: p. 158-167.
100. Ferreira, C., *Gene expression programming: a new adaptive algorithm for solving problems*. arXiv preprint cs/0102027, 2001.
101. Onen, F. and T. Bagatur, *Prediction of Flood Frequency Factor for Gumbel Distribution Using Regression and GEP Model*. Arabian Journal for Science & Engineering (Springer Science & Business Media BV), 2017. **42**(9).
102. Mohammed, A.Y. and A. Sharifi, *Gene Expression Programming (GEP) to predict coefficient of discharge for oblique side weir*. Applied Water Science, 2020. **10**(6): p. 1-9.
103. Ashrafian, A., A.H. Gandomi, M. Rezaie-Balf, and M. Emadi, *An evolutionary approach to formulate the compressive strength of roller compacted concrete pavement*. Measurement, 2020. **152**: p. 107309.

104. Talaghat, M.R., *Prediction of induction time for natural gas components during gas hydrate formation in the presence of kinetic hydrate inhibitors in a flow mini-loop apparatus*. The Canadian Journal of Chemical Engineering, 2013. **91**(4): p. 790-797.
105. Huot, K., M. White, and T. Acharya, *Natural Gas Hydrates: A Review of Formation, and Prevention/Mitigation in Subsea Pipelines*. Advanced Science, Engineering and Medicine, 2019. **11**(6): p. 453-464.
106. Yaqub, S., A. bin Mohd Shariff, and N.B. Mellon, *Unraveling the effect of sub-cooling temperatures on the kinetic performance of biopolymers for methane hydrate*. Journal of Natural Gas Science and Engineering, 2019. **65**: p. 68-81.
107. Zhang, Q., X. Shen, X. Zhou, and D. Liang, *Inhibition effect study of carboxyl-terminated polyvinyl caprolactam on methane hydrate formation*. Energy & Fuels, 2017. **31**(1): p. 839-846.
108. Zare, M., A. Haghtalab, A.N. Ahmadi, K. Nazari, and A. Mehdizadeh, *Effect of imidazolium based ionic liquids and ethylene glycol monoethyl ether solutions on the kinetic of methane hydrate formation*. Journal of Molecular Liquids, 2015. **204**: p. 236-242.
109. Zhao, X., Z. Qiu, and W. Huang, *Characterization of kinetics of hydrate formation in the presence of kinetic hydrate inhibitors during deepwater drilling*. Journal of Natural Gas Science and Engineering, 2015. **22**: p. 270-278.
110. Duchateau, C., J.-L. Peytavy, P. Glénat, T.-E. Pou, M. Hidalgo, and C. Dicharry, *Laboratory evaluation of kinetic hydrate inhibitors: a procedure for enhancing the repeatability of test results*. Energy & Fuels, 2009. **23**(2): p. 962-966.

111. Ke, W. and D. Chen, *A short review on natural gas hydrate, kinetic hydrate inhibitors and inhibitor synergists*. Chinese Journal of Chemical Engineering, 2019. **27**(9): p. 2049-2061.
112. Saghafi, H. and H. Yarveicy, *Gas hydrate stability conditions: modeling on the basis of gas gravity approach*. Petroleum Science and Technology, 2019.
113. Landgrebe, M.K.B., *Towards a robust, universal predictor of gas hydrate equilibria through the means of a deep learning regression*. 2019.
114. Bian, X.-Q., B. Han, Z.-M. Du, J.-N. Jaubert, and M.-J. Li, *Integrating support vector regression with genetic algorithm for CO<sub>2</sub>-oil minimum miscibility pressure (MMP) in pure and impure CO<sub>2</sub> streams*. Fuel, 2016. **182**: p. 550-557.
115. Vaferi, B., F. Samimi, E. Pakgozar, and D. Mowla, *Artificial neural network approach for prediction of thermal behavior of nanofluids flowing through circular tubes*. Powder technology, 2014. **267**: p. 1-10.
116. Lee Rodgers, J. and W.A. Nicewander, *Thirteen ways to look at the correlation coefficient*. The American Statistician, 1988. **42**(1): p. 59-66.

## **4. CHAPTER FOUR**

### **Computational Fluid Dynamics Approach to Study Methane Hydrate Formation in Stirred Reactor**

#### **Preface**

Marziyeh Zare, Vandad Talimi, Sohrab Zendeboudi, and Majid Abedinzadegan Abdi are the authors of this paper. This manuscript was prepared by the first author (Marziyeh Zare) with the cooperation of co-authors. The first author conducted the literature review, methodology, simulations, and results analysis. The first author addressed comments given by Vandad Talimi to improve the results and discussion. This paper was revised by Marziyeh Zare and co-authors. The feedback from co-authors, Vandad Talimi, Sohrab Zendeboudi, Majid Abedinzadegan Abdi, and journal reviewers were applied by the first author. Co-authors supervised the first author over the project and edited the manuscript.

## ABSTRACT

Prevention of hydrate blockages in oil and gas facilities requires considerable efforts and budgets. Management of hydrate formation in petroleum production and transportation components needs a detailed understanding of the dynamics and kinetics of hydrate formation phenomena. This research examines the hydrate formation in the stirred reactor for the water-methane system using the Eulerian multiphase flow model by employing a computational fluid dynamics (CFD) software (STAR CCM+). The developed numerical model incorporates the conservation equations of momentum, mass, and energy, where the hydrate equations, including mass transfer, hydrate kinetics, and heat of hydrate formation, are included in the governing equations. In this paper, the methane hydrate formation in the stirred reactor for the stirring rate of 300 RPM and volume fraction of 0.04 with a pressure of 5,500 kPa is simulated. Then, the simulation results are validated using the experimental data collected from the literature, resulting in an overall absolute average deviation percentage (AAD% of 15.6%). The influences of stirring rate, methane volume fraction, pressure, and subcooling are studied on the hydrate formation in the agitated reactor. The results reveal that the developed CFD model can predict the methane hydrate formation in the stirred reactor with acceptable precision. According to the simulation runs, methane hydrate is formed mainly near the walls and around the stirrer blades. In addition, an increase in subcooling, gas volume fraction, pressure, and stirring rate leads to more hydrate formation in the reactor with a constant temperature of 274.3 K. The proposed CFD model can be helpful for engineers and researchers in the petroleum industry to simulate hydrate formation in other complicated geometries in oil and gas facilities.

**Keywords:** Computational fluid dynamics; Methane hydrate; Sensitivity analysis; Flow assurance; Stirred reactor;

## 4.1 INTRODUCTION

Gas hydrates are crystalline compounds that occur when gas molecules as guests trap in the water cage-like structures as hosts [1, 2]. Gas hydrates are normally composed of water and gas molecules such as methane, ethane, propane, isobutane, normal butane, nitrogen, carbon dioxide, and hydrogen sulfide; natural gas hydrates may pose a threat to oil and gas operation [1]. The type of gas hydrate structure depends on the natural gas components. There are three structures of gas hydrates, including structure I, structure II and structure H, with various sizes and shapes. Generally, two structures of I and II have been found in oil and gas pipelines. Methane, ethane, and carbon dioxide usually form a cubic structure I, and other gases such as propane and isobutane create structure II [3, 4]. Oil and gas production systems with low temperature and high-pressure conditions might experience gas hydrate formation. Gas hydrate may not be a big issue during a normal operation, while it can cause various challenges in transient operations such as shut down and start-up, where the operating conditions have a tendency toward a lower temperature and higher pressure [5].

Some of the major problems reported by several energy companies are flow assurance challenges which need significant efforts and costs to avoid hydrate blockages in the oil and gas facilities. Under favourable conditions, gas hydrate can form rapidly, relative to waxes, scales, or asphaltenes, and without warning, in offshore pipelines. Although the hydrate plug formation rate is fast, the remediation process may take days or months [6]. Industry traditionally applied the preventing approach in gas hydrate formation scenarios by injecting thermodynamic inhibitors (methanol or monoethylene glycol) [7]. Due to economic considerations, the oil and gas companies desire to switch the hydrate avoidance policy to hydrate management [7-9]. Hydrate management strategy is a method where gas hydrates are allowed to form in the pipelines without

agglomerations and blockages. This method assists the industry to deal with hydrate formation in the pipelines, reducing the cost and amount of chemicals used in their operation [7]. One of the methods where switching from hydrate prevention to hydrate management strategy could be accomplished is using low-dosage hydrate inhibitors (LDHIs). These chemicals are generally divided into kinetic hydrate inhibitors (KHIs) and anti-agglomerate chemicals (AAs); they could postpone the hydrate formation rate and/or limit the total growth of hydrates in pipelines [10].

The hydrate management approach requires an adequate understanding of how hydrates form, accumulate, deposit, and jam in the pipes [7]. Therefore, researchers have been working on the gas hydrate behaviours and kinetics for several decades where different pieces of apparatus such as stirrer reactors and flow loops, and modeling/simulation tools are used [11-18]. Herri et al. (1999) studied the particle size distribution of methane hydrate crystals in the presence of kinetic inhibitors (A, B, and C) in a high-pressure reactor. They investigated the effect of additives on the induction time delay and the quantity of formed hydrate. The results indicated that the additives lead to increasing induction time and decreasing the amount of hydrate crystals [14]. The effect of induction time on the gas consumption rates of methane and carbon dioxide hydrates was investigated in the reactor with a 600 mL capacity made from 316 stainless steel and a pressure rating of 20 MPa. According to the results, the gas consumption rate of carbon dioxide hydrate decreases when induction time increases. In other words, a shorter induction time means there is a higher driving force in the reactor. However, the behavior of methane hydrate consumption rate with induction time is not similar to the carbon dioxide hydrate case [19]. The ethane hydrate formation and decomposition were investigated in a batch stirring reactor at a temperature range of 270–280 K, a pressure range of 883–1,667 kPa, and at various stirring rates of 110–190 rpm. They found that the hydrate formation rate was dependent on the stirring rate directly so that higher

hydrate formation was observed at a faster stirring rate. However, hydrate formation kinetics is related to pressure, temperature, degree of subcooling, and stirring rate [20]. Meindinyo and Svartaas (2016) studied the impacts of temperature, initial water content, stirring rate, and reactor size on the methane hydrate formation in the stirred semi-batch autoclave reactor at a pressure of 9,000 kPa [11]. The results revealed that subcooling had a significant influence on methane hydrate formation since increasing subcooling leads to an increase in the driving force for methane hydrate formation and growth. Also, the hydrate formation in batch/semi-batch reactor is considerably controlled by mass and heat transfer. In other words, the hydrate growth rate increases with increasing stirring rates, and then it remains unchanged at a specific stirring rate. Their research also showed a decrease in hydrate growth upon a up scale of the reactor size from 141.4 mL to 318.1 mL [11]. Methane hydrate growth kinetics was investigated theoretically and experimentally in the stirred laboratory cell, where heat transfer was the controlling mechanism for hydrate formation [12]. The effects of type and numbers of impellers on the methane hydrate formation in a stirred tank reactor with a volume of 5.71 L were studied. According to the results, methane hydrate formation rates in the experiments with Rushton turbine (RT) impeller for all baffles were higher than that of pitched blade turbines upward pumping (PBTU) experiments, while RT blades consumed more energy. The results of experiments with dual impellers were the same as single impellers tests [21]. Daraboina et al. (2011) investigated the hydrate inhibition and decomposition of the gas mixture (methane, ethane, and propane) in the presence of two commercial kinetic inhibitors (PVP and H1W85281) and two antifreeze proteins (AFP-I and AFP-III) in a stirred reactor with a volume of 58 cm<sup>3</sup> (i.d. = 3.00 cm, height = 7.07 cm). According to their results, H1W85281 was the best kinetic inhibitor with the longest induction time and slowest growth rate than other chemicals, while the fastest growth rate was obtained for PVP. However, AFP-I was

more efficient than PVP and AFP-III in terms of induction time and growth rate. Moreover, the hydrate decomposed completely in the presence of inhibitors and antifreeze [22]. CuiPing et al. (2010) utilized a 1.072-L reactor with a pressure of about 8 MPa and a temperature of 4°C to investigate the hydrate formation of methane, ethane, and propane gas mixture in the presence of low dosage hydrate inhibitors (PVP and GHI1). Their results showed that GHI1 and PVP are strong kinetic inhibitors that inhibit hydrate growth, not nucleation [23]. Four amino acids (valine, threonine, asparagine, and phenylalanine) as gas hydrate inhibitors were tested in the high pressure stirred reactor using the isochoric method at the temperature and pressure ranges of 275.71 to 286.10 K and 3.52 to 10.25 MPa, respectively. The results showed that the performance of all amino acids is similar to the thermodynamic inhibitors. Valine had the best inhibition effect among these inhibitors, with an average temperature depression of 0.529 K at 5 wt% [16]. Ahmadpanah et al. (2022) studied the natural gas hydrate kinetics in a stirred reactor under different pressures (6.5, 8.0, and 9.0 MPa ) and temperatures (274.15 and 276.15 K), where the induction time, moles of consumed gas, and gas uptake rate were measured. The results demonstrated that pressure and temperature parameters were the most effective parameters affecting the induction time, gas consumption, and gas uptake rate. However, increasing pressure and reducing temperature led to a decrease in the induction time and an increase in gas consumption and gas uptake rate [17].

Significant attempts have been made to model/simulate various processes/systems such as gas hydrate formation and decomposition phenomena in oil and gas facilities using computational fluid dynamics (CFD) [24-31]. OLGA, a thermo-hydraulic computational modelling software, was developed by the Institute of Energy Technology in Norway in 1979; this software can be employed to analyze the transient behavior of a piping system during start-up and shut-down operations. This dynamic two-fluid model can be used to predict different parameters, such as

pressure drop, liquid holdup, temperature, and pressure of the system [32, 33]. Hydrates Research Center of the Colorado School of Mines incorporated a hydrate kinetic model in the industrial standard transient flow simulator, OLGA2000, for oil-dominated systems (CSMHyK). They verified this model with flow loop experimental data from two cases, including ChevronTexaco and ExxonMobil flow loops [34]. Researchers from the Colorado School of Mines improved the CSMHyK model for different systems using the flow loops and field data [28, 35-37]. CSMHyK is a transient gas hydrate model with three sub-models, including the kinetics model, transport model, and cold flow model [28]. Wang et al. (2018) developed a new transient hydrate formation model in which hydrate growth and transportability were simulated for the oil and water-dominated systems. They used this model to study the flow dynamics of a subsea tieback in different water cuts [37]. Hydrate formation in a subsea pipeline was simulated using ANSYS CFX- workbench 14 through conducting sensitivity analysis for various flow (velocity and diameter) and fluid (viscosity and water fraction) parameters [38]. The main limitation of their research was that the kinetic parameters were not included in the ANSYS. They investigated to explore where hydrate could potentially form according to the temperature distribution in the pipe. Neto et al. (2016) developed the mechanistic CFD model to study hydrate formation in a pipe. In the model, a kinetic reaction model was coupled with the transport equations, as well as the mass transfer of methane from gas to the liquid phase. The results revealed that methane solubility is the initial reaction step so that not all dissolved gas turns to the hydrate due to insufficient residence time of the flow in the pipe [39, 40]. Yao et al. (2019) investigated the effect of inclination on hydrate slurry flow in pipes. They applied the population balance model coupled with the Eulerian–Eulerian two-fluid multiphase flow model using the CFD software FLUENT 15. They studied the effect of three parameters, including inclination, flow rate, and initial particle size, on

the hydrate slurry flow in the pipe. Their results revealed that the pipes are helpful for the hydrate slurry flow. However, an increase in the flow rate and a decrease in the initial particle size led to an increase in the pressure drop of the hydrate slurry transport [41]. The dynamic model of hydrate slurry flow for hydrate agglomeration and hydrate breakage was developed. The proposed model was based on the population balance equation, which was coupled with different solid-liquid flow models and then solved by CFD software FLUENT 14.5. The impacts of flow rate and hydrate volume fraction on the hydrate particle size distribution, hydrate concentration distribution, and pipe pressure drop were simulated [42].

In recent years, there has been considerable interest in the simulation of hydrate formation in pipelines using STAR CCM+ [24, 25, 27]. The three-dimensional CFD model for hydrate formation in oil-dominated flows using STAR CCM+ was conducted in 2011 by Lo [24]. This theory was based on the Eulerian multiphase flow model, where three fluid phases of continuous oil, dispersed water droplets, and dispersed gas bubbles were considered. However, water droplets were converted to solid hydrate particles during the hydrate formation process in pipelines. The model included the heat, mass, and momentum conservation equations; it should be noted that the heat and mass processes involved in hydrate formation phenomena were added to the software as source terms. According to the results, no hydrate was formed in the entrance where the temperature was higher than the hydrate formation temperature, while hydrate was formed in the cooler regions, such as walls [24]. Balakin et al. (2011) studied the R11 hydrate deposition in turbulent water flow experimentally and theoretically. They applied the Eulerian-Eulerian CFD model with variable hydrate particle size expression for hydrate formation, and the results were validated using experimental data [25]. The turbulent slurry of oil, water, and gas hydrates was simulated using the CFD model in which the population balance technique (PBM) was coupled

with the Eulerian–Eulerian model. The simulation results were compared with experimental data for different parameters, including the slurry rheology and flow patterns of a pipe. The results of the model were also compared to the results obtained from the CSMHyK model (hydrate kinetics model from Colorado School of Mines) [27]. Zare et al. (2022) investigated the hydrate formation in the jumper for the methane-water system using the Eulerian multiphase flow model by employing CFD software (STAR CCM+). They added the mass transfer, hydrate reaction kinetics model, and heat of hydrate formation equations to the CFD software. Then, the operating conditions of the jumper are the fluid velocity of 5 m/s, an inlet temperature of 7°C, and a gas volume fraction of 0.2. The sensitivity analysis was performed to study the effects of changes in the inlet fluid velocity, gas volume fraction, inlet temperature, and subcooling on the hydrate formation [43].

Stirred reactors are one of the popular experimental systems to study hydrate formation/dissociation in terms of kinetics and thermodynamics phenomena. CFD software packages are generally employed to simulate stirred reactors for different applications in chemical engineering industries, such as the ethanol fermentation process, hydrothermal carbonization process, biohydrogen process, and bioreactor [44-46]. However, there are rarely published studies on hydrate formation/dissociation simulation in stirred reactors using CFD software. Also, the influences of main parameters, including stirring speed, pressure, subcooling, and gas volume fraction on the methane hydrate formation in the agitated reactor have been rarely investigated using STAR CCM+ software as a CFD tool. Hence, this paper is able to fill in this knowledge gap. This study employs STAR CCM+ software to examine methane hydrate formation in a stirred reactor. In this model, the transient turbulent CFD model based on Eulerian multiphase flow is used to simulate the influence of different parameters, including volume fraction, stirring rate,

pressure, and subcooling on the hydrate formation after validation of the model with experimental data taken from the literature.

## **4.2 CFD MODELING AND METHODOLOGY**

Computational fluid dynamics (CFD) is a method of analysis that is able to solve complicated problems through automating mathematical principles such as partial differential (PDE) and Navier stocks equations. This tool helps engineers to evaluate the effect of fluid flow characteristics on the design of different flow systems. CFD modelling approach comprises three steps: pre-processing, solving, and post-processing. In the pre-processing, the geometry is specified, and meshing is accomplished. In the solving step, the boundary conditions, initial conditions, and models are defined. After obtaining the results in the solving stage, analyzing the results are crucial. Methods such as vector plots, contour plots, data curves, and streamlines are used to present results for evaluation and result analysis. Figure 4-1 presents the flowchart for a typical CFD simulation. STAR CCM+ is the CFD software used in this research.

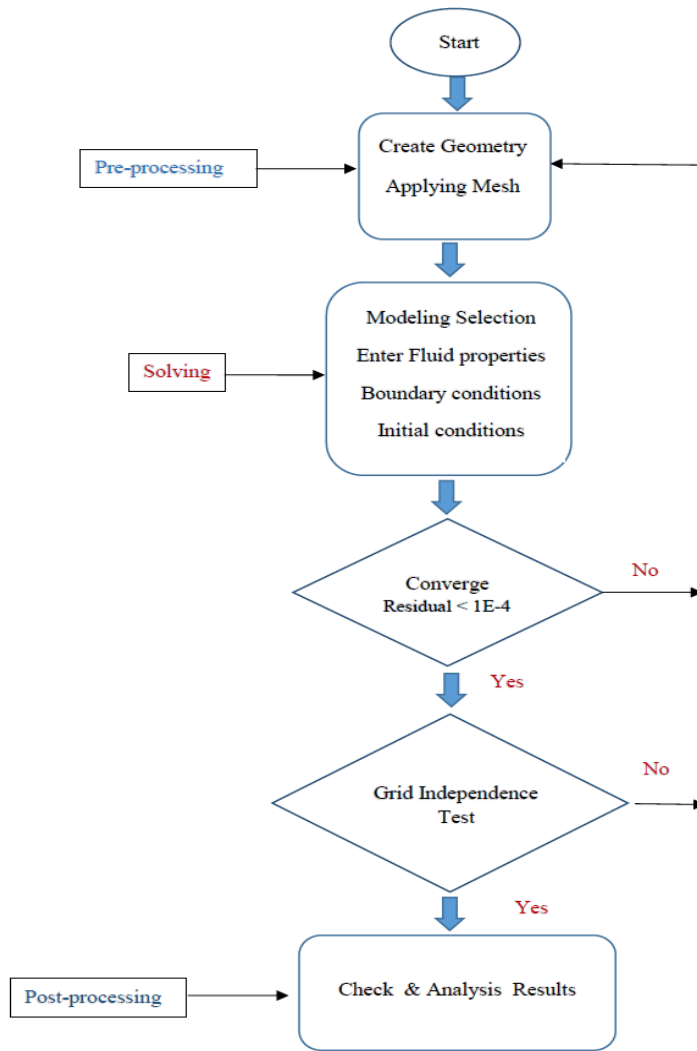


**Figure 4-1.** Flowchart for CFD simulation.

#### 4.2.1 Model Geometry

In this research, a stirred tank reactor is modeled based on a study conducted by Longinos and Parlaktuna (2021). They designed the reactor with internal dimensions of 150 mm in diameter and 312 mm in length and a total available volume of 5.7 liters to experimentally study the effect of impellers and baffles on the hydrate formation in the stirred reactor. In the current work, the size of the aforementioned reactor is scaled down to around 300 cm<sup>3</sup> to reduce simulation time. Figure

4-2 provides information about the geometry and dimensions of stirred reactor employed in this study.

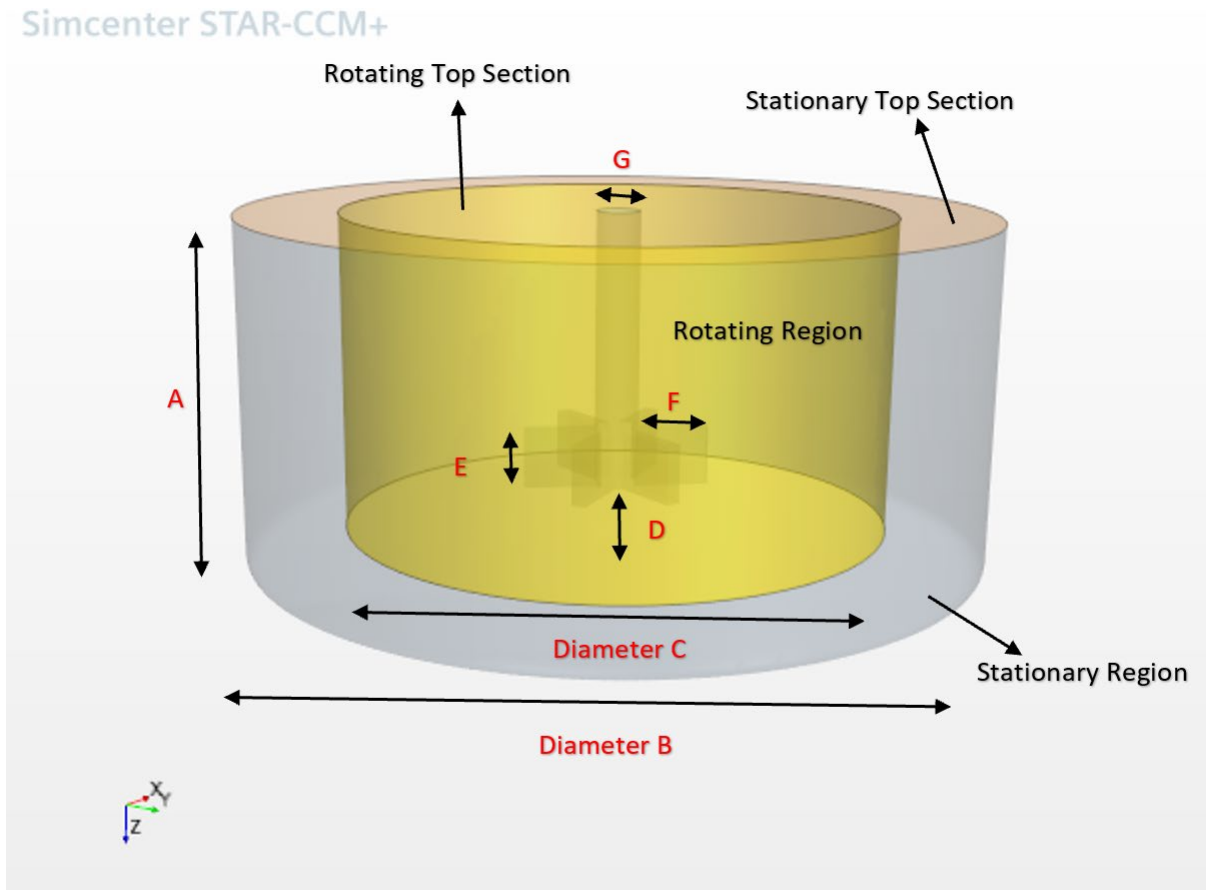


**Figure 4-2.** Three-dimensional CAD model of stirred reactor (A = 7 mm, B = 75 mm, C = 55 mm, D = 20 mm, E = 6 mm, F = 18.75 mm, and G = 5 mm)

According to Figure 4-2, the geometry considered for this reactor is a three-dimensional tank that is divided into two regions, including rotating and stationary sections. In Figure 4-2, the stationary section with a diameter of 75 mm is colored in gray. The rotating region with a diameter of 55 mm and an impeller attached to the shaft at a distance of 20 mm from the tank surface is shown in yellow colour. It is noted that for boundary condition definition, the tank top is a pressure outlet

as this reactor is a high-pressure reactor for methane hydrate formation, while the rest of the geometry is solid with no-slip walls and zero velocity. In fact, we need to specify the value of the radial stirring rate (RPM) in the CFD software.

#### **4.2.2 Mesh Creation and Mesh Independence Test**

STAR CCM+ software has a wide range of mesh models that need to be correctly selected for complicated geometries; otherwise, the simulation results may not have adequate accuracy [47, 48]. Although using a fine mesh has a significant impact on the accuracy of the results, an increase in the resolution leads to an increase in the run time of the simulation [49]. In this study, three mesh models, including polyhedral mesher, prism layer mesher, and surface remesher, are employed for two motionless and rotating regions. Polyhedral volume mesh creates a high-quality mesh, which provides a good balance between the simulation speed and precision. This mesher is mostly applicable for internal flows. The prism layer mesh is crucial for the boundary layer and accurate turbulence modeling. This mesher generates orthogonal prismatic cells next to wall surfaces or boundaries using core volume mesh. One of the parameters of the prism layer mesh that can be adjusted is the number of cell layers. This parameter controls the number of cell layers that are generated within the prism layer on a part of surface or boundary, where the default value for the number of cell layers is suggested as 2 according to the STAR CCM+ procedure [48]. In this research, the number of cell layers is considered 3 to increase the precision of the result simulations. However, a high value of this parameter leads to an increase in simulation time due to the high number of meshes close to the wall surfaces or boundaries. The surface remesher is able to resolve face quality errors and remesh the areas that have not meshed correctly [47].

One of the essential steps in CFD simulations is the mesh independence test. The accuracy of the results of CFD simulations is generally dependent on the mesh quality. The simulation runs can be considered mesh independent when the accuracy of the selected model has not changed appreciably with increasing the number of mesh elements. In fact, the agreement between experimental data and simulation results does not show that the simulation is mesh-independent [50]. In this work, the hydrate mass fraction and liquid velocity are considered for the mesh independence study. In other words, when the values of these two parameters do not change considerably with the increase in the number of mesh elements, it means the simulation is mesh-independent. The results of the simulation cases with different polyhedral volume cell numbers of 143,709, 226,106, 371,162, and 495,011 for two parameters of hydrate mass fraction and liquid velocity are compared. Finding demonstrated that the optimal number of meshes is 226,106, leading to more precise results than other cases. Figure 4-3 depicts the mesh layout of the stirred reactor and the plate section drawn in the middle of the reactor. It is worth mentioning that the impeller is a rotating solid that helps increase mass transfer in this system; thus, there is no need to mesh it.

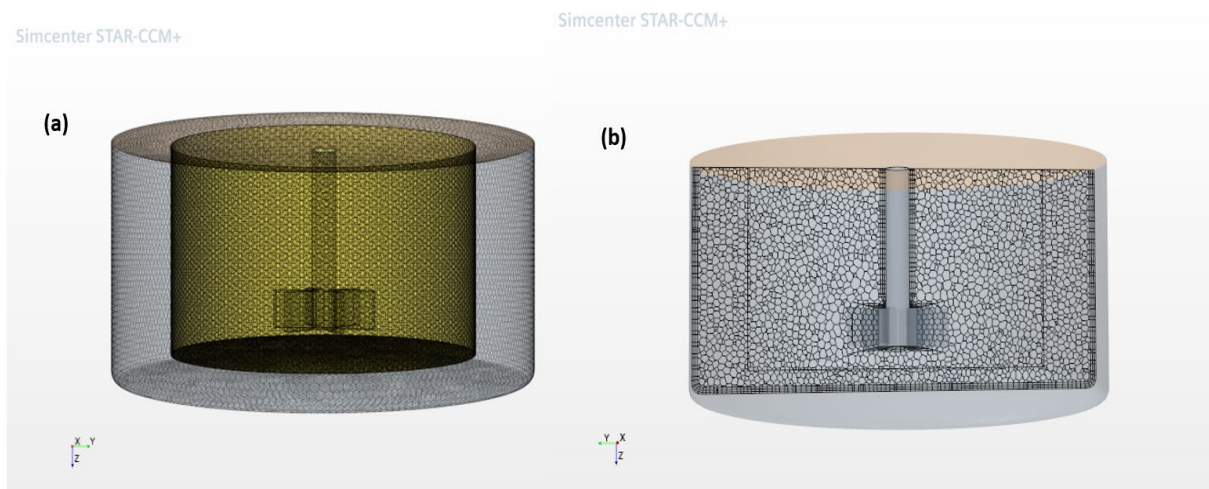


**Figure 4-3.** Mesh layout of the stirred reactor (a) and plate section (b)

### 4.2.3 Boundary and Initial Conditions

Proper definition of boundary and initial conditions significantly affects the results of CFD simulations; thus, they should be specified correctly. The stirred reactor is divided into motionless and rotating regions, as shown in Figure 4-2. The rotating region contains an impeller. The pressure outlet is the only boundary condition that is considered for rotating and motionless top sections. In contrast, other sections of the stirred reactor (all solid/fluid interfaces) are solid walls with a temperature of 1.15°C and no-slip conditions. It means that the velocity is zero for the inlet and outlet of the reactor, and only the impeller has a rotational speed in the range of 300 to 900 rpm. Also, there is a convection heat transfer between the common boundaries of the rotating and stationary regions. In this study, the pressure range for the outlet pressure boundary condition is between 3,500 kPa to 7,500 kPa. Table 4-1 reports the values of the parameters used in the transient model. As mentioned earlier, the values of initial and boundary conditions parameters must be added to the software. Therefore, the values that are entered for the initial condition in the software are the same as the values of boundary conditions to reduce simulation time.

**Table 4-1.** Boundary conditions and range of parameters for the CFD model.

Parameter	Value
Impeller speed	300-900 RPM
Outlet pressure	3,500-7,500 kPa
Gas volume fraction	0.04-0.4
System temperature	274.3 K

## 4.3 Computational Fluid Dynamic Model

In CFD simulation, the equations of momentum, heat, and mass transfer are discretized and solved iteratively for each cell. As a result, the values of parameters can be obtained approximately. The

turbulence equations are also solved along with the continuity equation, the Navier–Stokes equation, and the energy equation [45]. This paper introduces a mathematical model to study methane hydrate formation in the stirred reactor. Based on the Eulerian multiphase flow, this model considers water and hydrate as continuous phases and methane gas bubbles as dispersed phase [24, 26, 27, 43]. There are some assumptions with this simulation: 1) although gas and liquid are in the stirred reactor, the model simulates the liquid phase in which water + hydrate is a continuous fluid, and the gas bubbles form a dispersed phase [24], 2) water is altered to hydrate when it meets the methane gas bubbles, 3) the model is transient, 4) the system is at the isothermal condition, and 5) hydrate nucleation occurs immediately at a specific subcooling.

In this model, it is essential to determine the amount of methane hydrate formed in the reactor in the water phase. Therefore, the hydrate mass fraction is defined as the mass fraction of hydrate in the water phase, as denoted by  $f_{hyd}$ . When only pure water exists in the system, it implies  $f_{hyd} = 0$ ; and  $f_{hyd} = 1$  means that pure hydrate is in the system.

In this paper, the Eulerian – Eulerian multiphase model is selected for CFD simulations, consisting of continuity, momentum, turbulent, and energy equations. The hydrate formation equations also are added to this model to simulate methane hydrate formation in the stirred reactor.

**Transport equations.** The continuity equation for phase ‘k’ is given below [26, 43, 48]:

$$\frac{\partial}{\partial t} \phi_k \rho_k + \nabla \cdot \phi_k \rho_k \vec{u}_k = \sum_{j=1}^N (\dot{m}_{jk} - \dot{m}_{kj}) \quad (4-1)$$

where  $\phi_k$  stands for the volume fraction of phase  $k$ ;  $t$  is the time;  $\rho_k$  refers to the phase density;  $\vec{u}_k$  introduces the velocity of phase  $k$ ; and  $\dot{m}$  represents the mass transfer rate. The sum of the volume fractions is equal to 1, as shown below:

$$\sum_k \phi_k = 1 \quad (4-2)$$

The momentum equation for phase  $k$  is defined as follows:

$$\begin{aligned} \frac{\partial}{\partial t} \phi_k \rho_k \vec{u}_k + \bar{\nabla} \cdot (\phi_k \rho_k \vec{u}_k \vec{u}_k) - \bar{\nabla} \cdot (\phi_k \mu_k (\bar{\nabla} \vec{u}_k + (\bar{\nabla} \vec{u}_k)^T)) \\ = -\phi_k \bar{\nabla} p + \phi_k \rho_k \vec{g} + M_k \end{aligned} \quad (4-3)$$

where

$$M_k = \sum_{j \neq k} (F_{kj}^D + F_{kj}^{VM} + F_{kj}^{TD}) + \sum_{j=1}^N (\dot{m}_{jk} \vec{u}_j - \dot{m}_{kj} \vec{u}_k) \quad (4-4)$$

where  $\mu_k$  is the phase viscosity;  $p$  stands for the pressure;  $\vec{g}$  denotes the gravity acceleration; and  $M$  represents the sum of interfacial forces and momentum associated with the mass transfer.

Further detail about Equation (4) is found in Appendix A.

The energy conversation for phase  $k$  is given below:

$$\frac{\partial}{\partial t} (\phi_k \rho_k h_k) + \bar{\nabla} \cdot (\phi_k \rho_k \vec{u}_k h_k) - \bar{\nabla} \cdot \left[ \phi_k \left( \lambda_k (\bar{\nabla} T_k + \frac{\mu_{tk}}{\sigma_t} \bar{\nabla} h_k) \right) \right] = Q \quad (4-5)$$

where  $h$  is the phase enthalpy;  $\lambda$  represents the thermal conductivity;  $\mu$  is the turbulent viscosity;  $\sigma_t$  symbolizes the turbulent Prantle number with the value of 0.9; and  $Q$  introduces the heat source [24].

**Hydrate equations.** The summation of volume fraction for two phases (methane gas and water, which form hydrate) is equal to unity [24, 26, 43].

$$\phi_g + \phi_w = 1 \quad (4-6)$$

Methane gas is dissolved in water in the interphase. Upon maintaining proper conditions (high pressure and low temperature in the system) methane hydrate phase is then formed according to the chemical reaction, as given below:



where,  $n_{CH_4}$ ,  $n_{H_2O}$ , and  $n_{hyd}$  are the stoichiometric coefficients with the values of 1, 5.75, and 1, respectively.

The mass transfer should occur between two phases of methane gas and water for the hydrate formation. The continuity equations for the gas, water, and hydrate phases are given below:

$$\frac{\partial}{\partial t} (\phi_g \rho_g) + \bar{\nabla} \cdot (\phi_g \rho_g \vec{u}_k) = -\dot{m}_{CH_4} \quad (4-8)$$

$$\frac{\partial}{\partial t} (\phi_w \rho_w f_w) + \bar{\nabla} \cdot (\phi_w \rho_w \vec{u}_k f_w) = \dot{m}_{CH_4} \left( 1 - \frac{W_{hyd} n_{hyd}}{W_{CH_4} n_{CH_4}} \right) \quad (4-9)$$

$$\frac{\partial}{\partial t} (\phi_w \rho_w f_{hyd}) + \bar{\nabla} \cdot (\phi_w \rho_w \vec{u}_k f_{hyd}) = \dot{m}_{CH_4} \left( \frac{W_{hyd} n_{hyd}}{W_{CH_4} n_{CH_4}} \right) \quad (4-10)$$

where  $f_w$  and  $f_{hyd}$  denote the mass fractions of water and hydrate in the liquid phase ( $f_w + f_{hyd} = 1$ );  $W_{hyd}$  (=119.65 kg/mol) is the molar mass of methane hydrate;  $W_{CH_4}$  (= 16.04 kg/mol) stands for the molar mass of methane gas; and  $\dot{m}_{CH_4}$  refers to the amount of dissolved methane gas in the water, which is changed to hydrate due to the chemical hydrate reaction [24].

Based on the assumptions in this study, hydrate nucleation occurs immediately after a specific subcooling temperature, which is defined by the following equation [24, 43]:

$$\Delta T_{sub} = T_{hyd} - T_{system} \quad (4-11)$$

where  $T_{hyd}$  stands for the hydrate equilibrium temperature at system pressure, and  $T_{system}$  is the temperature of the reactor. The following equation is considered for the subcooling temperature in the CFD model:

$$\Delta T_{sub} = \max (T_{hyd} - T_{system}, 0) \quad (4-12)$$

$\dot{m}_{CH_4}$  is the methane consumption rate, determined based on the following intrinsic kinetics equation:

$$-\frac{dm_{gas}}{dt} = uk_1 \exp\left(\frac{-k_2}{T_{sys}}\right) A_s (\Delta T_{sub}) \quad (4-13)$$

where,  $k_1$  and  $k_2$  refer to the intrinsic rate constants;  $A_s$  represents surface area;  $\Delta T_{sub}$  stands to subcooling; and  $u$  is equal to 1/500. Subcooling is a driving force for hydrate formation defined as a difference between hydrate equilibrium temperature (at the system pressure) and actual system temperature.

The methane consumption rate equation was suggested by Vysniauskas and Bishnoi (1983) and Englezos et al. (1987) [51, 52]. They conducted experiments for methane and ethane hydrate formation to calculate  $k_1$  and  $k_2$  [28, 35, 37]. The correction value ( $u$ ) was suggested for gas consumption rate to achieve a good match with experimental data. Indeed, the mass and heat transfer resistances were included in this correction factor [36, 53]. In this research, the values of  $k_1$  and  $k_2$  are  $1.7427 \times 10^{15} \left(\frac{lb_m}{in.^2 hr^\circ R}\right)$  and  $24509.21^\circ R$ , respectively [36].

$A_s$  is the surface area of gas bubbles that convert into hydrate particles when water contact bubbles according to the assumption considered in this study. This parameter is calculated as follows [54]:

$$A_s = \frac{6\phi_g}{d_b} \quad (4-14)$$

where  $\phi_g$  represents the gas volume fraction and  $d_b$  is the bubble diameter that is considered to be  $40 \times 10^{-6}$  m [34].

As hydrate formation is an exothermic reaction. Hence, energy is released when hydrates form in the reactor. The heat of hydrate formation needs to be added to the energy equation (as a heat source). The equation used in this model for the energy created by hydrate formation is expressed as a function of hydrate equilibrium temperature, as follows [24]:

$$\dot{q}_{hyd} = \dot{m}_{CH_4} C_{p_{hyd}} T_{hyd} \quad (4-15)$$

where,  $C_{p_{hyd}}$  is the heat capacity of hydrate;  $T_{hyd}$  introduces the hydrate equilibrium temperature; and  $\dot{m}_{CH_4}$  stands for the consumption rate of methane gas changed to hydrate.

#### 4.3.1 Numerical Solution

The implicit SIMPLE technique is employed to solve Equations 1 to 15 using the commercial CFD package STAR CCM+ revision 15.04.010. Table 4-2 reports the thermophysical properties of methane, water, and hydrate, where the properties of methane and water are calculated using PVTsim Nova, and the properties of hydrate are borrowed from the literature [34]. Selecting a proper time step and simulation time may help achieve transient stability and numerical accuracy. Therefore, three different time steps of 0.1, 0.01, and 0.001 seconds with different simulation times ranging from 0 to 200 seconds were applied to find an appropriate time step and time simulation.

According to the results, the proper time step and simulation time were 0.01 and 15 seconds, respectively. Table 4-3 presents the specifications of the Eulerian- Eulerian multiphase model, which is used along with standard  $k - \epsilon$  turbulence and Realizable k-epsilon two-layer to simulate methane formation in the stirred reactor.

**Table 4-2.** Thermophysical properties for water, methane, and hydrate used in the CFD modeling.

Parameter	Value
Water phase density	1000.6 kg/m <sup>3</sup>
Water dynamic viscosity	0.0011 Pa-s
Water specific heat	4813.03 J/kg-K
Water thermal conductivity	0.60548 W/m-K
Hydrate phase density	807.80 kg/m <sup>3</sup>
Hydrate dynamic viscosity	0.0015 Pa-s
Hydrate thermal conductivity	0.34 W/m K
Hydrate specific heat	2100 J/kg K
Methane thermal conductivity	0.04543 W/m-K
Methane dynamic viscosity	1.39 E-5 Pa-s
Methane specific heat	3096.43 J/kg K

**Table 4-3.** CFD Model specifications for hydrate formation simulation in the stirred reactor

Space	Three dimensional
Meshing	Polyhedral with near-wall effect
Simulation type	Implicit unsteady with the time step 0.01 s and time duration of 15 s
Main model	Eulerian multiphase flow model
Turbulent Model	Standard $k - \epsilon$ turbulence, Realizable k-epsilon two-layer
Fluid	Methane and water
Pipe wall	No-slip conditions
g	9.8 m/s <sup>2</sup>

### 4.3.2 Model Validation

In this study, the developed model is validated using the experimental data published by Vysniauskas and Bishnoi (1983) [51]. Their study used a reactor with an inside diameter of 7.62 cm and an internal capacity of about 500 cm<sup>3</sup>. The sample inside the reactor (300 cm<sup>3</sup>) was stirred by a magnetic stir bar that was coupled to a magnet mounted on a pneumatically driven turbine at the base of the reactor, where the stirring rate was adjusted between 0 to 600 RPM. They

investigated the methane hydrate formation at 5,500 kPa and 274.3 K at different stirring rates [51]. Therefore, the volume of the reactor simulated in this paper is the same as the reactor employed in the work by Vysniauskas and Bishnoi (1983) [51]. However, we used the impeller with a shaft for stirring in the system, according to Figure 4-2. Table 4-4 reports the comparison of experimental data and simulation results for the methane consumption when the reactor is at 5,500 kPa pressure and 274.3 K with a stirring rate of 300 rpm. Based on Table 4-4, the simulation results are in good agreement with the experimental data. For instance, the overall AAD% is 15.7%. It should be noted that the AAD% for some data, including 21, 25, and 30 seconds is higher than other values. The difference between the simulation and experimental results is due to the stochastic nature of hydrate nucleation [35]. Another reason for the differences between the experimental data and simulation results is the delay in methane hydrate nucleation in reality. The model assumes that hydrate nucleation occurs immediately after a specific subcooling when water molecules contact gas bubbles. However, several parameters may control hydrate nucleation in practice, including the stochastic behavior of hydrate formation in the stirred reactor.

**Table 4-4.** Validation of the CFD model with experimental data

<b>t(s)</b>	<b>m<sub>CH4-Cal.</sub> (g)</b>	<b>m<sub>CH4-Exp.</sub> (g)</b>	<b>AD (g)</b>	<b>AAD%</b>
3.9	0.0077	0.0102	0.2381	23.81
4.5	0.0093	0.0106	0.1245	12.45
5	0.0105	0.0110	0.0467	4.673
5.4	0.0113	0.0113	0.0067	0.667
6	0.0126	0.0117	0.0752	7.522
7	0.0144	0.0124	0.1571	15.71
8	0.0157	0.0131	0.1975	19.75
9	0.0163	0.0138	0.1808	18.08
10	0.0164	0.0146	0.1284	12.84
11	0.0163	0.0153	0.0676	6.762
11.5	0.0162	0.0156	0.0358	3.588
12	0.0161	0.0160	0.0096	0.964
15	0.0164	0.0181	0.0944	9.444
21	0.0155	0.0224	0.3085	30.85

25	0.0155	0.0253	0.3867	38.67
30	0.0157	0.0288	0.4542	45.42
<b>Overall</b>				<b>15.70</b>

#### 4.4 RESULTS AND DISCUSSION

In this paper, the methane hydrate formation in the stirred reactor is simulated using STAR CCM+ software by considering two phases of hydrate + water as a continuous phase and gas bubbles as a dispersed phase. The simulation runs are based on the Eulerian multiphase flow model as described in Section 2. This CFD model is first applied to simulate the hydrate formation of methane in the stirred reactor with a constant temperature of 274.3 K and a pressure of 5,500 kPa. In this case, the volume fraction of the gas is 0.04. Then, the influences of volume fraction (0.04 to 0.4), impeller speed (300 to 900 rpm), Pressure (3,500 to 7,500 kPa), and subcooling (1.93 to 9.23) on the methane hydrate formation are investigated.

Figure 4-4 illustrates the mass fraction of hydrate in the liquid phase in the stirred reactor for a case where the stirring rate is 300 rpm, the system pressure is 5,500 kPa, the gas volume fraction is 0.04, and the reactor temperature is 274.3 K. Other parameters have the same values as presented in Table 4-2. According to Figure 4-4 (a), it is observed that hydrate is formed around the stirrer blades and close to the walls. The total amount of methane hydrate formed in this case is 0.0164 g. Figure 4-4 (b) depicts the methane volume fraction contour in the stirred reactor. Figure 4-4 (a) and (b) shows that the lower the volume fraction of methane, the more hydrate forms in the reactor. It means that a higher hydrate concentration is observed in the area around the impeller blades and near the walls, where the volume fraction of methane is small, equal to 0.008. The results agree with the experiments conducted by Burla et al. (2022) [55]. They observed the hydrate formed on the reactor wall as also seen in Figure 4-5. The cross-section area of the stirred reactor, Figure 4-4,

is shown in Figure 4-5. According to Figure 4-5, more methane hydrate can be observed in the red color regions, where they are near the wall. Note that the methane hydrate can be detected in the yellow areas, where the mass fraction of the hydrate is 0.00013.

Sensitivity analysis of the key parameters, such as stirring rate, volume fraction, pressure and subcooling provides more insight into hydrate formation in the stirred reactor.

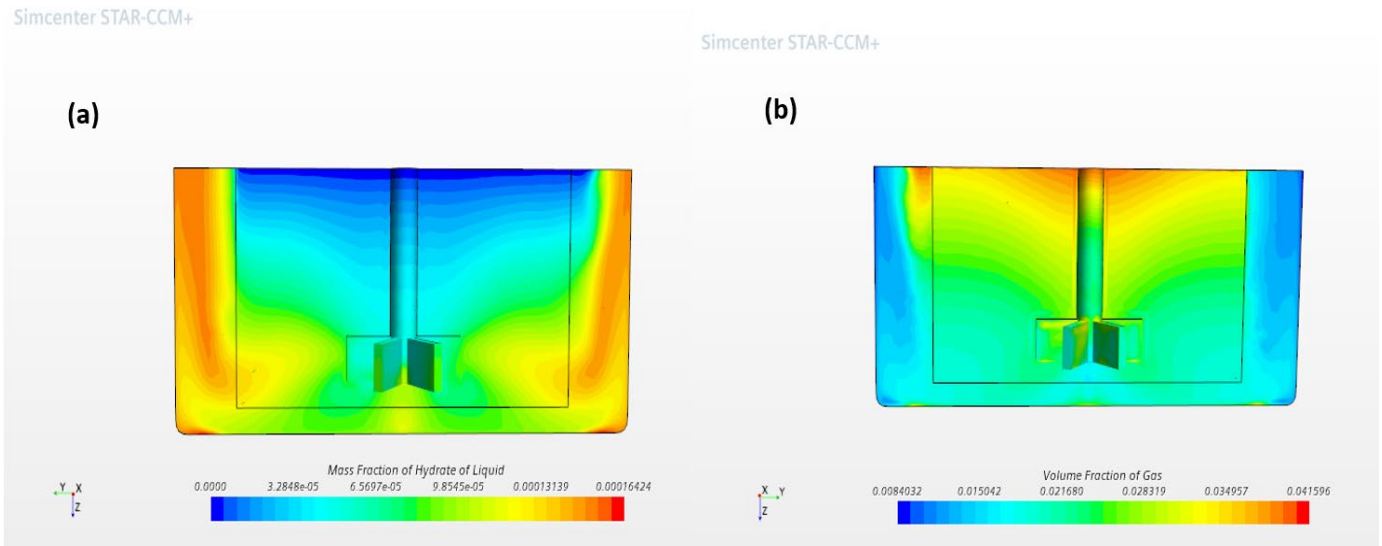


**Figure 4-4.** Hydrate mass fraction (a) and gas volume fraction in the stirred reactor (b) [stirring rate = 300 rpm, pressure = 5,500 kPa, gas volume fraction = 0.04, and system temperature = 274.3 K].

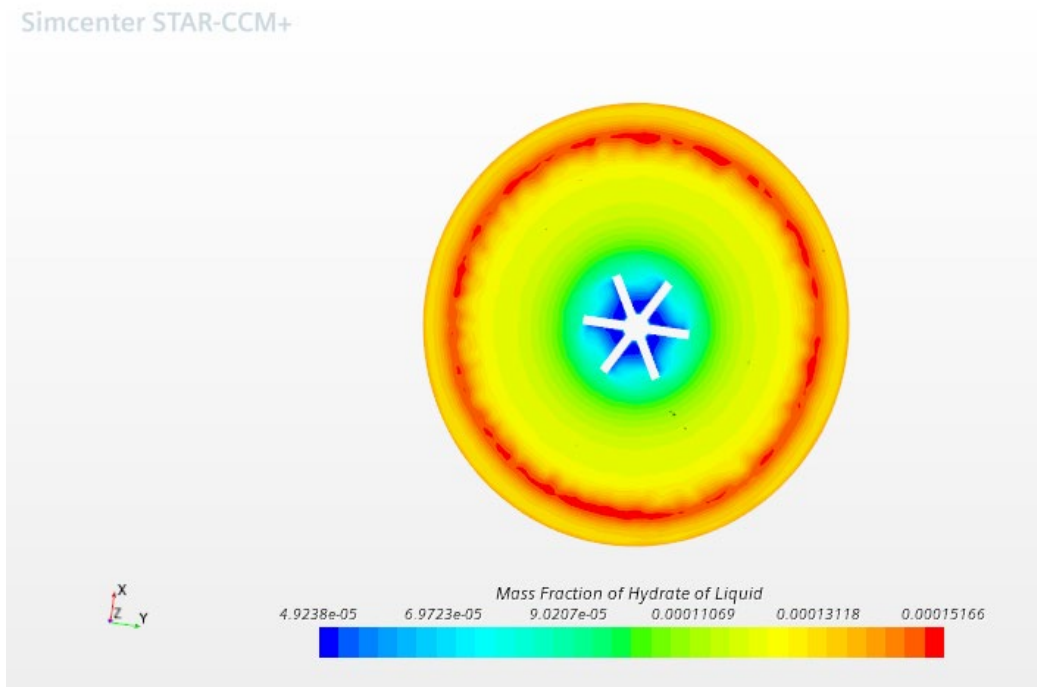


**Figure 4-5.** Hydrate mass fraction contour for cross-section area of stirred reactor [stirring rate= 300 rpm, gas volume fraction = 0.04, pressure = 5,500 kPa, and system temperature = 274.3 K].

#### 4.4.1 Effect of Stirring Rate

Different cases with various agitation rates of 300, 500, 700, and 900 RPM are simulated to determine the hydrate mass fraction for the stirred reactor, as indicated Figure 4-6. The gas pressure, temperature, and volume fraction for these simulations are 5,500 kPa, 274.3 K, and 0.04, respectively. Table 4-5 tabulates or presents the mass fraction of methane hydrate formed in the reactor for impeller speeds of 300, 500, 700, and 900 RPM. As clear from Table 4-5, if the impeller speed increases from 300 to 900 RPM, the mass of methane hydrate increases so that the maximum value of the hydrate mass fraction is  $3.35 \times 10^{-4}$  when the stirring rate is 900 rpm. In comparison, this parameter is minimal with the value of  $1.70 \times 10^{-4}$  when the impeller speed is 300 RPM. It is noted that the hydrate mass fraction for the stirring rates of 500 and 700 RPM are  $2.54 \times 10^{-4}$  and

$3.14 \times 10^{-4}$ , respectively. According to Figure 4-6 (a) to Figure 4-6 (d), the blue area with no hydrate decreases when the stirring rate increases from 300 to 900 RPM. It implies that an increase in the stirring rate leads to more hydrate formation in the reactor. This is because the higher stirring rate helps reduce the heat and mass transfer resistance for methane hydrate formation [56]. On the other hand, increasing the stirring rate leads to a larger contact area between gas and water. This larger area will increase the velocity of the gas molecule moving to the liquid phase. Therefore, the concentration of gas in the liquid phase will increase compared with the lower stirring speed. However, increasing stirring speed might reduce nuclei formation [57]. Qureshi et al. (2017) revealed that the nucleation of hydrate has a tendency to decrease when the stirring rate is high (around 1000 to 1400 RPM), while hydrate crystal formation is increased when the stirring rate is between 550 and 750 RPM [13].

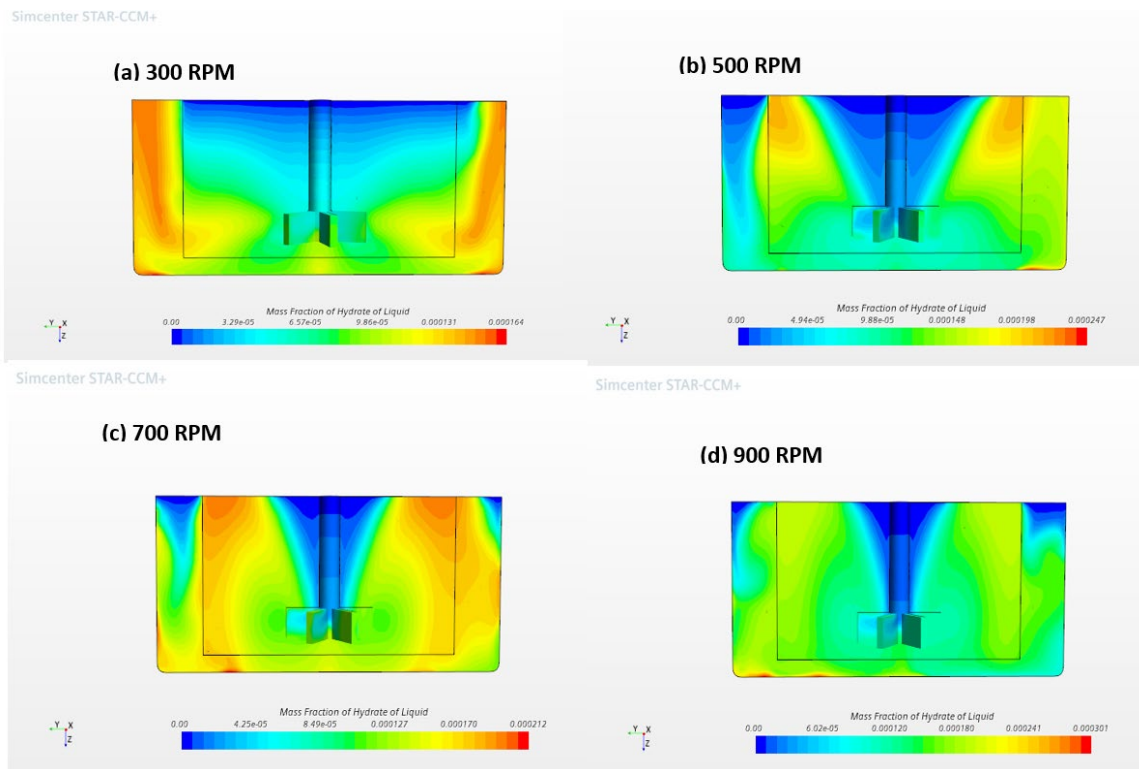


**Figure 4-6.** The effect of stirring rates on the hydrate mass fraction in the stirred reactor [gas volume fraction = 0.04, system pressure = 5,500 kPa, and system temperature = 274.3 K].

**Table 4-5.** Mass fraction of hydrate as a function of stirring rate [gas volume fraction = 0.04, system pressure = 5,500 kPa, and system temperature = 274.3 K].

Stirring rate (RPM)	Methane hydrate mass fraction ( $\times 10^4$ )
300	1.70
500	2.54
700	3.14
900	3.35

#### 4.4.2 Effect of Gas Volume Fraction

Gas hydrate formation usually occurs when there are water and light hydrocarbon gases in the system under high pressure and low-temperature conditions. Therefore, the amount of gas (methane volume fraction) is vital for hydrate formation in the stirred reactor. As mentioned earlier, the methane consumption rate is a function of the gas volume fraction. The impact of gas volume fraction in the range of 0.04 to 0.4 on the methane hydrate formation is investigated where the stirring rate is between 300 to 900 RPM, as shown in Figure 4-7. The pressure and temperature for the simulation runs are 5,500 kPa, and 274.3 K, respectively. According to Figure 4-7, the amount of hydrate in the stirred reactor increases with increasing gas volume fraction and stirring rate. However, the amount of methane hydrate formed in different stirring rates for the gas volume fractions of 0.04 and 0.1 is significantly lower than that of other gas volume fractions (0.2, 0.3, and 0.4). The maximum amount of methane hydrate is 1.38 g, when the gas volume fraction and stirring rate are 0.4 and 900 RPM, respectively. However, the minimum value of methane hydrate is 0.092 g, where the volume fraction is 0.04. Figure 4-7 also reveals that an increase in methane volume fraction leads to a significant increase in the amount of hydrate formation at a constant stirring rate. For instance, the amount of hydrate increases from 0.1387 to 1.305 g at the stirring rate of 700 RPM when the volume fraction changes from 0.04 to 0.40. This parameter for the cases with the volume fractions of 0.1, 0.2, and 0.3 at the stirring rate of 700 RPM is 0.269, 0.574, and

0.902 g, respectively. It is worth noting that methane is a limiting reactant due to low solubility in water based on the gas hydrate reaction equation. Therefore, increasing the volume fraction of gas can help increase the solubility of methane gas in the water; therefore, the amount of methane hydrate formed in the reactor increases significantly.

Figure 4-8 shows methane hydrate formation in the stirred reactor for different volume fractions of 0.1, 0.2, 0.3, and 0.4 when the stirring speed is 500 RPM. As shown in Figure 4-8, if the gas volume fraction increases from 0.1 to 0.4, the mass fraction of hydrate in the agitated reactor increases from  $6.19 \times 10^{-4}$  to  $2.19 \times 10^{-3}$ . According to Figure 4-8, it can be concluded that methane hydrate is formed in the reactor, particularly in the areas near the reactor wall and around the stirrer. However, hydrate can not be observed near the stirrer shaft due to stirrer motion. The increasing volume fraction of the gas has a significant impact on the hydrate formation so that the amount of hydrate in the reactor for the volume fraction of 0.40 is 1.21 g when the pressure and temperature are 5,500kPa and 274.3 K, respectively, while this value for the volume fraction of 0.100 is 0.239 g. Also, the amounts of hydrate for the volume fractions of 0.2 and 0.3 are 0.557 and 0.876 g, respectively.

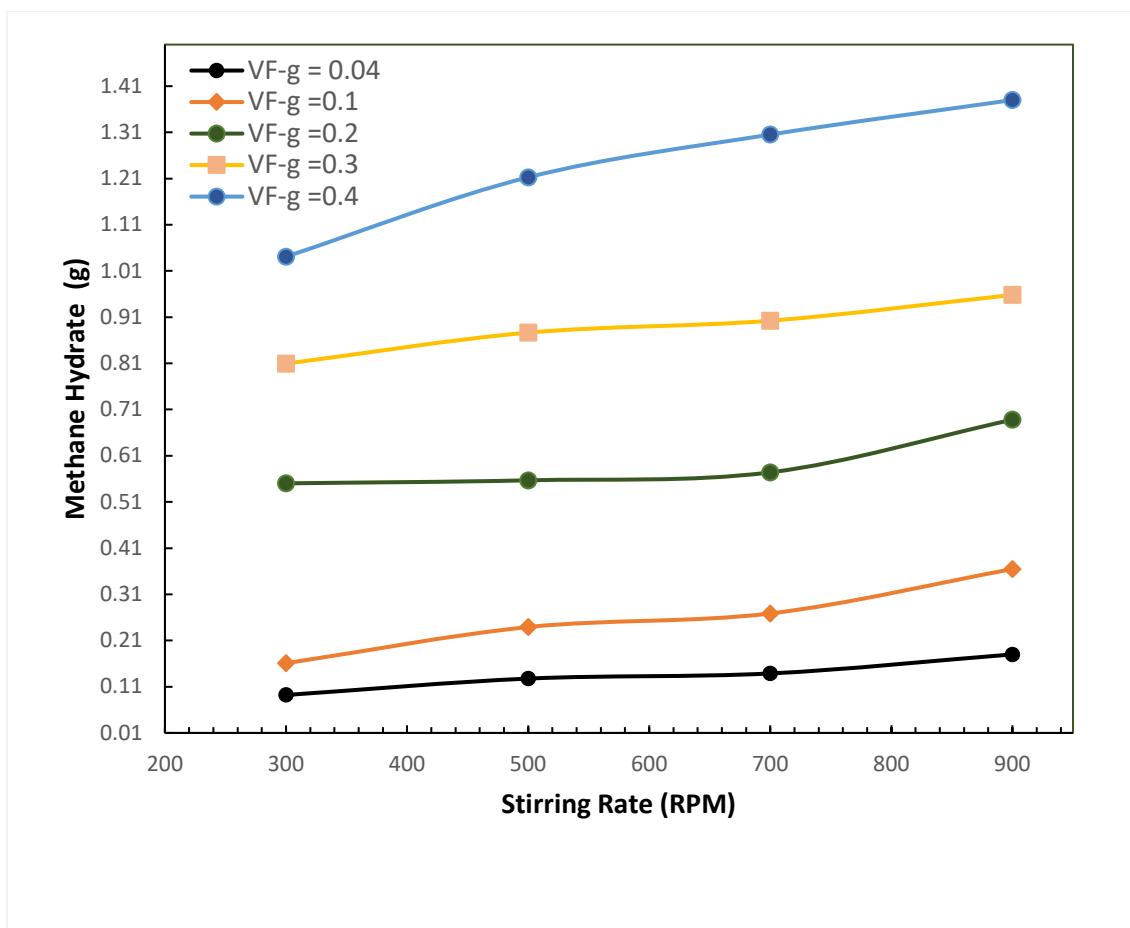
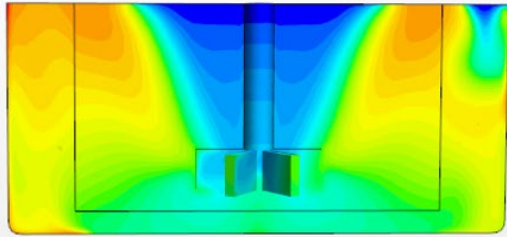


**Figure 4-7.** Effect of gas volume fraction and stirring rate on the methane hydrate formation in the stirred reactor, [pressure = 5,500 kPa, system temperature = 274.3 K].

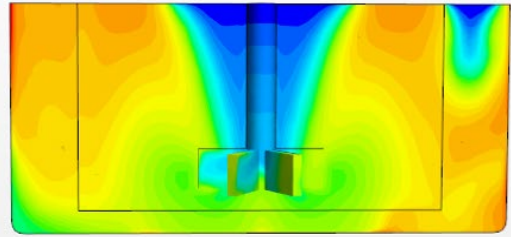
Simcenter STAR-CCM+

(a)  $VF_{\text{gas}} = 0.1$



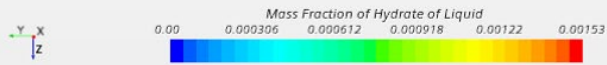
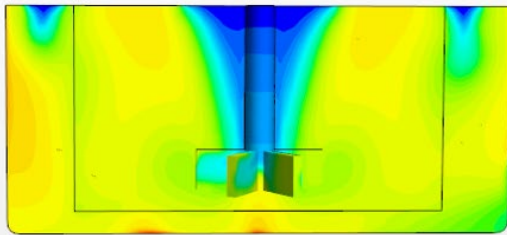
Simcenter STAR-CCM+

(b)  $VF_{\text{gas}} = 0.2$



Simcenter STAR-CCM+

(c)  $VF_{\text{gas}} = 0.3$



Simcenter STAR-CCM+

(d)  $VF_{\text{gas}} = 0.4$

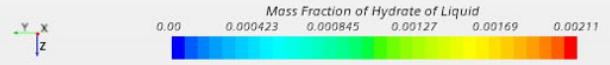
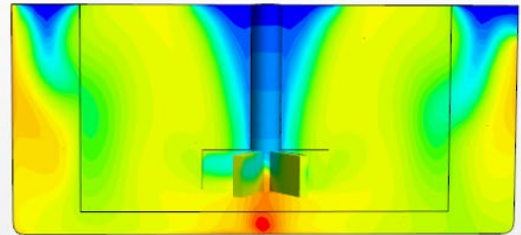


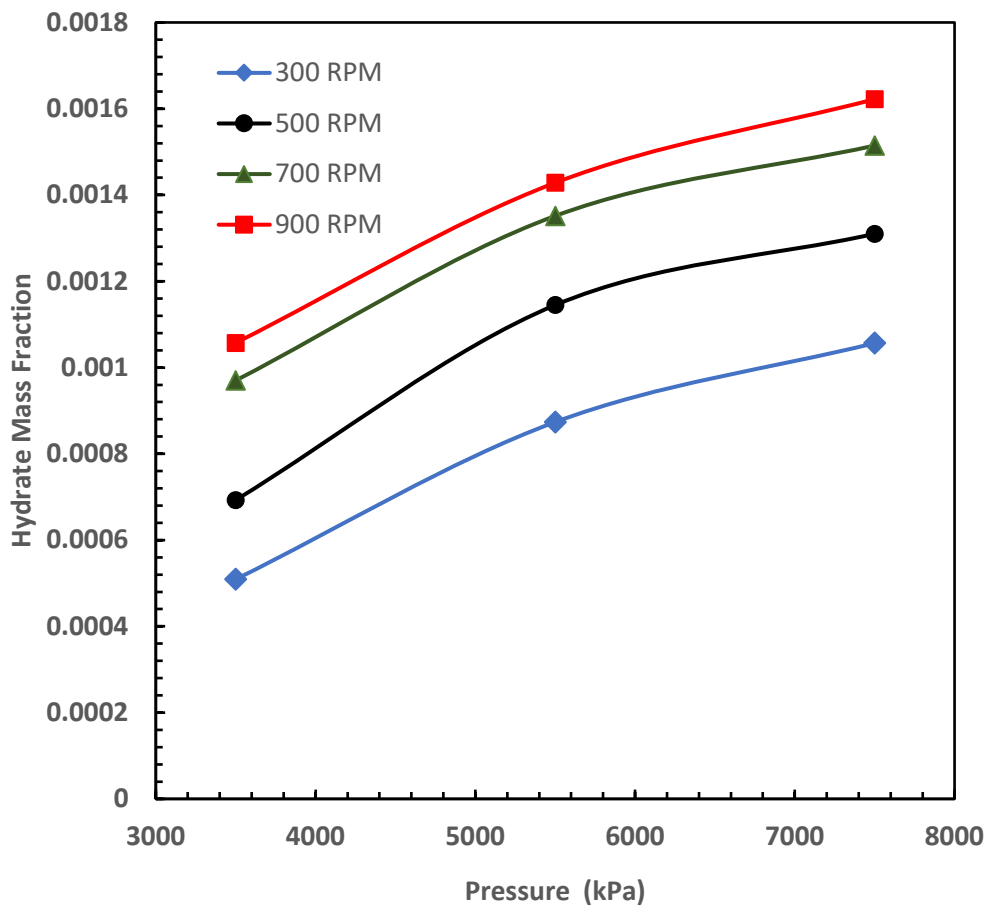
**Figure 4-8.** Effect of gas volume fraction on the methane hydrate formation in the stirred reactor [stirring rate = 500 RPM, pressure = 5,500 kPa, system temperature = 274.3 K].

### 4.4.3 Effect of Pressure and Subcooling

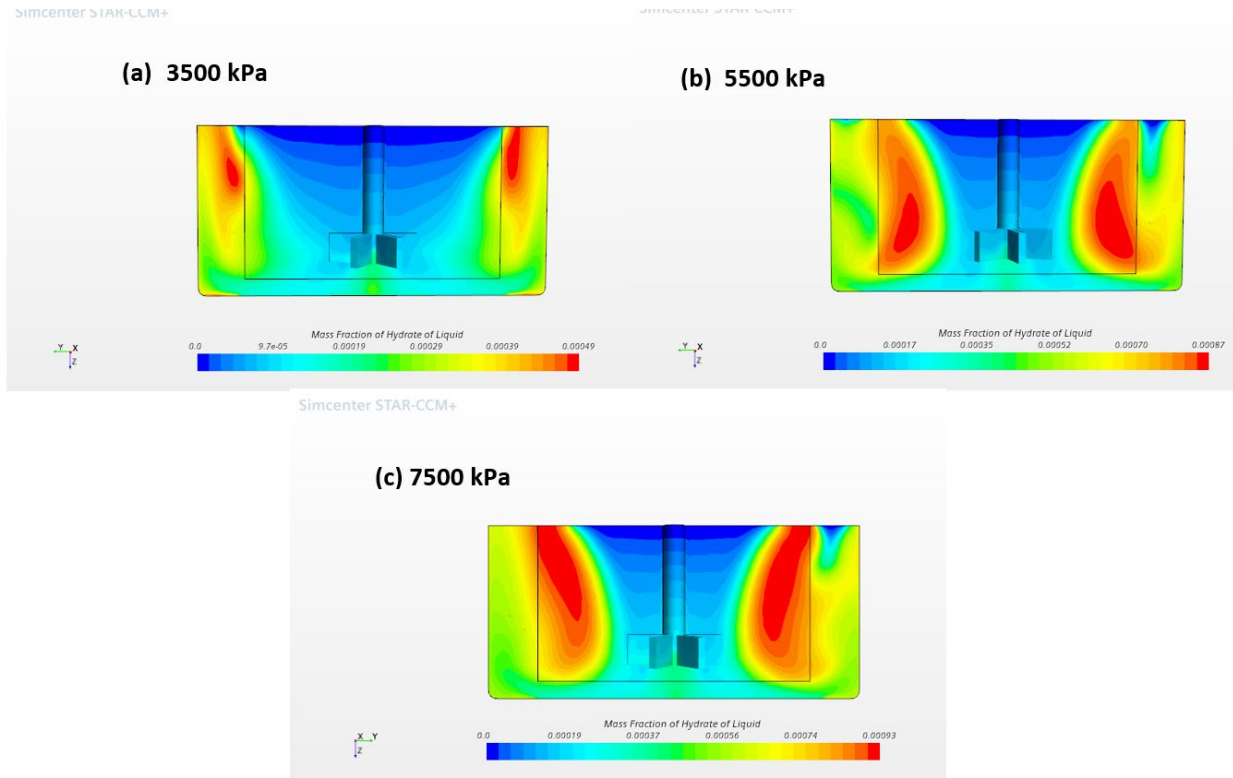
The Eulerian multiphase flow model in the CFD simulation considers two phases: the gas phase, as a dispersed phase, and water plus hydrate as a continuous phase. At the beginning of the simulation, no hydrate exists in the system. Hydrate is then formed when a specific driving force is maintained in the system. Based on the gas consumption rate equation (Equation (4-13)), the driving force expresses as the degree of subcooling (e.g., the difference between the system temperature and the hydrate equilibrium temperature at the system pressure). Mathews et al. (2000) reported this specific temperature driving force (subcooling) for natural gas hydrate nucleation to be around 6.5°F [58]. However, the model introduced in this paper assumes that hydrate nucleation occurs immediately after a specific subcooling when the water molecules touch the gas bubbles. According to Equation (4-11), the degree of subcooling is a function of two parameters, including system temperature and hydrate equilibrium temperatures. Also, the hydrate equilibrium temperature is a function of the system pressure and can be calculated using the hydrate equilibrium P-T diagram or commercial software. This paper calculates the hydrate equilibrium temperatures using PVTsim Nova software.

Figure 4-9 shows the effect of pressure (e.g., 3,500 to 7,500 kPa) on the methane hydrate formation for the stirring speed between 300 and 900 RPM. According to this figure, an increase in the amount of pressure leads to a significant increase in the methane hydrate mass fraction for different agitating speeds. The hydrate mass fraction reaches the value of 0.0016 when the pressure and the stirring rates are 7,500 kPa and 900 RPM, respectively. The hydrate mass fraction is 0.0005 for the case with a pressure of 3,500 kPa and a stirring rate of 300 RPM, because at high pressure the methane gas molecules can dissolve further in the water; thus, higher amount of methane will be converted into hydrate. In other words, the higher the pressure, the more hydrate forms in the

reactor due to an increase in the value of the subcooling. According to Figure 4-9, although increasing the speed of the impeller from 300 to 900 RPM leads to a significant increase in the value of the methane hydrate mass fraction when the pressure changes from 3,500 to 7,500 kPa, the hydrate mass fraction value for the stirring rate of 900 RPM increases with a lower rate compared to other agitating speeds such as 700 RPM. It is also seen that for 5,500 kPa pressure, the hydrate mass fraction increases from 0.0009 to 0.0014 when the stirring rate is increased from 300 to 900 RPM. This is because increasing the stirring rate leads to a reduction in the heat and mass transfer resistance [56]. Figure 4-10 illustrates the contours of hydrate mass fraction for different pressure varying from 3,500 to 7,500 kPa, where the gas volume fraction and the system temperature are 0.2 and 274.3 K, respectively. Figure 4-10 reveals that an increase in the pressure increases the amount of methane hydrate formation in the stirred reactor, particularly close to the wall and impeller blade. The mass fraction of methane hydrate is 0.0005 at 3,500 kPa, as compared to 0.00093 at 7,500 kPa.



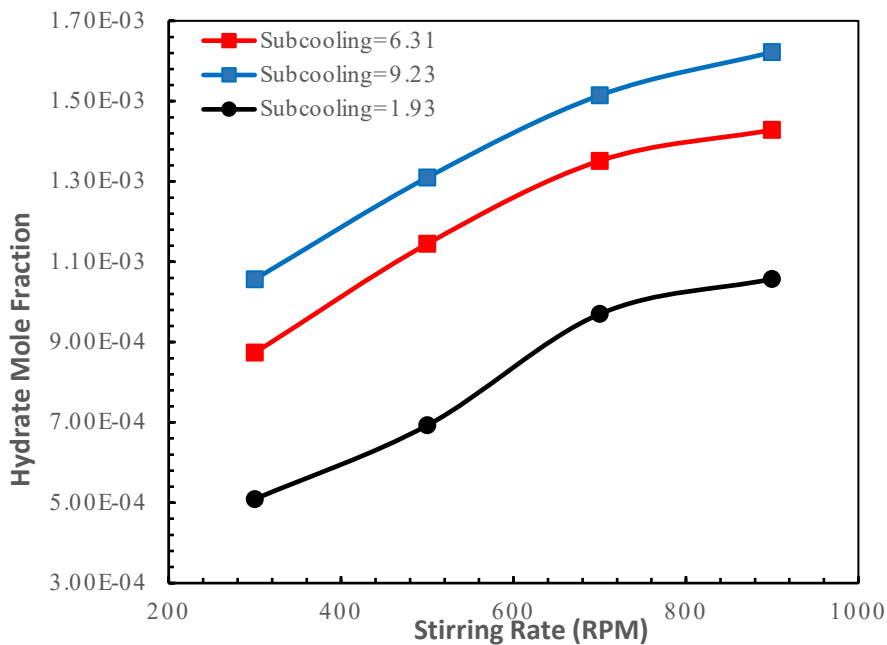
**Figure 4-9.** Effect of pressure and stirring rate on the methane hydrate mass formation in the stirred reactor [gas volume fraction=0.2, system temperature = 274.3 K].



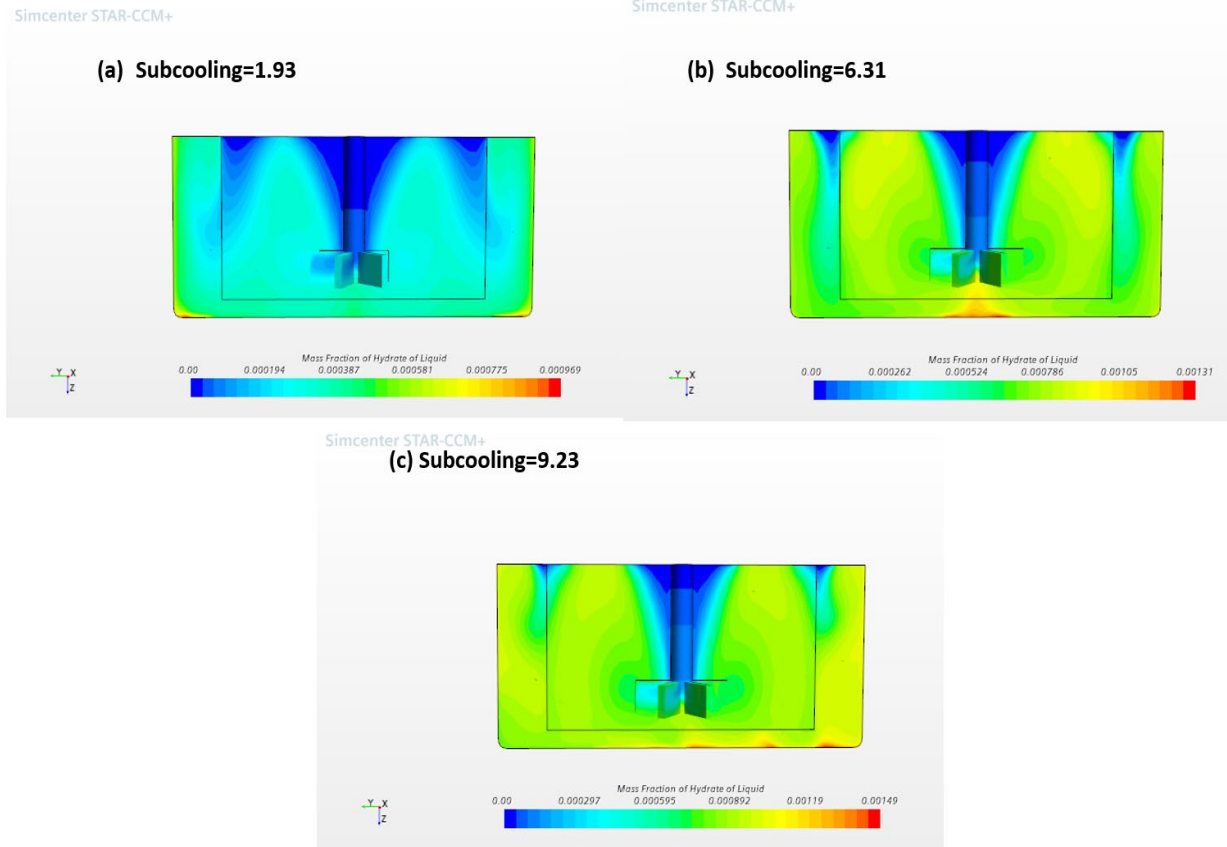
**Figure 4-10.** The contours of hydrate mass fraction for different pressure in the stirred reactor [Stirring rate = 300 RPM, gas volume fraction = 0.2, and system temperature = 274.3 K].

Figure 4-11 illustrates the effect of subcooling on the methane hydrate mass fraction for different stirring rates. In this phase, the gas volume fraction and the system temperature are 0.2 and 274.3 K, respectively. As presented in Figure 4-11, an increase in the subcooling causes a significant increase in the hydrate mass fraction. In the case with a subcooling of 1.91 °C and stirring rate of 300 RPM, the hydrate mass fraction is  $5.10 \times 10^{-4}$ , while it is 0.0011 for the stirring rate of 900 RPM. Hydrate mass fraction is  $6.93 \times 10^{-4}$  and  $9.7 \times 10^{-4}$  at 500 and 700 RPM, respectively. This is because subcooling is a driving force that facilitates methane hydrate formation in the stirred reactor according to the gas consumption rate as expressed by Equation (4-13). Figure 4-11 also implies that the higher the subcooling value, the more methane hydrate is formed in the reactor due to the greater thermal driving force. Because when the system pressure is increased, the

hydrate equilibrium temperature also increases, resulting in an increase in subcooling degree as thermal driving force. The highest hydrate mass fraction is formed at the subcooling of 9.23°C, while the lowest is at 1.92°C. Figure 4-12 presents hydrate mass fraction contour plots at different subcooling at a stirring rate of 900 RPM, the gas volume fraction of 0.2, and reactor temperature of 274.3 K. At 1.92°C subcooling, methane hydrate is formed in the area near the wall and impeller blades, while it is formed in almost all regions of the reactor at 6.21 and 9.23°C subcooling conditions. According to Figure 4-12, the hydrate mass fraction for the subcooling of 1.92°C is  $1.06 \times 10^{-3}$ . This parameter for other subcooling with the values of 6.21 and 9.23 are  $1.43 \times 10^{-3}$  and  $1.62 \times 10^{-3}$ , respectively.



**Figure 4-11.** Effect of subcooling on the methane hydrate mass formation in the stirred reactor [gas volume fraction=0.2, system temperature = 274.3 K].



**Figure 4-12.** Contour plots of mass fraction of hydrate in the stirred reactor with different degrees of subcooling [stirring rate = 900 RPM, gas volume fraction=0.2, and system temperature = 274.3 K].

## 4.5 CONCLUSIONS

In this work, a CFD model is developed to simulate the methane hydrate formation in a stirred reactor using STAR CCM+ software. This model is based on the Eulerian multiphase flow, in which water and hydrate are in the continuous phase and methane gas is in a dispersed phase. The software solves the conservation equations of momentum, mass, and energy simultaneously. The hydrate formation rate equations, including mass transfer, hydrate kinetics, and heat of hydrate formation, are incorporated in the mass and energy equations as source terms. The geometry,

meshing, and mesh independence were developed before solving and post-processing steps. The simulation results were validated using published experimental data for a stirred reactor, at 5,500 kPa, 274.3 K, and gas volume fraction of 0.04. The effects of stirring rate, gas volume fraction, pressure, and subcooling parameters on methane hydrate formation in stirred reactor were assessed. The main conclusions drawn from the research are summarized as follows:

1. The results of the mesh independence study show that among four different polyhedral cells, the simulations with a mesh number of 226,106 lead to more precise results. In addition, the time step of 0.01 seconds and simulation time of 15 seconds are selected for the simulation runs.
2. Methane hydrate formation was simulated successfully in stirred reactors at the temperature of 274.3 K and a pressure of 5,500 kPa with a gas volume fraction of 0.04., and a stirring rate of 300 RPM. The simulation results were validated with experimental data. The simulation results were in good agreement with experimental data with the overall AAD% of 15.7%. It was noticed that the results of simulations indicated that hydrate is mainly formed near the reactor walls and around stirrer blades.
3. The results showed that the methane hydrate mass fraction was maximized when the stirring rate was at 900 RPM. It was concluded that the higher stirring rates resulted in reduced heat and mass transfer resistance. High stirring rates can also help to increase the contact area between gas and water, as a result of higher rate of methane gas transferred to the liquid phase within the reactor.
4. Similar to the stirring rate, the higher gas volume fraction was also favoured more hydrate formation in the reactor. The maximum amount of methane hydrate was formed when the

gas volume fraction and stirring rates were at 0.4 and 900 RPM, respectively. An increase in methane gas concentration in water resulted in higher hydrate formation.

5. Methane hydrate formation in the stirred reactor is directly affected by the system pressure. For instance, an increase in the amount of pressure leads to a significant increase in the methane hydrate mass fraction. The higher solubility of methane molecules in the liquid phase as well as an increase in equilibrium hydrate formation temperature and subcooling can cause an increase in the amount of hydrate formation.
6. The gas consumption rate is directly proportional to subcooling as a driving force in the stirred reactor. The methane hydrate was formed in the areas close to the wall and the impeller blades at subcooling of 1.92°C. At higher subcooling of 6.21 and 9.23 °C, hydrate was observed almost in all regions within the reactor.

Although the CFD model is introduced for the stirred reactor, it can be applicable for complicated geometries in the oil and gas industry to investigate gas hydrate formation. In addition, this model can help oil and gas engineering sectors to control and manage gas hydrate. In this research, a sensitivity analysis is performed to understand the impact of key parameters (e.g., temperature and pressure) on the methane hydrate formation in stirred reactors. Considering a wider range of important parameters is recommended for the next phase of this work to obtain a better understanding of the gas hydrate phenomenon in various geometries. In future research, this model can be extended to study the hydrate formation for three-phase systems, including oil, methane, and water. In addition, the effects of type of thermodynamic inhibitors such as mono ethylene glycol and methanol at different compositions on the hydrate formation in various geometries can also be investigated.

## ACKNOWLEDGMENTS

The authors would like to acknowledge Memorial University (NL, Canada), the Natural Sciences and Engineering Research Council of Canada (NSERC), Suncor, ExxonMobil Canada, Equinor Canada, Energy Research Newfoundland and Labrador (ERI NL), and+ Department of Industry, Energy and Technology (IET) of Government of Newfoundland and Labrador for offering financial assistance.

## APPENDIX A

$M$  refers to the sum of interfacial forces and momentum associated with the mass transfer. The interfacial momentum transfer corresponding to the mass transfer and lift force is not considered.  $M$  contains the drag, virtual mass, and turbulent dispersion (or turbulent drag) forces as shown below [27, 43, 48]:

$$M_K = \sum_{j \neq k} (F_{kj}^D + F_{kj}^{VM} + F_{kj}^{TD}) \quad (\text{A-1})$$

where  $F_{kj}^D$  refers to the drag force;  $F_{kj}^{VM}$  is the virtual mass flow; and  $F_{kj}^{TD}$  resembles the turbulent dispersion force.

The forces are defined as the force per cell volume on phase  $k$  due to phase  $j$ , as given below:

$$F_{jk} = -F_{kj} \quad (\text{A-2})$$

The inter-phase drag force is a function of the drag coefficient and the relative velocity between two phases (gas and liquid) that can be determined by the following expression [43, 48]:

$$F_{kj}^D = \sum_j \frac{1}{2} W_j C_D \rho_c |\vec{u}_j - \vec{u}_k| \left( \frac{a_{kj}}{4} \right) (\vec{u}_j - \vec{u}_k) \quad (\text{A-3})$$

Where,  $W_j$  stands for the weight function;  $C_D$  represents the drag coefficient; and  $a_{kj}$  symbolises the interfacial area density [48].  $C_D$  is computed based on Schiller-Naumann equation [43, 48, 59] as follows:

$$C_D = \begin{cases} \frac{24}{Re_d} (1 + 0.15Re_d^{0.687}) & 0 < Re_d \leq 1000 \\ 0.44 & Re_d > 1000 \end{cases} \quad (A-4)$$

The dispersed Reynolds number ( $Re_d$ ) is determined as follows:

$$Re_d = \frac{\rho_c |\bar{u}_j - \bar{u}_k| l}{\mu_k} \quad (A-5)$$

Where,  $\rho_c$  refers to the density of the continuous phase;  $\mu_k$  is the dynamic viscosity of the continuous phase; and  $l$  indicates the interaction length scale or bubble size [48].

The acceleration of a particle that is submerged in the flow is influenced by the inertia of the surrounding.

This impact is represented as a “virtual mass” in the inviscid flow theory, as shown below:

$$F_{kj}^{VM} = C_{VM} \rho_c \phi_d (a_j - a_k) \quad (A-6)$$

where  $c$  is the continuous phase in the phase interaction  $kj$ ;  $d$  stands for the dispersed phase in the phase interaction  $kj$ ;  $C_{VM}$  represents the virtual mass coefficient for interaction  $kj$ ; and  $a_j$  and  $a_k$  are the acceleration of phase  $j$  and  $k$ , respectively [43, 48].

## NOMENCLATURES

---

### Acronyms

---

AAD	Average Absolute Deviation
AD	Absolute Deviation (g)
ANSYS	Analysis Systems
AAs	Anti-Agglomerate chemicals
AFPs	Antifreeze Proteins
CAD	Computer-Aided Design
CFD	Computational Fluid Dynamics
CSMHyK	Hydrate Kinetics Model from Colorado School of Mines
KHIs	Kinetic Hydrate Inhibitors
LDHIs	Low-Dosage Hydrate Inhibitors
MEG	Mono Ethylene Glycol
PBM	Population Balance Model
PBTU	Pitched Blade Turbines Upward Pumping
PDE	Partial Differential Equation
PVP	Polyvinylpyrrolidone
RPM	Radian Per Minute
RT	Rushton Turbine
WD	Water Depth

---

### Variables/Letters

---

$A_s$	Surface area ( $m^2$ )
$a_j, a_k$	Acceleration of phase $j$ and $k$ ( $m\ s^{-2}$ )
$a_{kj}$	Interfacial area density ( $m^{-1}$ )
$C_D$	Drag coefficient
$C_{p_{hyd}}$	Heat capacity of hydrate ( $J\ Kg^{-1}\ K^{-1}$ )
$C_{VM}$	Virtual mass coefficient for interaction $kj$
$d_b$	Bubble diameter that equals $40 \times 10^6\ m$
$f_{hyd}$	Mass fraction of hydrate in the water
$f_w$	Mass fraction of the water
$F_{kj}^D$	Drag force per unit of volume ( $N\ m^{-3}$ )
$F_{kj}^{VM}$	Virtual mass flow per unit of volume ( $N\ m^{-3}$ )

$F_{kj}^{TD}$	Turbulent dispersion force per unit of volume ( $\text{N m}^{-3}$ )
$g$	Gravity ( $\text{m s}^{-1}$ )
$h$	Phase enthalpy ( $\text{J Kg}^{-1}$ )
$k_1$	Intrinsic kinetics rate constants 1 ( $\text{Kg m}^{-2} \text{s}^{-1} \text{K}^{-1}$ )
$k_2$	Intrinsic kinetics rate constants 2 (K)
$l$	Interaction length scale or bubble size (m)
$n$	Stoichiometric coefficients
$n_{CH_4}$	Stoichiometric Coefficient of Methane Gas (1)
$n_{H_2O}$	Stoichiometric Coefficient of Water (5.75)
$n_{hyd}$	stoichiometric Coefficient of Hydrate (1)
$\dot{m}$	Mass transfer rate ( $\text{Kg s}^{-1}$ )
$m_{CH_4-Cal}$	Calculated methane consumption using the CFD model (g)
$m_{CH_4-Exp}$	Experimental value of methane consumption (g)
$M_K$	Sum of interfacial forces and momentum associated with mass transfer ( $\text{N m}^{-3}$ )
$p$	System pressure (Pa)
$Q$	Heat source term ( $\text{W m}^{-3}$ )
$\dot{q}_{hyd}$	Heat of hydrate formation (J/s)
$Re_d$	Dispersed Reynolds number
$T$	Turbulent
$t$	Time (second)
$T_{system}$	Actual system temperature (K)
$T_{hyd}$	Hydrate equilibrium temperature at the system pressure (K)
$\vec{u}_k$	Velocity of phase $k$ ( $\text{m s}^{-1}$ )
$u$	Correction Coefficient (1/500)
VF-g	Gas volume fraction
$W_j$	Weight function
$W_{hyd}$	Molar mass of methane hydrate
$W_{CH_4}$	Molar mass of methane gas

---

### Greek Letters

$\phi_k$	Volume fraction of phase $k$
$\rho_k$	Density of phase $k$ ( $\text{Kg m}^{-3}$ )
$\lambda$	Thermal conductivity ( $\text{W m}^{-1} \text{K}$ )

$\mu_k$	Dynamic viscosity of the continuous phase ( $\text{Kg m}^{-1} \text{s}^{-1}$ )
$\mu_t$	Turbulent viscosity (Pa s)
$\sigma_t$	Turbulent Prantle number with 0.9 value
$\Delta T_{sub}$	Subcooling (K)

---

### Subscripts and Superscripts

---

$k, j$	Phases
$hyd$	Hydrate
$g$	Gas
$sub$	Subcooling
$d$	Dispersed phase in the phase interaction
$t$	Turbulent
$W$	Water

### REFERENCES

1. Sloan, E.D., *Gas hydrates: review of physical/chemical properties*. Energy & Fuels, 1998. **12**(2): p. 191-196.
2. Sloan Jr, E.D. and C.A. Koh, *Clathrate hydrates of natural gases*. 2007: CRC press.
3. Sloan, E.D., *Natural gas hydrates in flow assurance*. 2010: Gulf Professional Publishing.
4. Jasamai, M., M. Idress, M.Z. Arshad, and M.F. Taha, *MITIGATION OF METHANE HYDRATE BLOCKAGE IN SUBSEA PIPELINES USING IONIC LIQUID AS HYDRATE INHIBITOR*. Platform: A Journal of Engineering, 2019. **3**(1): p. 13-18.
5. Gbaruko, B., J. Igwe, P. Gbaruko, and R. Nwokeoma, *Gas hydrates and clathrates: Flow assurance, environmental and economic perspectives and the Nigerian liquified natural gas project*. Journal of Petroleum Science and Engineering, 2007. **56**(1-3): p. 192-198.
6. Sloan, E., C. Koh, A. Sum, A. Ballard, G. Shoup, N. McMullen, J. Creek, and T. Palermo, *Hydrates: state of the art inside and outside flowlines*. Journal of petroleum technology, 2009. **61**(12): p. 89-94.

7. Sum, A.K., C.A. Koh, and E.D. Sloan, *Developing a comprehensive understanding and model of hydrate in multiphase flow: from laboratory measurements to field applications*. Energy & Fuels, 2012. **26**(7): p. 4046-4052.
8. Sloan, E.D., *A changing hydrate paradigm—from apprehension to avoidance to risk management*. Fluid Phase Equilibria, 2005. **228**: p. 67-74.
9. Kinnari, K., J. Hundseid, X. Li, and K.M. Askvik, *Hydrate management in practice*. Journal of Chemical & Engineering Data, 2015. **60**(2): p. 437-446.
10. Creek, J., *Efficient hydrate plug prevention*. Energy & Fuels, 2012. **26**(7): p. 4112-4116.
11. Meindinyo, R.-E.T. and T.M. Svartaas, *Gas hydrate growth kinetics: a parametric study*. Energies, 2016. **9**(12): p. 1021.
12. Meindinyo, R.-E.T., T.M. Svartaas, T.N. Nordbø, and R. Bøe, *Gas hydrate growth estimation based on heat transfer*. Energy & Fuels, 2015. **29**(2): p. 587-594.
13. Qureshi, M.F., M. Atilhan, T. Altamash, S. Aparicio, M. Aminnaji, and B. Tohidi, *High-pressure gas hydrate autoclave hydraulic experiments and scale-up modeling on the effect of stirring RPM effect*. Journal of Natural Gas Science and Engineering, 2017. **38**: p. 50-58.
14. Herri, J.-M., F. Gruy, J.-S. Pic, M. Cournil, B. Cingotti, and A. Siquin, *Interest of in situ turbidimetry for the characterization of methane hydrate crystallization: Application to the study of kinetic inhibitors*. Chemical Engineering Science, 1999. **54**(12): p. 1849-1858.
15. Farhadian, A., A. Kudbanov, M.A. Varfolomeev, and D. Dalmazzone, *Waterborne Polyurethanes as a New and Promising Class of Kinetic Inhibitors for Methane Hydrate Formation*. Scientific reports, 2019. **9**(1): p. 1-10.

16. Bavoh, C.B., M.S. Khan, B. Lal, N.I.B.A. Ghaniri, and K.M. Sabil, *New methane hydrate phase boundary data in the presence of aqueous amino acids*. Fluid Phase Equilibria, 2018. **478**: p. 129-133.
17. Ahmadpanah, S., M. Manteghian, and H. Ganji, *Effect of cyclopentane and sodium chloride on the formation kinetics of natural gas hydrate in different operating conditions*. Journal of Natural Gas Science and Engineering, 2022: p. 104417.
18. Zare, M., S. Zendehboudi, and M.A. Abdi, *Deterministic tools to estimate induction time for methane hydrate formation in the presence of Luvicap 55 W solutions*. Journal of Molecular Liquids, 2022. **348**: p. 118374.
19. Renault-Crispo, J.-S. and P. Servio, *Role of induction time on carbon dioxide and methane gas hydrate kinetics*. Journal of Natural Gas Science and Engineering, 2017. **43**: p. 81-89.
20. Hussain, S., A. Kumar, S. Laik, A. Mandal, and I. Ahmad, *Study of the kinetics and morphology of gas hydrate formation*. Chemical Engineering & Technology: Industrial Chemistry-Plant Equipment-Process Engineering-Biotechnology, 2006. **29**(8): p. 937-943.
21. Longinos, S.N. and M. Parlaktuna, *The effect of experimental conditions on methane hydrate formation by the use of single and dual impellers*. Reaction Kinetics, Mechanisms and Catalysis, 2021. **132**(2): p. 771-794.
22. Daraboina, N., P. Linga, J. Ripmeester, V.K. Walker, and P. Englezos, *Natural gas hydrate formation and decomposition in the presence of kinetic inhibitors. 2. Stirred reactor experiments*. Energy & Fuels, 2011. **25**(10): p. 4384-4391.
23. Tang, C., X. Dai, J. Du, D. Li, X. Zang, X. Yang, and D. Liang, *Kinetic studies of gas hydrate formation with low-dosage hydrate inhibitors*. Science China Chemistry, 2010. **53**(12): p. 2622-2627.

24. Lo, S. *CFD modelling of hydrate formation in oil-dominated flows*. in *Offshore Technology Conference*. 2011. OnePetro.
25. Balakin, B., A. Hoffmann, and P. Kosinski, *Experimental study and computational fluid dynamics modeling of deposition of hydrate particles in a pipeline with turbulent water flow*. *Chemical Engineering Science*, 2011. **66**(4): p. 755-765.
26. Balakin, B.V., A. Kosinska, and K.V. Kutsenko, *Pressure drop in hydrate slurries: Rheology, granulometry and high water cut*. *Chemical Engineering Science*, 2018. **190**: p. 77-85.
27. Balakin, B.V., S. Lo, P. Kosinski, and A.C. Hoffmann, *Modelling agglomeration and deposition of gas hydrates in industrial pipelines with combined CFD-PBM technique*. *Chemical Engineering Science*, 2016. **153**: p. 45-57.
28. Zerpa, L.E., E.D. Sloan, A.K. Sum, and C.A. Koh, *Overview of CSMHyK: A transient hydrate formation model*. *Journal of Petroleum Science and Engineering*, 2012. **98**: p. 122-129.
29. Sultan, R.A., M.A. Rahman, S. Rushd, S. Zendejboudi, and V.C. Kelessidis, *Validation of CFD model of multiphase flow through pipeline and annular geometries*. *Particulate Science and Technology*, 2019. **37**(6): p. 685-697.
30. Mahmoodi, M., N. Rezaei, S. Zendejboudi, and D. Heagle, *Fluid dynamic modeling of multiphase flow in heterogeneous porous media with matrix, fracture, and skin*. *Journal of Hydrology*, 2020. **583**: p. 124510.
31. Huque, M.M., S. Butt, S. Zendejboudi, and S. Imtiaz, *Systematic sensitivity analysis of cuttings transport in drilling operation using computational fluid dynamics approach*. *Journal of Natural Gas Science and Engineering*, 2020. **81**: p. 103386.

32. Makwashi, N., D. Zhao, T. Ismaila, and I. Paiko. *Pipeline Gas Hydrate Formation and Treatment: A Review*. in *3rd National Engineering Conference on Building the Gap between Academia and Industry, Faculty of Engineering, Bayero University, Kano*. 2018.
33. Bendiksen, K.H., D. Maines, R. Moe, and S. Nuland, *The dynamic two-fluid model OLGA: Theory and application*. SPE production engineering, 1991. **6**(02): p. 171-180.
34. Turner, D., J. Boxall, S. Yang, D. Kleehammer, C. Koh, K. Miller, E. Sloan, Z. Xu, P. Matthews, and L. Talley. *Development of a hydrate kinetic model and its incorporation into the OLGA2000® transient multiphase flow simulator*. in *5th international conference on gas hydrates, Trondheim, Norway*. 2005.
35. Davies, S.R., J.A. Boxall, L.E. Dieker, A.K. Sum, C.A. Koh, E.D. Sloan, J.L. Creek, and Z.-G. Xu, *Predicting hydrate plug formation in oil-dominated flowlines*. Journal of petroleum science and engineering, 2010. **72**(3-4): p. 302-309.
36. Davies, S.R., J.A. Boxall, C. Koh, E.D. Sloan, P.V. Hemmingsen, K.J. Kinnari, and Z.-G. Xu, *Predicting hydrate-plug formation in a subsea tieback*. SPE Production & Operations, 2009. **24**(04): p. 573-578.
37. Wang, Y., C.A. Koh, J.A. Dapena, and L.E. Zerpa, *A transient simulation model to predict hydrate formation rate in both oil-and water-dominated systems in pipelines*. Journal of Natural Gas Science and Engineering, 2018. **58**: p. 126-134.
38. Sule, I., A. Adedeji, C. Obeng, A. Okosun, M. Morshed, M. Rahman, and K. Hawboldt, *CFD analysis of hydrate formation in pipelines*. Petroleum Science and Technology, 2015. **33**(5): p. 571-578.

39. Neto, E. *A mechanistic computational fluid dynamic CFD model to predict hydrate formation in offshore pipelines.* in *SPE Annual Technical Conference and Exhibition.* 2016. OnePetro.
40. Turco Neto, E., M. Rahman, S. Imtiaz, and S. Ahmed. *Numerical Flow Analysis of Hydrate Formation in Offshore Pipelines Using Computational Fluid Dynamics (CFD).* in *International Conference on Offshore Mechanics and Arctic Engineering.* 2016. American Society of Mechanical Engineers.
41. Yao, S., Y. Li, W. Wang, G. Song, Z. Shi, X. Wang, and S. Liu, *Investigation of hydrate slurry flow behaviors in deep-sea pipes with different inclination angles.* *Oil & Gas Science and Technology—Revue d'IFP Energies nouvelles*, 2019. **74**: p. 48.
42. Song, G., Y. Li, W. Wang, K. Jiang, Z. Shi, and S. Yao, *Hydrate agglomeration modeling and pipeline hydrate slurry flow behavior simulation.* *Chinese journal of chemical engineering*, 2019. **27**(1): p. 32-43.
43. Zare, M., V. Talimi, S. Zendehboudi, and M.A. Abdi, *Computational fluid dynamic modeling of methane hydrate formation in a subsea jumper.* *Journal of Natural Gas Science and Engineering*, 2022. **98**: p. 104381.
44. Sangare, D., S. Bostyn, M. Moscossa-Santillan, and I. Gökalp, *Hydrodynamics, heat transfer and kinetics reaction of CFD modeling of a batch stirred reactor under hydrothermal carbonization conditions.* *Energy*, 2021. **219**: p. 119635.
45. Ding, J., X. Wang, X.-F. Zhou, N.-Q. Ren, and W.-Q. Guo, *CFD optimization of continuous stirred-tank (CSTR) reactor for biohydrogen production.* *Bioresource technology*, 2010. **101**(18): p. 7005-7013.

46. Ramírez, L.A., E.L. Pérez, C. García Díaz, D.A. Camacho Luengas, N. Ratkovich, and L.H. Reyes, *CFD and Experimental Characterization of a Bioreactor: Analysis via Power Curve, Flow Patterns and  $k_L a$  Processes*, 2020. **8**(7): p. 878.
47. Mevik, C., *Particle size distribution of methane hydrates and particle growth using a CFD-PBM model*. 2018, The University of Bergen.
48. CD-adapco, S.-C., *11.0 User Guide*. CD-Adapco Inc.: Melville, NY, USA, 2016.
49. Talimi, V., P. Thodi, M. Abedinzadegan Abdi, R. Burton, L. Liu, and J. Bruce, *Enhancing harsh environment oil spill recovery using air floatation system*. *Safety in Extreme Environments*, 2020. **2**(1): p. 57-67.
50. Gyurik, L., A. Egedy, J. Zou, N. Miskolczi, Z. Ulbert, and H. Yang, *Hydrodynamic modelling of a two-stage biomass gasification reactor*. *Journal of the Energy Institute*, 2019. **92**(3): p. 403-412.
51. Vysniauskas, A. and P. Bishnoi, *A kinetic study of methane hydrate formation*. *Chemical Engineering Science*, 1983. **38**(7): p. 1061-1072.
52. Englezos, P., N. Kalogerakis, P. Dholabhai, and P. Bishnoi, *Kinetics of gas hydrate formation from mixtures of methane and ethane*. *Chemical Engineering Science*, 1987. **42**(11): p. 2659-2666.
53. Boxall, J., S. Davies, C. Koh, and E.D. Sloan, *Predicting when and where hydrate plugs form in oil-dominated flowlines*. *SPE Projects, Facilities & Construction*, 2009. **4**(03): p. 80-86.
54. Cents, A., D.W.F. Brillman, G. Versteeg, P. Wijnstra, and P.P. Regtien, *Measuring bubble, drop and particle sizes in multiphase systems with ultrasound*. *AIChE journal*, 2004. **50**(11): p. 2750-2762.

55. Burla, S.K. and S.P. Pinnelli, *Enrichment of gas storage in clathrate hydrates by optimizing the molar liquid water–gas ratio*. RSC Advances, 2022. **12**(4): p. 2074-2082.
56. Clarke, M.A. and P. Bishnoi, *Determination of the intrinsic kinetics of CO<sub>2</sub> gas hydrate formation using in situ particle size analysis*. Chemical Engineering Science, 2005. **60**(3): p. 695-709.
57. Skovborg, P., H. Ng, P. Rasmussen, and U. Mohn, *Measurement of induction times for the formation of methane and ethane gas hydrates*. Chemical Engineering Science, 1993. **48**(3): p. 445-453.
58. Matthews, P.N., P.K. Notz, M.W. Widener, and G. Prukop, *Flow loop experiments determine hydrate plugging tendencies in the field*. Annals of the New York Academy of Sciences, 2000. **912**(1): p. 330-338.
59. Balakin, B., A. Hoffmann, P. Kosinski, and S. Høiland, *Turbulent flow of hydrates in a pipeline of complex configuration*. Chemical engineering science, 2010. **65**(17): p. 5007-5017.

## **5. CHAPTER FIVE**

### **Summary and Recommendations for Future Work**

This thesis focuses mainly on methane hydrate formation behaviours/mechanisms in complicated geometries, including a jumper and stirred reactor using CFD software. In addition, this research aims to predict a critical parameter (induction time) for the methane + water + Luvicap 55W systems through deterministic models. In this project, commercial software packages (Star CCM+ and GEP ) and Matlab software are employed to run different systems for methane hydrate formation. Star CCM+ is a CFD software for SIEMENS with a license that is used for simulations of jumper and stirred reactor systems. This thesis includes 5 chapters. An introduction/background is provided in chapter one. Methane hydrate formation in a jumper is simulated using Star CCM+ in chapter two in which the impacts of key parameters, such as subcooling and inlet gas temperature, gas volume fraction, and inlet liquid velocity on the hydrate formation are studied. In chapter three, the deterministic models (ANFIS, LSSVM, and GEP) are employed to predict the induction time for systems of methane + water + Luvicap 55 W. Also, a sensitivity analysis is performed based on the ANFIS model to find the influences of inlet parameters and their relationship on the induction time prediction. The methane hydrate formation in the agitated reactor is studied in chapter fourth in which hydrate formation is simulated in different cases, considering a various range of effective parameters, including stirring rate, subcooling, pressure, and gas volume fraction. The current chapter (chapter fifth) includes the summary and recommendations.

## **5.1 Computational Fluid Dynamic Modeling of Methane Hydrate Formation in Subsea Jumper (Chapter 2)**

Hydrate formation in a jumper is studied for a system of methane gas in the presence of water in different conditions using Star CCM+ as a CFD software. The developed model is applied to simulate methane hydrate formation in the jumper. This model is based on the multiphase Eulerian model that includes conservation of mass, momentum, and energy; they are solved simultaneously where the mass transfer, hydrate kinetics, and heat of hydrate formation are incorporated in the mass and energy equations, respectively. The geometry drawing and meshing are done before solving and post-processing steps. Firstly, methane hydrate formation in the jumper is modeled when gas velocity is 5 m/s. The gas volume fraction and the gas inlet temperature are 0.2 and 7 °C, respectively. Then, the influence of subcooling, inlet temperature, inlet gas velocity, and gas volume fraction is estimated for methane hydrate formation in the jumper. The key outcomes of this phase are as follows:

- Methane hydrate is formed in the jumper less when the fluid inlet velocity and gas inlet temperature increase. In contrast, an increase in subcooling and gas volume fraction leads to more hydrate formation in the jumper.
- The simulation results show that the hydrate mass fraction has a higher value near the wall region than in the middle area of the pipe due to the cold wall temperature and higher subcooling.
- Hydrate cannot be observed at the inlet. The amount of formed hydrate is then gradually increased and becomes maximum close to the end of the jumper.

- The higher value of inlet fluid velocity, the lower hydrate formed in the jumper due to insufficient residence time for methane gas to be solved in water. The maximum hydrate formation is observed when the inlet fluid velocity is 5 m/s.
- Subcooling is an effective parameter for hydrate formation since the gas consumption rate equation is directly proportional to this parameter. The subcooling value near the non-slip wall is higher than that of the pipe center due to the wall temperature. Therefore, methane hydrate is observed further near the wall than at the center of the pipe.
- A decrease in the fluid inlet temperature leads to a significant increase in the amount of formed hydrate in the jumper.

## **5.2 Deterministic Tools to Estimate Induction Time for Methane Hydrate Formation in the Presence of Luvicap 55 W Solutions (Chapter 3)**

The key parameter that represents the quality of the KHIs is the induction time for systems containing KHIs. In this research, the induction time is calculated using deterministic models, such as LSSVM, ANFIS, and GEP for methane/ Luvicap 55W/ water systems. 440 experimental data points are used to develop the models, where 85% of the data are utilized for the training step and 15% for the testing step. The induction time is a target (output), while the molecular weight of the solution ( $Mw_{sol}$ ), mass fraction of KHI ( $m_i$ ), temperature ( $T_{exp}$ ), system pressure (P), and subcooling ( $\Delta T$ ) are considered input parameters. The collected experimental data are split randomly into two subgroups including training (85%) and testing (15%) data points before running the models. Training data set is needed for developing the models, while the testing data set is used to evaluate the accuracy of the trained models. The criterion for the termination of the

modeling is when  $R^2$  value is close to one. Based on the conducted literature review, the LSSVM and ANFIS models are selected, since these two approaches had exhibited an excellent performance in predicting of hydrate equilibrium parameters. In addition, these two models have been used in several applications in chemical and petroleum engineering and led to high reliability and precision. Also, GEP model is selected to introduce a correlation to better represent the relationship between the induction time and input parameters. In fact, there are rare correlations in the literature to predict the induction time of the methane/water/Luvicap 55W solutions.

The performance of deterministic models is investigated using statistical parameters, including ARE, AARE%, and  $R^2$ . Moreover, the sensitivity analysis is performed for the developed ANFIS model to find out the relationship between the induction time and input parameters and find the most significant parameters. The main conclusions drawn from this research work are given below:

- The developed LSSVM model is able to predict the induction time with good accuracy, where the  $R^2$  values for the training and testing phases are 0.929 and 0.940, respectively.
- The coefficient deterministic ( $R^2$ ) values for the training and testing phases of the ANFIS model reveal that there is an acceptable match between the calculated and experimental induction time.
- The coefficient deterministic ( $R^2$ ) values for the training and testing phases of the ANFIS are 0.930 and 0.944, respectively, while the  $R^2$  values for the training and testing phases of the GEP model are 0.973 and 0.958, respectively.
- The GEP model has greater performance for the induction time prediction in the training and testing phases, compared with LSSVM and ANFIS models.
- The run time of the GEP model is much more than that of the ANFIS and LSSVM models.

- The system pressure and temperature are the most influential parameters for the induction time according to the sensitivity analysis results obtained from the ANFIS model.
- Based on sensitivity analysis and Pearson correlation coefficient, the molecular weight of the solution, mass fraction of the Luvicap 55 W, and subcooling have indirect relationships with the induction time.
- The developed equation from the GEP approach can be employed to predict the induction time for the methane/ Luvicap 55 W solution.

### **5.3 Computational Fluid Dynamics Approach to Study Methane Hydrate Formation in Stirred Reactor (Chapter 4)**

In this chapter, methane hydrate formation in the stirred reactor is studied using Star CCM+ as CFD software. The Eulerian multiphase flow model is selected for the simulation runs, assuming that water and hydrate are considered as the continuous phase and methane gas is considered as the dispersed phase. The conservation equations of momentum, mass, and energy with a turbulent model are solved simultaneously, where the hydrate equations, including mass transfer, hydrate kinetics, and heat of hydrate formation, are incorporated in the mass and energy equations (in the form of source terms), respectively. Solving and postprocessing steps are performed after the geometry drawing and meshing stages. The stirred reactor is simulated to study methane hydrate formation, where the system pressure, system temperature, and volume fraction are 5,500 kPa, 274.3 K, and 0.04, respectively. Then the results of this simulation are validated with experimental data from the literature. The sensitivity analysis is conducted to identify the effect of pressure (3,500 -7,500 kPa), subcooling (1.93 - 9.23 °C), gas volume fraction (0.04 - 0.4), and stirring speed

(300 - 900 RPM) on the methane hydrate formation in the agitated reactor. The main outcomes of this phase are as follows:

- The optimum values of the time step and the simulation time are 0.01 and 15 seconds, respectively according to the CFD simulation runs.
- The mesh independence study is performed; the results indicate that a mesh number of 226,106 between four different polyhedral cells has more precise results.
- The amount of hydrate concentration in the area around the impeller blades and near the walls is higher, where the volume fraction of methane is small with a value of 0.008.
- Comparing the simulation results and experimental data reveals that the developed CFD model has a good performance for induction time prediction; therefore, the overall AAD% is 15.7%.
- The amount of formed hydrate is maximum when the stirring rate is 900 RPM, while the minimum value of methane hydrate is 1.38 g, where the volume fraction is 0.04.
- The higher gas volume fraction values, the more hydrate formation is observed in the agitated reactor.
- An increase in the subcooling parameter leads to an increase in the hydrate formation since the gas consumption rate is directly proportional to subcooling as a driving force in the stirred reactor.
- Similar to subcooling, high-pressure is a favorable parameter to increase the amount of hydrate formation in the agitated reactor. In other words, an increase in the amount of pressure leads to a significant increase in the methane hydrate mass fraction for different agitating speeds. This is because increasing the system pressure causes an increase in the

equilibrium hydrate formation temperature, resulting in an increase in the subcooling as a driving force for hydrate formation.

## 5.4 Recommendations for Future Work

In this research, methane hydrate formation is studied in two different geometries (jumper and stirred reactor) using Star CCM + software. The influences of the key parameters, including gas volume fraction, subcooling, pressure, inlet temperature, fluid velocity, and stirring rate on hydrate formation are investigated. Moreover, the smart models are introduced to predict the induction time of methane/Luvicap 55 W solutions. The recommendations for future work based on the scope of this thesis are summarized below:

- Further experimental studies are needed to accurately determine the kinetic constants ( $k_1$  and  $k_2$ ) for the methane gas consumption rate equation and then validate the developed models in the jumper and other complicated geometries in pipeline systems.
- Further sensitivity analysis is needed to figure out the effects of the different parameters such as pressure, inlet fluid temperature, gas volume fraction, and subcooling on the hydrate behaviors in the jumper; this can help to find the parameters with high impacts on the methane hydrate formation.
- In this research, only methane hydrate formation for the systems, including water and methane gas is studied. Adding the oil phase to the fluid systems can lead to simulating real conditions in offshore facilities.
- Methane hydrate formation in the presence of thermodynamic inhibitors with different concentrations in the stirred reactor and other geometries can be investigated in future studies using CFD software.

- Broader range of key parameters, including pressure, subcooling, and temperature for investigation of hydrate formation in complicated geometries can be considered for future work.
- Prediction of induction time for methane/ natural gas hydrate systems in the presence of other KHIs using deterministic models is recommended for future work.
- The development of new correlations for the induction time calculation for natural gas hydrate in the presence of KHI solutions using hybrid models, such as ANFIS and ANN-PSO is suggested for future work.
- Using other deterministic models to estimate induction time for the natural gas/KHIs solutions such as PVP is recommended for future study.
- The developed model for the stirred reactor can be extended to the complicated geometries in the oil and gas industries to study hydrate formation.
- The developed CFD model can be extended to study hydrate formation for the three-phase systems, including oil, water, and gas. The sensitivity analysis can be performed for these systems as well.
- The effect of thermodynamic inhibitors (mono ethylene glycol and methanol) with the various concentrations on the methane hydrate formation in the stirred reactor and other geometries are suggested for future work.